In Situ Thermal Annealing and Growth Investigations on III/V Semiconductor Materials

Dissertation

zur
Erlangung des Doktorgrades
der Naturwissenschaften
(Dr. rer. nat.)

dem

Fachbereich Physik
der Philipps-Universität Marburg

vorgelegt von

Rainer Straubinger, M. Sc.

aus

Ingolstadt

Marburg (Lahn), 2018

Vom Fachbereich Physik der Philipps-Universität Marburg
als Dissertation angenommen am: 19. Juni 2018
Erstgutachterin: Frau Prof. Dr. Kerstin Volz
Zweitgutachter: Herr Prof. Dr. Heinz Jänsch
Tag der mündlichen Prüfung: 21. Juni 2018
Hochschulkennziffer: 1180

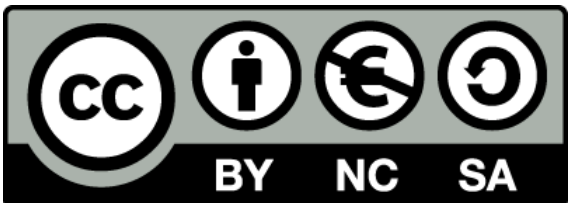

Contents

CHAPTER 1

Introduction

In situ (scanning) transmission electron microscopy [(S)TEM] has proven to be an outstanding technique for investigating dynamic processes in material structures under high resolution conditions. In general there are two approaches to perform *in situ* (S)TEM experiments in the presence of gases. These are based on a differential pumping scheme also called environmental TEM (ETEM) [1–4] and a closed cell holder [5–8]. Each has its advantages and disadvantages as shown in detail in [9, 10].

In the differential pumping approach, the pioneering work was done by H. Hashimoto and T. Naiki [2] in the 1950s and 1960s resulted in the development of the first reaction specimen chamber compatible with TEM based on differential pumping. Due to refinements carried out by Baker and co workers in the 1970s, particle mobility and carbon filament growth could be studied [11–13]. In later ETEMs, the so called environmental-cell is an integrated part of the microscope column, which increases the stability and thereby the resolution. This type of setup allowed E. D. Boyes and P. L. Gai to demonstrate a point resolution of 0.23 nm in a 0.4 hPa N_2 environment in 1997 [3]. One advantage of ETEMs is that all commercially available TEM holders such as heating holders can be used without modifications [14, 15]. This paves the way for various kinds of *in situ* investigation such as catalytic experiments [16–19], experiments on nano particles [20–22] and crystal growth investigations [23–26]. Since then, resolution has gradually been improved using field emission guns [27–29] and aberration correctors [30, 31]. Besides the aforementioned advantages, the most important drawback of the ETEM relative to the closed cell holder approach is the long gas path through which the electron beam must pass in the upper and lower region of the specimen (around 1 cm). This limits the pressure for high resolution investigations to around 20 hPa [32]. Furthermore, deposits of gases can affect the microscope adversely.

In contrast, the closed cell holder approach uses specially designed TEM holders to enclose the specimen between two electron transparent windows (e.g. C or SiN), confining

the gas within a thin slab around the sample [5]. The holder developed by L. F. Allard and co workers in 2012 enables the possibility of working at pressures up to 1,000 hPa and 1,000°C. Furthermore, this type of closed cell holder can be used in different microscopes without further modifications to the TEM column. To prove the functionality of the developed gas cell holder, L. F. Allard and co workers investigated gold nanoparticles revealing a point resolution of 0.29 nm. Further investigations on $CuAu/TiO_2$ catalysts showed that it was possible to investigate catalytic processes at elevated temperatures and at much higher pressures compared to ETEMs [33]. This development makes high resolution *in situ* TEM investigations in a specific environment and at elevated temperatures feasible for a wide range of research [34–39].

Moreover, these pressure and temperature ranges match the growth and post-growth annealing conditions during metal organic vapor phase epitaxy (MOVPE) and consequently, the usage of *in situ* TEM holders enables the possibility of studying MOVPE processes under high resolution conditions.

Thesis Objective

The first step for the investigations carried out in this thesis was to develop a gas storage and transfer system. This would allow the possibility of handling toxic and phyrophoric precursors inside the atmosphere holder designed and produced by Protochips. This setup is capable of facilitating group V stabilized thermal annealing experiments inside a TEM under high resolution conditions [40]. In addition, the development of a procedure for transferring an electron transparent focused ion beam (FIB) lamella onto the thermal e-chip was also required [41].

For the *in situ* TEM studies the two technologically relevant material systems Ga(N,As,P) [42, 43] and Ga(P,Bi) [42, 44, 45] have been investigated. These compound semiconductors are promising candidates for optoelectronic applications on Si. Ga(N,As,P) for example could be capable of overcoming the efficiency limitations of gallium indium arsenide phosphide ((Ga,In)(As,P)) based structures [46–48].

Unfortunately, the realization of good quality epitaxial layers of highly metastable materials is indeed very challenging [49–53]. A successful approach to improve the layer quality and therefore increase the optical output of these structures is post-growth annealing [44, 54–59]. Here, the required energy is introduced by thermal annealing to enable atomic movement and therefore rearrange wrong bonds or diffuse imperfections out of the structure.

Nevertheless, *in situ* information with regards to cluster formation, desorption processes, and material distribution within the Ga(N,As,P) and Ga(P,Bi) layer due to thermal treatment are still missing. One possible reason for this are the complications involved in

handling the necessary precursor gases to enable thermal annealing experiments under MOVPE conditions i.e. without taking the incongruent desorption of group V species into account. To overcome this issue when handling toxic and pyrophoric group III and group V precursors such as trimethylgallium (TMGa), tertiarybutylphospine (TBP), or hydride based precursors, it is necessary to have an *in situ* system which fulfills all of the technical- and safety-requirements of a modern MOVPE machine.

This thesis shows that it is possible to build this type of *in situ* system and the first results using the setup show the possibility of gaining an in-depth understanding of growth kinetics and thermal annealing processes of III/V semiconductors.

List of Publications:

- R. Straubinger, A. Beyer and K. Volz, Preparation and Loading Process of Single Crystalline Samples into a Gas Environmental Cell Holder for *In Situ* Atomic Resolution Scanning Transmission Electron Microscopic Observation, *Microscopy and Microanalysis* **22**(3):515–519, 2016. DOI: 10.1017/S1431927616000593
- R. Straubinger, A. Beyer, T. Ochs, W. Stolz and K. Volz, *In Situ* Thermal Annealing Transmission Electron Microscopy (TEM) Investigation of III/V Semiconductor Heterostructures Using a Setup for Safe Usage of Toxic and Pyrophoric Gases, *Microscopy and Microanalysis* **23**(4):751-757, 2017. DOI: 10.1017/S1431927617012351
- R. Straubinger, M. Widemann, J. Belz, L. Nattermann, A. Beyer and K. Volz, Thermally Introduced Bismuth Clustering in Ga(P,Bi) Layers under Group V Stabilised Conditions Investigated by Atomic Resolution *In Situ* (S)TEM. Submitted to *Scientific Reports* (2018)
- A. Beyer, R. Straubinger, J. Belz and K. Volz, Local sample thickness determination via scanning transmission electron microscopy defocus series, *Journal of Microscopy* **262**(2):171-177, 2015. DOI: 10.1111/jmi.12284
- E. Sterzer, N. Knaub, P. Ludewig, R. Straubinger, A. Beyer and K. Volz, Investigation of the microstructure of metallic droplets on Ga(AsBi)/GaAs, *Journal of Crystal Growth*, **408**:71-77, 2014.

CHAPTER 2

The Investigated Materials

In this chapter, the crystal structures of the investigated semiconductor materials are discused. Subsequently, the basics of crystal growth via metal organic vapor phase epitaxy (MOVPE) are explained. Thereafter, examples of typical group III and group V source molecules, which were also present during the *in situ* experiments, are introduced. Next, the possible crystal defects resulting from the epitaxial growth and the effects of post-growth thermal annealing on these defects are discussed. Finally, the model systems which are used to demonstrate the functionality of the *in situ* setup are presented.

2.1 Fundamentals of Crystal Structures

The materials investigated in this work have a crystalline structure which exhibits a periodic arrangement of atoms. This periodicity can be described by the translation vector $\vec{R}$ with the following form:

$$\vec{R} = u\vec{a}_1 + v\vec{a}_2 + w\vec{a}_3, \tag{2.1}$$

where $\vec{a}_{1,2,3}$ are basis vectors which build a unit cell and u, v and w are integers. It follows that the characteristics of the crystal at a specific position $\vec{r}$ are the same as at the position $\vec{r} + \vec{R}$.

Furthermore, the model systems used for the *in situ* investigations are based on GaP and Si heterostructures, therefore the focus of the following explanation will be on this material group. Being a member of group IV of the periodic table, Si has four electrons in its outermost shell. The three p-orbitals together with the s-orbital form four equivalent sp^3-hybrid orbitals. Therefore solid Si results from each Si forming four covalent bonds with its neighbouring atoms. This results in a tetragonal structure with angles of 109°

at its apexes. This arrangement is also called a diamond structure, and consists of two face-centered cubic (fcc) sub-lattices shifted from one another by 1/4 along the [111] plane. GaP crystallizes in the zinc blend structure, which is similar to the aforementioned diamond structure. However, in this case one of the fcc sub-lattices is occupied with group III atoms and the other sub-lattice is filled with group V atoms.

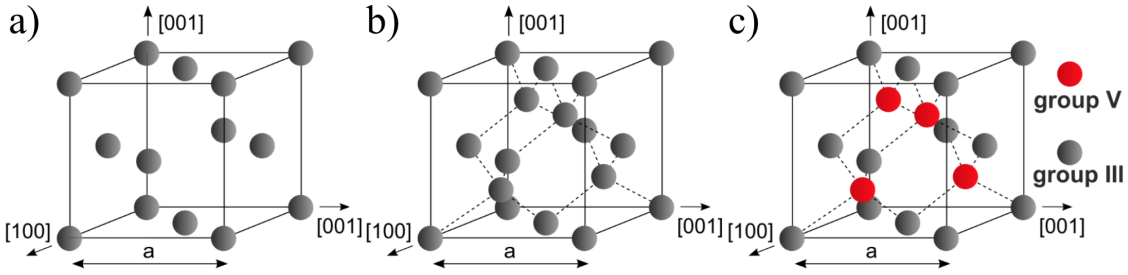

Figure 2.1: a) unit cell of a face-centered cubic (fcc) structure. b) the arrangement of the atoms in a diamond structure: this consists of two fcc sub-lattices shifted from one another by 1/4 along the [111] plane. c) crystal arrangement of the zinc blend structure. Both sub-lattices are occupied with either group III or group V atoms.

In many cases it is useful to consider the crystal structure in momentum space. Momentum space is defined by the basis vectors $\vec{b}_1$, $\vec{b}_2$ and $\vec{b}_3$ of the following form

$$\vec{b}_1 = 2\pi \frac{\vec{a}_2 \times \vec{a}_3}{\vec{a}_1 \cdot (\vec{a}_2 \times \vec{a}_3)} \ , \tag{2.2}$$

$$\vec{b}_2 = 2\pi \frac{\vec{a}_3 \times \vec{a}_1}{\vec{a}_1 \cdot (\vec{a}_2 \times \vec{a}_3)} \ , \tag{2.3}$$

$$\vec{b}_3 = 2\pi \frac{\vec{a}_1 \times \vec{a}_2}{\vec{a}_1 \cdot (\vec{a}_2 \times \vec{a}_3)} \ . \tag{2.4}$$

Consequently, the relationship between the basis vectors in real space and the reciprocal space can be written as

$$\vec{a}_i \cdot \vec{b}_j = 2\pi\delta_{ij} \text{ with i, j = 1, 2, 3 and } \delta_{ij} = \begin{cases} 1 & \text{it } i = j \\ 0 & \text{it } i \neq j \end{cases} . \tag{2.5}$$

In analogy to the translation vector $\vec{R}$ in real space (compare 2.1), one can define the reciprocal lattice vector $\vec{g}_{hkl}$ in momentum space as follows:

$$\vec{g}_{hkl} = h \cdot \vec{b}_1 + k \cdot \vec{b}_2 + l \cdot \vec{b}_3 \ . \tag{2.6}$$

Here h, k, and l are the so-called Miller indices. Furthermore the plane (hkl) represents a real lattice plane which is orthogonal to the reciprocal lattice vector in 2.6 and intercepts the real axes at $(\frac{\vec{a}_1}{h}, \frac{\vec{a}_2}{k}, \frac{\vec{a}_3}{l})$. Therefore the notation $[hkl]$ represents a direct lattice vector $h\vec{a}_1 + k\vec{a}_2 + l\vec{a}_3$ which is the normal to the lattice planes (hkl) in a cubic lattice.

2.2 Crystal Growth via MOVPE

To gain a better understanding of the results in chapter 8, it is necessary to understand the physical basis and limits of epitaxial growth. In addition to the small overview given in the following text, a more detailed description can be found in [60].

The foundation of crystal growth is a substrate material which determines the in-plane lattice constant of the epitaxial layer. After the deposited atoms reach the surface of the substrate, they move on the surface until they find an energetically favorable position such as a step edge. This process can be grouped into two processes: homoepitaxy and heteroepitaxy. In homoepitaxy, the deposited atoms are identical to the substrate, whereas in the case of heteroepitaxy, the added atoms are different from the substrate. In the case of heteroepitaxy, one needs to take the surface energy of the individual surfaces (γ_A, γ_B) and the surface energy of the boundary layer (γ_{AB}) into account. In doing this, and with the knowledge that the system always acts to minimize its surface energy, one is able to understand the single crystal growth mechanism. The relationship between the total energy and the single surface energies can be written as

$$\Delta E = (\gamma_B + \gamma_{AB} - \gamma_A) \cdot (1 - \delta) \cdot C = \Delta\gamma \cdot (1 - \delta) \cdot C \ . \tag{2.7}$$

As mentioned above, γ_A and γ_B are the surface energies of the substrate and epitaxial layer, respectively. γ_{AB} is the energy of the boundary layer and δ is the amount of left over substrate surface C. Formula 2.7 already indicates that the surface energy of the individual elements has an influence on the growth mechanism of the crystal structure. Here one distinguishes between three main growth mechanisms:

Frank-van-der-Merwe Growth [61–63] $(\gamma_A > \gamma_B + \gamma_{AB})$
Here, the growth is two dimensional along the step edges. The growth takes place layer by layer.

Volmer-Weber Growth [64] $(\gamma_A < \gamma_B + \gamma_{AB})$
As a result of the larger surface energy of the epitaxial layer, three dimensional island growth is preferred. This often results in a rough surface and a boundary layer.

Stranski-Krastanov Growth [65] ($\gamma_A \approx \gamma_B + \gamma_{AB}$)
This model is a combination of the two- and three dimensional growth.

Non-Equilibrium Growth Conditions

The growth of a metastable III/V semiconductor in a non-equilibrium growth regime is realized by partial pressures in the gas phase, which are much higher than the corresponding equilibrium partial pressures. In the case of III/V compounds, the vapor pressure of the group V species is higher than the vapor pressure of group III species. This fact results in an incongruent evaporation, where the desorption of the group V atoms from the surface is higher than the desorption of the group III atoms. To compensate for this effect, it is necessary to add the group V precursors in excess to the reactor during growth. Under these circumstances the growth rate is determined by the group III flux. Nevertheless, the growth temperature also plays a significant role in the growth process. Figure 2.2 shows the dependence of logarithmic growth rate on the inverse substrate temperature. Here, the three areas A, B, and C are distinguishable. In regime (A), where the substrate temperature is highest, the thermal energy is high enough to allow atoms which have already bonded to the surface to leave the surface. The growth rate is therefore desorption limited. In the mass transport limitation regime (B), the growth rate is limited by the group III supply and independent from the temperature. The limitation in regime (C) stems from the incomplete decomposition of the precursors (compare to section 2.3) and the surface reactions [68]. Of course the three regimes shown here are different for every material system. Nevertheless, the sketch shown in figure 2.2 illustrates that one needs to take extra care when working with materials with different vapor pressures as was done in this work. This statement is also true for post-growth thermal annealing experiments (compare to section 2.4).

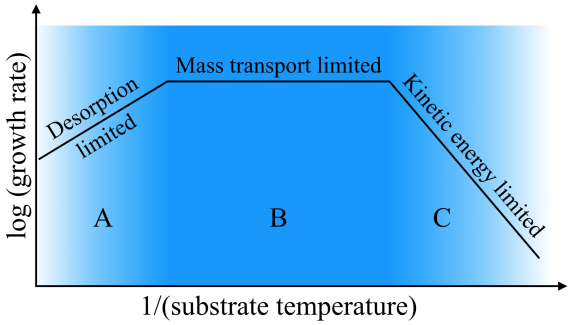

Figure 2.2: Sketch of the three main growth rate limitating factors depending on the substrate temperature. [66, 67]

2.3 Group III and Group V Source Molecules

In the following section the precursors used for this study are discussed i.e. trimethylgallium (TMGa) and tertiarybutylphosphine (TBP). In addition their bonding configurations, melting and boiling point will be discussed. Next, a short overview of the vapor pressures of typically used group III and group V precursors will be given. A more detailed description of typical precursors for MOVPE processes is given in [60].

Trimethylgallium: TMGa

In this work TMGa was used as a Ga precursor [66, 69]. The bonding in group III molecules can be understood from the valence bond theory of hybridized covalent bonding [70]. The incomplete electron shell of the atoms contains one p and two s electrons. Thus, the three covalent bonds between the metal and the organic rest group are formed with a hybridized sp^2 bonding configuration. This results in a planar, trigonal molecule with three ligands separated by 120° angles as depicted in figure 2.3. Moreover, after the three covalent bonds are formed, the p orbital remains unfilled. This unfilled p orbital, lying perpendicular to the plane of the molecule is electrophilic. Further characteristics of TMGa are a melting point of -15.8 °C and a boiling point of 55.8 °C [71]. So it is a liquid precursor at room temperature, which allows easy handling for many applications.

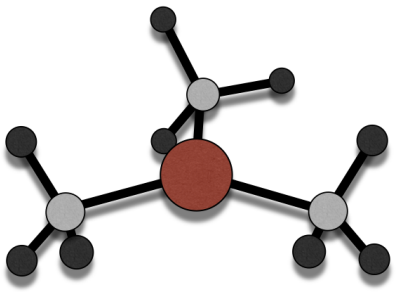

Figure 2.3: Sketch of the TMGa precursor bonding configuration (red: Ga, grey: C, black: H).

One reason why TMGa was chosen instead of the also well established triethylgallium (TEGa) for this study is the much higher vapor pressure of TMGa. Figure 2.5 a) shows the temperature dependence of the vapor pressure of several common group III precursors [60]. For clarity the vapor pressure dependence on temperature for TMGa is marked in red. Furthermore the graphs shown in Figure 2.5 a) and Figure 2.5 b) indicate the general trend that the vapor pressure is higher for lighter molecules.

A second reason why TMGa is a good candidate for the used *in situ* setup and the performed investigations is the great stability of the precursor. Thus it can be stored for indefinite periods at room temperature prior to use and is less likely to be involved in parasitic reactions.

Tertiarybutylphosphine: TBP

The phosphorus source used for the *in situ* experiment was TBP [72]. The bonding in group V molecules is characterized by three p electrons and two s electrons in the unfilled shell. Thus the formation of three covalent bonds satisfies the bonding requirements. Figure 2.4 shows the tetragonal bonding configuration caused by the sp^3 hybridization. The butyl-group and the two H atoms form a structure with bond angles of approximately 109°. Atop this arrangement is a pair of electrons forming no covalent bond. These electrons, referred to as a "lone pair", are important for interactions of the group V precursor molecules with surfaces and with other molecules. Moreover, due to this arrangement the molecules behave as electron donors. Further characteristics of TBP are a melting point of 4 °C and a boiling point of 56.1 °C. So like TMGa it is a liquid at room temperature, wich allows easy handling. The temperature dependence of vapor pressure of several common group V precursors is depicted in Figure 2.5 b). For clarity the corresponding TBP dependency is marked in red. The high vapor pressure of 381 hPa at room temperature [72] as depicted in Figure 2.5 b) makes TBP very suitable for many MOVPE processes. Moreover, it is found to be 50 % pyrolyzed at a temperature of 450 °C [73], which is several hundred degrees lower than for example the pyrolysis temperature for PH_3 [73–75]. The major pyrolysis reactions are deduced to be isobutane, PH_2, and PH, with a small amount of isobutene and phosphine. As already mentioned in the previous section, the graphs shown in Figure 2.5 a) and Figure 2.5 b) display the general trend that the vapor pressure is higher for lighter molecules.

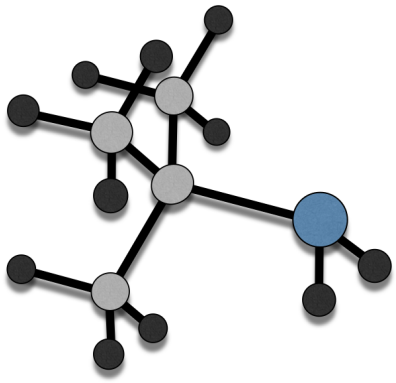

Figure 2.4: Sketch of the TBP precursor bonding configuration (blue: P, grey: C, black: H).

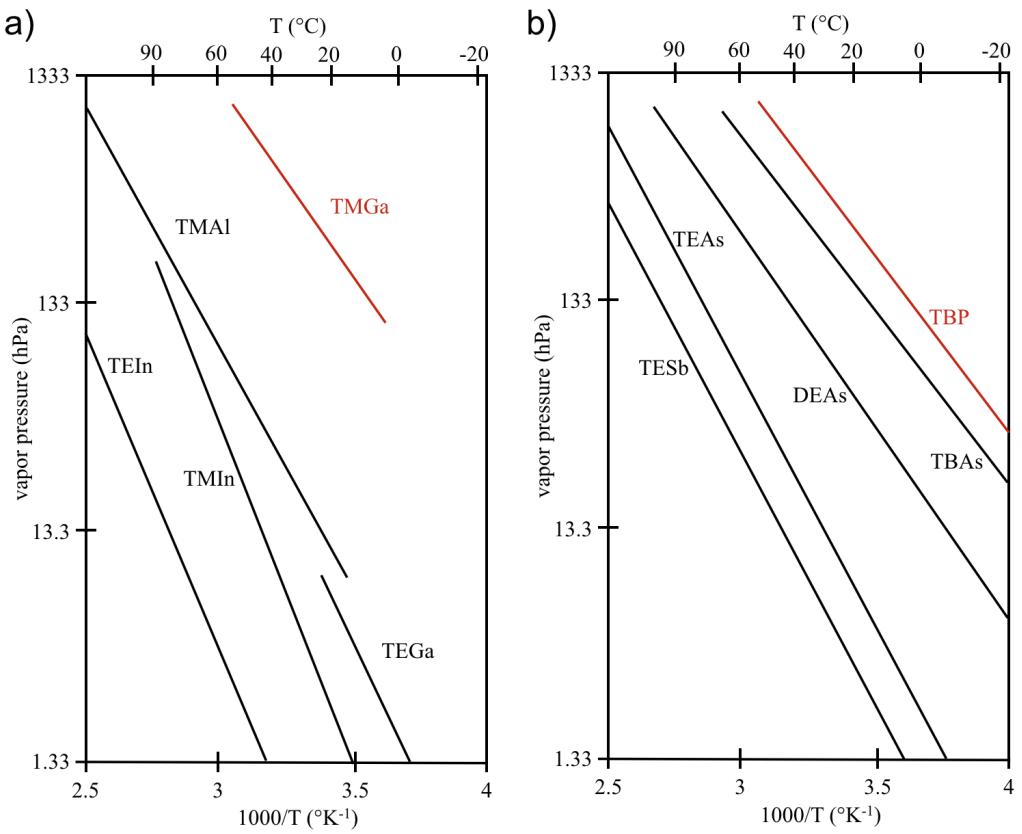

Figure 2.5: The graph a) shows the temperature dependence of vapor pressure for common group III precursors. The graph b) shows the temperature dependence of vapor pressure for common group V precursors [60].

2.4 Crystal Defects and Post-Growth Annealing

In reality, the grown crystals are not perfect and these imperfections can have negative influences on the later performance and lifetime of the device. In the following, a short overview of the different defects and the method of post-growth thermal annealing for decreasing the number of defects in the crystal will be given.

Point defects are zero dimensional defects in the crystal lattice. One example is the vacancy, which is a missing atom in the crystal lattice that would be occupied in a perfect crystal. In contrast, interstitials are atoms that are located in between lattice sites of a perfect crystal. In crystals like GaP with more than one species of atom, one atom can occupy a lattice site of the wrong sublattice; this kind of irregularity is called an antisite defect. Substitutional defects (impurities) are non-native atoms incorporated into the lattice of the perfect crystal. This could be either intentional, for example, the atom could act as donor or acceptor to increase or decrease the charge carrier density, or this could be an undesirable defect of growth that degrades the material. The most common examples

of impurities in MOVPE are oxygen and carbon atoms from the organic rest groups of the precursors (compare section 2.3).

Line defects derive their name from the fact that these types of defects have a two dimensional expansion through the crystal and the distorted atoms in the crystal lie along a line. Some of these dislocations can relieve misfit strain in a heteroepitaxially grown semiconductor and are therefore called misfit dislocations. A second type of dislocation, which extends through the layer to the surface of the following interface of the crystal structure, is referred to as a threading dislocation. Threading dislocations are often attached to misfit dislocations.

Due to the dynamic properties of defects and dislocations in the crystal, it is possible to reduce the amount of imperfections in the structure to a crucial point by post-growth thermal annealing. Here, the thermal energy is supplied to enable atomic movement. This therefore rearranges wrong bonds or diffuses imperfections out of the structure.

For Ga(N,As,P), post-growth annealing reveals an increase of the photoluminescence (PL) intensity with rising annealing temperature [76]. Investigations performed by S. Gies [54] and T. Wegele [57] show changes in the composition of the quantum well and a gradual exchange of arsenic and phosphorous atoms between the Ga(N,As,P) layer and the GaP barriers.

Growth investigations on Ga(P,Bi) on GaP carried out by L. Nattermann [56] show that the higher growth temperature of the following GaP layer serve as a thermal annealing for the Ga(P,Bi) layer. Due to this, the Bi accumulates within the Bi containing layer, which results in a inhomogeneous Bi distribution. Further investigation on Ga(As,Bi) epilayers revealed formation and phase transformation of Bi containing clusters upon annealing [77].

2.5 The Investigated Model Systems

In the following, the two model systems Ga(N,As,P) and Ga(P,Bi) are introduced. Moreover, the reason why these samples are of special interest for the *in situ* investigations will be discussed and the sample structure of both samples is introduced.

Ga(N,As,P)

As shown by T. Wegele [57] in case of a complex material like Ga(N,As,P), not only the growth temperature but also the post-growth thermal annealing procedure has a strong impact on the layer quality. Furthermore, the annealing time and the annealing temperature seems to have a large influence on diffusion processes within the quantum well structure. Rapid thermal annealing (RTA) experiments carried out at annealing

temperatures of 925°C and above revealed pore-like spheres within the quantum well structure.

Due to the *in situ* system developed in the framework of this thesis, it is possible to investigate the aforementioned thermal annealing processes at high resolution conditions without taking group V desorption into account. This deeper insight enables further improvements on the growth and post-growth annealing conditions in order to enhance the device properties. To ensure no contribution due to post-growth thermal annealing, the investigated sample was not thermally annealed after growth in the MOVPE machine.

Ga(N,As,P) Sample Structure

The Ga(N,As,P) multi quantum well structure investigated in this study is grown by MOVPE in a horizontal reactor. The schematic structure and the width of the layers can be seen in figure 2.6. GaP/Si (001) templates serve as pseudo substrates consisting of a 48 nm thick GaP layer nucleated on an exact Si (001) substrate. Ga(N,As,P)/GaP/(B,Ga)P heterostructures were grown on these templates to achieve a laser integrated on Si. To obtain a better interface quality, the growth was interrupted while exposing TBP and TBAs to the surface after every epitaxial layer. A more detailed description of the defect-free nucleation of GaP on Si (001) and the growth of the Ga(N,As,P)/GaP/(B,Ga)P/Si laser structure is given in the work of Liebich et al. [42] and Volz et al. [78]. At the end, a cap consisting of 150 nm (B,Ga)(As,P) and 50 nm (B,Ga)P was grown on top of the quantum well structure.

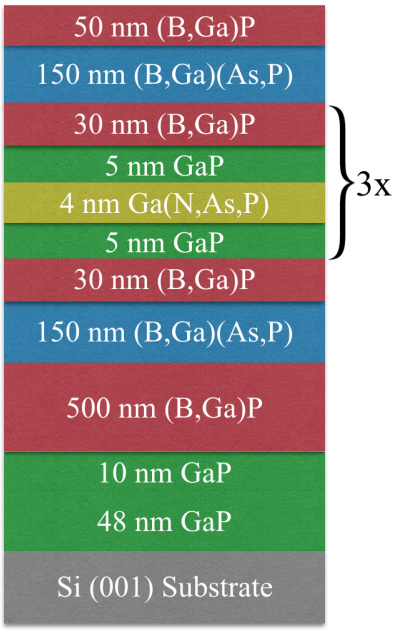

Figure 2.6: Schematic structure of the layers of the investigated sample.

Ga(P,Bi)

Due to the possibility to deposit GaP nearly lattice matched on Si [79, 80], Ga(P,Bi) on GaP could be a promising candidate for optoelectronic applications on Si. Investigation performed by L. Nattermann and colleagues [58] realized MOVPE growth of Ga(P,Bi) on GaP with Bi fractions up to 8% [53]. Nevertheless, the low growth temperature needed to incorporate a high fraction of Bi and at the same time ensure a good layer quality is a

major challenge. Furthermore, Bi shows the tendency to accumulate during the growth of the following layer at higher temperatures. This behavior makes Ga(P,Bi) a perfect candidate for *in situ* TEM investigations. Moreover, the information gained from the *in situ* investigations allows a more detailed knowledge of the dynamic processes during the MOVPE growth.

Ga(P,Bi) Sample Structure

Like the aforementioned Ga(N,As,P) multi quantum well structure, the Ga(P,Bi) sample was also grown by MOVPE. The schematic structure and the layer thickness of one quantum well of the repetitive structure is shown in figure 2.7. Compared to the Ga(N,As,P) samples, the Ga(P,Bi) quantum wells were grown on a GaP substrate. To ensure a good quality GaP surface, a 250 nm thick GaP layer was grown on top of the substrate at 675 °C. To enable the growth of Ga(P,Bi), the temperature was decreased to 400 °C. Each Ga(P,Bi) layer has a thickness of 55 nm and a Bi content of 0.5 %, 3.2 %, 3.4 %, and 7.4 %, respectively, and is, except for the last GaP layer which has a thickness of 200 nm, embedded in a 100 nm thick GaP layer grown at 625 °C.

Figure 2.7: Schematic structure of the investigated Ga(P,Bi) sample.

CHAPTER 3

Scanning Transmission Electron Microscopy

In this chapter the fundamental interaction processes between the impinging electrons and a crystalline sample in a scanning transmission electron microscope (STEM) will be introduced. First, the differences between the mechanisms of elastic and inelastic scattering are presented. To get a deeper understanding of the intensity distribution in the shown micrographs in this work it is necessary to understand the Rutherford scattering process in detail. Subsequent, an overview of the operating modes of magnetic lenses and the corresponding lens aberrations will be given. Finally, the high angle annular dark field (HAADF) image formation process using a STEM will be presented.

3.1 Mechanisms of Elastic and Inelastic Scattering

The sketch depicted in figure 3.1 a) shows the two scatter mechanisms between an isolated atom and a high-energy electron. In the first case the electron interacts with the electron cloud around the nucleus. Here, the small coulomb attraction results in a small deflection angle. In the second case the electron penetrates the electron cloud and reaches the nucleus. Due to the much larger coulomb interaction between the electron and the nucleus, the electron will be scattered at a larger angle. It should be mentioned that both of these interactions are not fully elastic. Nevertheless, the minor loss of energy is negligible in this simplified picture. A more detailed description of this kind of electron-atom interaction is given in section 3.2.

In contrast to the aforementioned elastic scattering event, the sketch depicted in figure 3.1 b) shows one of the possible inelastic interactions resulting in X-ray radiation. Here, an impinging electron penetrates through the outer electron cloud and interacts with one inner shell electron. If the beam electron transfers enough energy to this electron, the electron can be freed from the attraction of the nucleus into the vacuum, leaving a hole in the inner shell. In case of a solid it escapes above the Fermi level into the unfilled states.

This process results in an atom in its excited state with an excess of energy. By filling the hole with an electron from an outer shell the ionized atom can reduce energy. This transition is accompanied by the emission of a characteristic X-ray. It should be noted that emitting an X-ray is not the only way of reducing energy of the atom. By emitting a so called 'Auger electron' the atom can also reduce its energy.

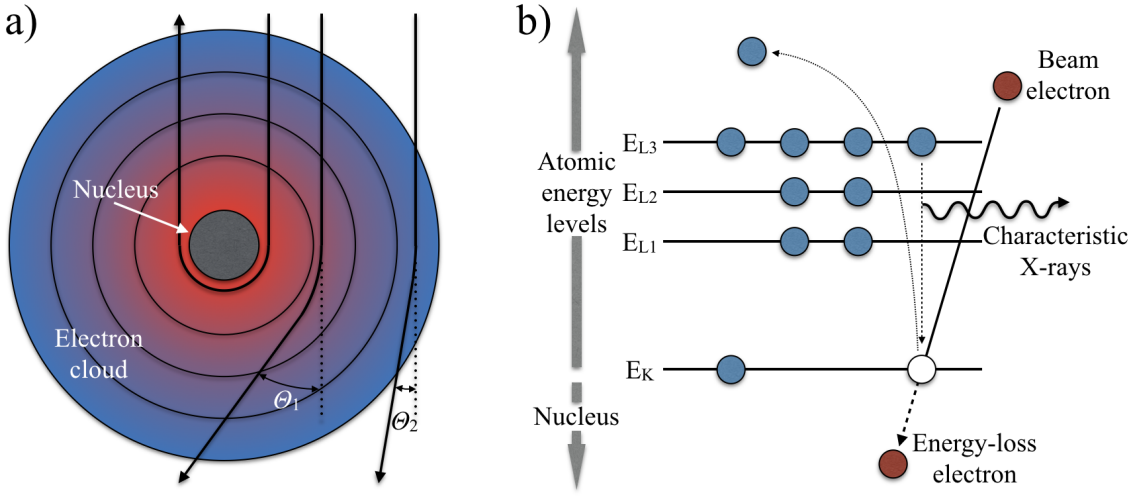

Figure 3.1: The sketch a) shows the two different scatter mechanisms between an isolated atom and a high-energy electron. The coulomb interaction with the electron cloud results in low-angle scattering, whereas the coulombic attraction with the nucleus causes higher-angle scattering and backscattering ($\Theta > 90°$). The potential within the electron cloud is always positive. The sketch depicted in b) shows a simplified model of the ionization process resulting in X-ray radiation. Here, the electron beam transfers enough energy to one inner shell electron to free it from the attraction of the nucleus. When the hole in the inner shell is filled by a higher electron, characteristic X-ray emission occurs.

3.2 Rutherford Scattering

The contrast generation in HAADF images is primarily determined by electrons scattering to high angles ($> 3°$). In this regime the deflection of the beam electron is best described by Rutherford scattering [81, 82]. Ernest Rutherford (1911) described backscattering and derived the expression for the differential cross section to high-angle scattering by the nucleus alone as follows

$$\sigma_R(\theta) = \frac{e^4 Z^2}{16(4\pi\varepsilon_0 E_0)^2} \frac{d\Omega}{sin^4\frac{\theta}{2}} \ . \tag{3.1}$$

Here, Z is the atomic number, e (-1.602 $\times$ 10^{-19}C) the elementary charge, E_0 the kinetic energy of the particles, ε_0 the dielectric constant and θ the scattering angle. Equation 3.1

ignores relativistic effects and assumes that the beam electron does not lose energy due to inelastic processes. Accordingly, the energy of the electrons, E_0 is fixed. This assumption can be tolerated for low acceleration voltages below 100 kV. One further effect, which is neglected in equation 3.1, is the screening of the electron cloud. By replacing the $\sin^2(\theta/2)$ term with $[\sin^2(\theta/2) + (\theta_0/2)^2]$, screening is taken into account and the differential cross section is effectively reduced and the amount of scattering is lowered. θ_0 is called the screening parameter and is given by

$$\theta_0 = \frac{0.117 Z^{1/3}}{E_0^{1/2}} \ . \tag{3.2}$$

Adding relativistic and screening corrections to equation 3.1, the net result is

$$\sigma_R(\theta) = \frac{Z^2 \lambda_R^4}{64\,\pi^4 a_0^2} \frac{d\Omega}{\left[sin^2\left(\frac{\theta}{2}\right) + \frac{\theta_0^2}{4}\right]^2} \ . \tag{3.3}$$

Where λ_R is the relativistically corrected electron wavelength

$$\lambda_R = \frac{h}{\left[2 m_0 e V \left(1 + \frac{eV}{2 m_0 c^2}\right)\right]^{(1/2)}} \tag{3.4}$$

and a_0 the Bohr radius of the scattering atom

$$a_0 = \frac{h^2 \varepsilon_0}{\pi m_0 e^2} \ . \tag{3.5}$$

Here, m_0 (9.109×10^{-31} kg) is the rest mass of the electron, c (2.998×10^8 m/s) is the speed of light in vacuum and ε_0 is the dielectric constant.

The modified Rutherford cross section equation (3.3) is one of the most important equation for understanding HAADF image generation.

3.3 Operating Modes of Magnetic Lenses

To understand the functioning of magnetic lenses, one needs to understand how an electron behaves in a magnetic field with a strength $\vec{B}$ and an electric field of strength $\vec{E}$. The aforementioned electron with the charge q (= -e) will experiences the so called Lorentz force $\vec{F}$, which also depends on the velocity of the electron $\vec{v}$. These factors are related through the equation

$$\vec{F} = q(\vec{E} + \vec{v} \times \vec{B}) = -e(\vec{E} + \vec{v} \times \vec{B}) \ . \tag{3.6}$$

Because there is no electric field within the lens, the resulting Lorentz force $\vec{F}$ is a vector normal to the velocity $\vec{v}$ and the magnetic field $\vec{B}$, which are inclined to one another at an angle Θ.

Consequently, the force F an electron experiences by entering a uniform magnetic field nearly 90° to $\vec{B}$ is

$$F = evBsin\Theta = evB = \frac{mv^2}{r} \ , \tag{3.7}$$

where r is the radial distance of the electron from the optic axis and m is the mass of the electron. Later in the manuscript it will be shown, that this restriction of the angle Θ is an oversimplification. After rearranging equation 3.7, the radial distance r can be written as

$$r = \frac{mv}{eB} \ . \tag{3.8}$$

As already mentioned in chapter 3.2, in the contemplation of modern TEM's with high accelerating voltages it is imperative to take relativistically effects into account. Therefore equation 3.8 becomes

$$r = \frac{\left[2m_0E\left(1 + \frac{E}{2E_0}\right)\right]^{\frac{1}{2}}}{eB} \ . \tag{3.9}$$

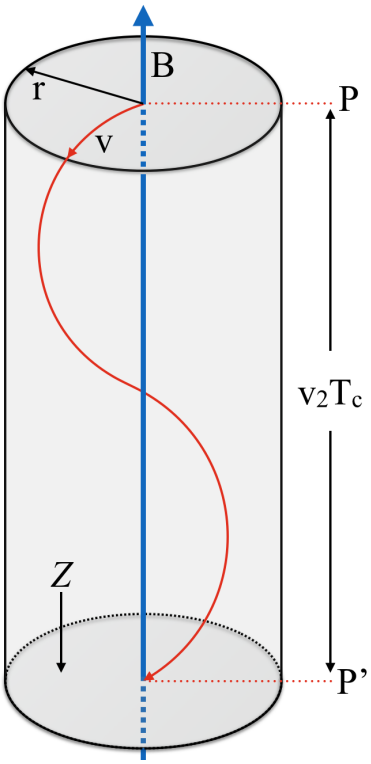

Figure 3.2: Sketch of the electron trajectory in a homogeneous magnetic field. The Lorentz force causes electrons passing through point P on the optic axis to spiral through the field and intersect the axis again at P'

The restriction of the angle Θ to 90° leads to the consequence that an electron which travels straight down the optic axis experience no force and therefore is not focused. Only the deviation from $\Theta = 90°$ results in a force. Therefore it is necessary to consider the two components of the velocity $\vec{v}$ within the magnetic field separately. Here, $\vec{v}_1$ is the movement perpendicular to the magnetic field and $\vec{v}_2$ is the component of the velocity parallel to $\vec{B}$. Figure 3.2 shows the sketch of the electron trajectory in a homogenous magnetic field, where $v_1 = v\,sin\,\Theta$ and $v_2 = v\,cos\,\Theta$. The resulting parallel component $\vec{v}_2$ leads to a motion parallel to the optic axis in the z

direction, with $z = v_2 t$, while the perpendicular component produces circular motion with a radius given by equation 3.8. The period of rotation T_c through the field can be related to the cyclotron frequency ω_c by

$$\omega = \frac{2\pi}{T_c} = \frac{eB}{m} \ . \tag{3.10}$$

From the aforementioned relationships one is now able to calculate the complete ray paths through the lens. These so called paraxial (i.e. near-axial ray) equations determine the radial distance r as well as the rotation angle Θ for an moving electron in an homogenous magnetic field around the axis in z direction.

$$\frac{d^2 r}{dz^2} + \frac{\eta^2 B^2 r}{2V^{1/2}} = 0 \tag{3.11}$$

$$\frac{d\Theta}{dz} = \frac{\eta B}{2V^{1/2}} \tag{3.12}$$

Here V is the accelerating voltage of the microscope and η is $(e/2m_0c^2)^{1/2}$. One can see from equation 3.11 that the rate of change of r along the optic axis is smaller for more energetic electrons and furthermore larger for more intense magnetic fields within the lens. Accordingly equation 3.12 shows that the angular rotation rate increases with increasing field strength and decreases for more energetic electrons.

3.4 Lens Aberrations

In chapter 3.3 the basic operation principles of magnetic lenses are discussed. However here only paraxial rays were taken into account and therefore additional errors resulting from real lenses were not considered. These errors will be pointed out in this section. Figure 3.3 shows sketches of the four most prominent aberrations. The most relevant aberration in modern STEMs is the spherical aberration which is depicted in figure 3.3 a). This effect has its origin in the inhomogeneity of the magnetic field of the lens. This results in stronger focusing for electrons which travel further away from the optic axis through the magnetic lens. As a result, a point object is imaged as a disk of finite size. Conversely, this means that the ability to magnifying details is limited because the details degrade during the imaging process. The constant C_s is called the spherical aberration coefficient and characterises the distance between the Gaussian image plane and the plane of least confusion for a particular lens. Furthermore the diameter of the Gaussian image of a point formed by paraxial rays is defined as $\sigma = C_s \Theta^3$. Astigmatism, which is depicted in figure 3.3 b), is caused by the asymmetry of round magnetic lenses. If the lens is not perfectly radial symmetric, the focal length varies depending on the point of entry of the

electron into the magnetic lens. As illustrated in the corresponding sketch, an electron coming from the point P and entering the magnetic field in the horizontal plane (red) will result in a shorter focal length (P_1) compared to the vertical plane (blue) which will result in the focal length P_2. This effect results in an elongated image of the object in each of the mentioned planes. In addition, like spherical aberration, the chromatic aberration (C_c) also leads to image blurring. In this case, electrons with different kinetic energies experience a different Lorentz force within the magnetic field [83]. A sketch of the effect of chromatic aberration is depicted in figure 3.3 d), where the different colored lines represent the different kinetic energies of the electrons like in the light microscopy. The fourth main aberration in electron microscopy is shown in figure 3.3 c) and is named "coma". Here, off axis electrons propagating through various zones of the lens are focused at different positions shifted with respect to each other in the image plane. The resulting spot size of each focus point is different, resulting in a spot with a tail.

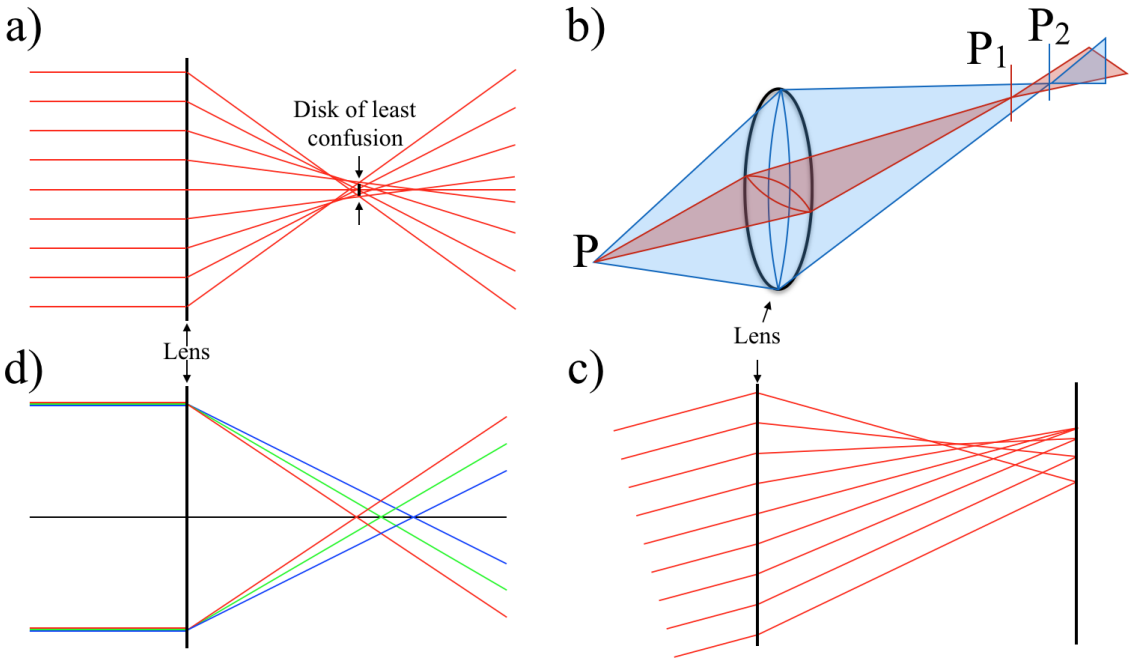

Figure 3.3: a) Spherical aberration with marked disk of least confusion. b) Astigmatism with marked focal length in horizontal (red) and vertical (blue) plane of the lens. d) Chromatic aberration for three electrons with different acceleration voltage ($V_{blue} > V_{green} > V_{red}$). c) Coma shown for various electrons propagation through different regions of the lens.

3.5 HAADF Image Formation using a STEM

The results presented in chapter 5, 6 and 8 where acquired using a double C_s-corrected JEOL JEM 2200 FS. During the experiments the microscope was exclusively operating in STEM-mode. The schematic ray path in STEM-mode is shown in figure 3.4. In the following, the individual parts are explained from the top to the bottom. The JEM 2200 FS has a Schottky field emission gun (FEG) as an electron source [84]. This type of gun is a combination of a thermionic and field emission source. By heating a tungsten wire at 1700 K and applying a intense electric field at the same time, electrons are extracted from the tip and form a bright e-beam with a stable current [85]. The following condenser lens (CL) system allows the intensity of the electron beam to be changed. Furthermore, it transfers the beam through the condenser lens aperture (CLA) to the spherical aberration (C_s) corrector. Accordingly, the size of the CLA determines the convergence angle of the e-beam. To minimize the influence of aberrations, the semi-convergence angle was set to 24 mrad in this work [86]. After optimizing the probe shape and size in the C_s corrector, the beam gets deflected by scan coils in a way that is rasters pixel by pixel over the sample. Below the specimen is the ring shaped HAADF detector consisting of a yttrium aluminum perovskite (YAP) scintillator and a light pipe made of solid quartz. A more detailed description of these types of detectors is given in [87]. The sensitivity and the short decay times of around 40 ns makes the YAP detectors a powerful tool for STEM investigations.

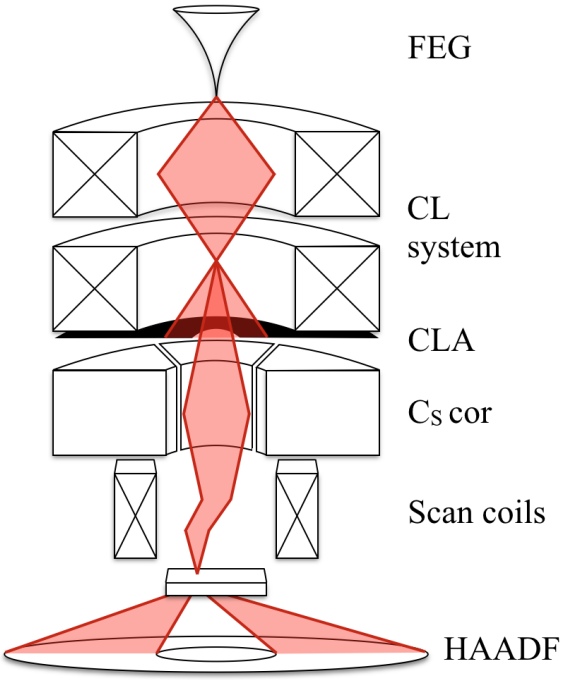

Figure 3.4: Schematic beam path through the microscope in STEM-mode. Only the main components of the image formation process are shown.

CHAPTER 4

The *In Situ* System

In this chapter, firstly a detailed overview of the *in situ* system and the home made gas storage locker will be given. In chapter 4.2, the procedure for pumping/purging the two subsystems when they are not in use will be discussed. Finally, the procedure for performing a helium leak test to ensure the tightness of the system is described step by step in chapter 4.3.

4.1 Introduction

Figure 4.1 shows a sketch of the stainless steel line plan of the *in situ* setup used in this work. On the left hand side the line plan of the manifold, which is designed and produced by Protochips, can be seen [33]. The diameter of the pipes within the manifold is 1/4 inch. The volume of the two experimental tanks (labeled as tank 1 and tank 2) is 0.75 l, whereas the volume of the vacuum tank is 2 l. Vacuum coupling radiation (VCR) metal gasket face seals (Swagelok, Cleveland, OH, USA) with silver-plated stainless steel seals are used to connect the pipes. To evacuate either the manifold themselves or the manifold and the gas storage locker simultaneously a computer controlled pump (labelled as P1) is installed. A detailed workflow of how to use the pump P1 to evacuate both systems at once is given later in the manuscript in chapter 4.2.

The holder, which is also designed and produced by Protochips, is depicted at the lower left part of figure 4.1. The supply line which connects the manifold with the holder has a diameter of 1/32 inch. The return line has also a diameter of 1/32 inch but is interrupted by a capillary with a diameter of 1/64 inch. This reduction limits the flow rate within the holder tip depending on the pressure during a flow experiment. Next to the holder tip an enlarged side view of the assembled environmental (e)-chips with a mounted focussed ion beam (FIB) lamella is shown. The two e-chips consist of Si with 20 nm thick electron transparent SiN windows. Furthermore the thermal e-chip is coated with a SiC membrane,

and varying the applied voltage across this membrane allows for precise control over the temperature of the chip. This design allows investigation at atmospheric pressures of up to 1,000 hPa and temperatures reaching up to 1,000 °C, with a heating rate of up to 5 °C/s.

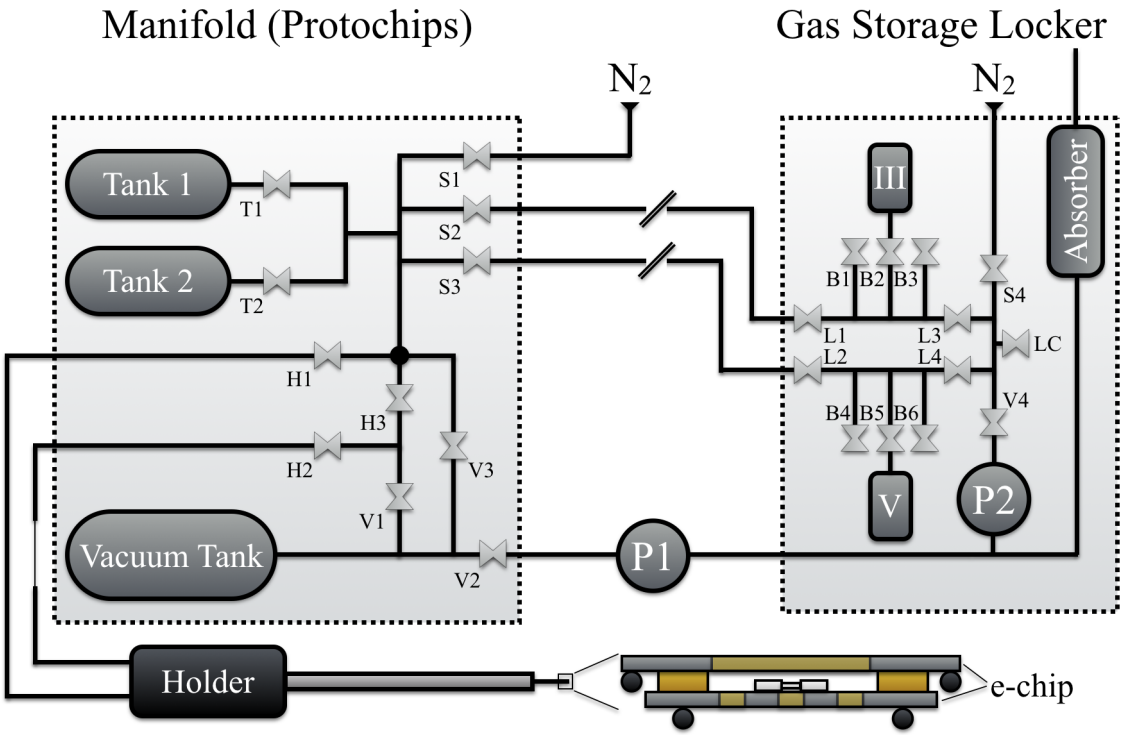

Figure 4.1: On the left hand side a sketch of the manifold line plan is shown. On the right hand side one can see the line plan of the home made gas storage locker. In the lower part of the figure, the holder and the schematic layout of the assembled e-chips with a mounted TEM lamella is presented.

On the right hand side of figure 4.1, the line plan of the home made gas storage locker is presented. As in the manifold the main stainless steal pipes have a diameter of 1/4 inch. The unit provides three ports on the group III and group V side, respectively. These ports are mainly for the precursor container but can also be used to connect gas bottles if other purge and carrier gases are needed. The connection pipes between the precursor container / gas bottles and the according port have a diameter of 1/8 inch. All connections in the gas storage locker are welded where possible. If necessary, VCR metal gasket face seals with silver-plated stainless steel seals are used. To evacuate the gas storage locker separately a pump (labeled as P2) is installed. To ensure that no toxic gases are released into the environment, a mini absorber (CS Cleaning System AG, Ismaning, Germany) is installed in the exhaust pipe. To take fire safety into account the locker complies with DIN 12925. This means that it is fire safe and that all openings close automatically in case of a fire inside the locker. Furthermore, an external ventilation system ensures that

no toxic gases are released into the air. The connection between the gas storage locker and the manifold is realized by two 15 m long pipes with a diameter of 1/8 inch. Due to this length, one needs to take special care during the helium leak check as described later in the manuscript in chapter 4.3. The two units form a closed system where ultra pure nitrogen is used as a purge and carrier gas. If necessary, it is possible to switch the purge and carrier gas to argon or an argon hydrogen mixture (4 % H), respectively. To further ensure safety during the whole process of gas transfer to the manifold and during the experiment, the systems are monitored by gas sensors (Dräger, Lübeck, Germany).

4.2 System Pump Purge

To clean the system and reduce the oxygen level continually, it is important to pump purge the system when it is not in use. In order to avoid the risk of a window failure during the pump purge, it is advisable to assemble the holder with the windowless e-chips before starting the cleaning process. To pump purge the home build gas storage locker simultaneously to the manifold, it is necessary to manipulate the system before starting the process. It should be mentioned that it is important to ensure that no residual gases, which might create a dangerous mixtures, are in the gas lines connecting the manifold with the gas storage locker. By disconnecting the electrical connection of valve S2 and valve S3, and opening the pneumatic bypass between S1, S2 and V1, one can force the system to open the valves S1 and S2 simultaneously with valve V1 during the pump purge process. A detailed sketch of the system line plan and all valves is shown in figure 4.1. After starting the pump/purge from 0.4 hPa to 1,000 hPa, the whole system gets cleaned. To reduce carbon contamination, the holder should be stored in an evacuated pumping station during this process.

4.3 System Leak Test

To ensure that toxic gases do not distribute into the air and to avoid oxygen contaminations in the system, it is necessary to check the tightness of every pipe fitting periodically using a helium-leak-test machine. To provide reliable measurements, it is recommendable to check the gas storage locker, the manifold and the holder separately. Before connecting the helium-leak-test machine, the system needs to be at atmospheric pressure and in a nitrogen environment. The connection port for connecting the test device to the gas storage locker is labelled with (LC) in figure 4.1. Due to the manual valves, one can just follow the regular testing procedure.

The software controlled valves of the manifold need a further manipulation to enable a leakage test of this subsystem. To realize this manipulation, one needs to connect

the helium-leak-test machine to the exhaust pipe of the manifold instead of the pump P1 (compare figure 4.1). Furthermore it is necessary to block the original pump of the manifold with a blind flange. By starting a software controlled pump down of the whole manifold to 0 hPa and at the same time starting the test device, one is now able to pump down the system using the helium-leak-test machine instead of the regular pump P1. To circumvent any error messages, it is important to start the evacuation directly after starting the pump down in the software. After reaching the recommended vacuum, one is now able to check the tightness of every pipe fitting of the manifold and the boom.

To shorten the gas path and therefore enable a faster and more precise measurement, it is advisable to check the tightness of the holder separately from the rest of the system. Therefore one need to disconnect the holder from the manifold and remove the e-chips, so that the holder tip is open against the environment. After connecting the helium leak check machine to the top of the pumping station and separating the upper part of the pumping station from its pump, one is able to evacuate the pumping station and holder by using the helium-leak-test machine. Here, it is particularly important to carefully check the tightness of the pipe fittings of the 1/64 inch capillary.

CHAPTER 5

Experimental Preparation and Performance Check

In this chapter a detailed description of the preparation process of a TEM lamella for later use on the thermal e-chip is given. Next, the actual task of placing the lamella at zone axis on the thermal e-chip and removing residual tungsten from the welding of the lamella to the thermal e-chip is described in detail. Standard FIB lamella preparation will not be discussed here and can be found for example in [88]. Finally, the first system check is presented in this chapter.

5.1 Preliminary E-Chip Preparation

Before loading the thermal e-chip, both chips should be carefully examined for any kind of damage. Special care must be taken that the SiN window does not have damage or any kind of contamination. Furthermore, one should clarify that the back sides of the chips do not have any production faults since this is the area where the gasket is positioned to seal the assembled cell. To ensure that the SiC membrane is in the right resistance range and therefore a precise temperature control during the experiment is possible, one should assemble the cell and check the resistance of the membrane before loading the thermal e-chip. After ensuring the functionality of the thermal e-chip, both chips should be cleaned in a plasma cleaner for around 10 minutes. This ensures, that possible left over carbon contamination from the manufacturing process is removed. It was found that either ArO_x or pure Ar plasma works for the cleaning of the e-chips.

5.2 Focussed Ion Beam System

The samples investigated in this study were prepared with the JIB-4601 F dual beam system produced by JEOL GmbH. A simplified sketch of the geometry of the setup is shown in figure 5.1. The system consists of a scanning electron microscope (SEM) and a FIB column at an angle with respect to the SEM of 53°. With the help of accelerated and focussed Ga ions within the FIB column, it is possible to precisely remove material through ion bombardment. To protect the area of interest and avoid Ga implantation, two gas injection systems (GIS) with either carbon or tungsten are attached to the system. The protective layer can be deposited with both columns depending on the task. Moreover the manipulator needle (Kleindiek Nanotechnik GmbH) enables the operator to lift a slice of material from any position of the sample. A detailed description of the specific lifting and thinning process required for *in situ* STEM investigation is given in [41, 88]. In addition, a detailed description of the used dual beam system including all particularities is given in the following section of the manuscript.

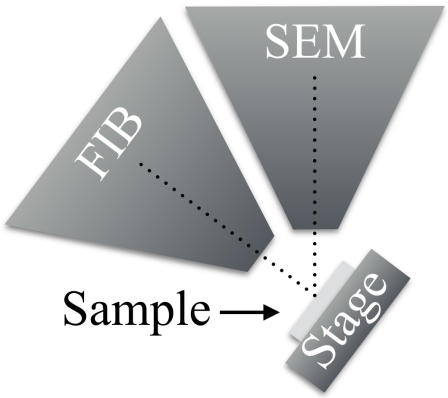

Figure 5.1: Sketch of the geometry of the dual beam system FIB JIB-4601 F which consist of a SEM and FIB columns at an angle of 53° with respect to one another

5.3 FIB Preparation and Loading Process

The SEM image in figure 5.2 a) shows the lamella welded to the TEM grid. To fit the lamella between the two e-chips and avoid any damage to the SiN windows, the lamella has to be thinner than 2 μm in the dimension indicated by the two white arrows. Furthermore, to ensure that the finished lamella lies precisely perpendicular to the zone axis of interest on the thermal e-chip, one needs to ensure that the side facets of the lamella are perpendicular to the zone axis. In this example the zone axis of interest is the [100] as indicated in the image in figure 5.2 a). The best way to achieve this is to rotate the substrate before deposition of the first protection layer in such a way that the zone axis of interest is precisely aligned vertically in the SEM image as shown in the inset in figure 5.2 a). From then on, one needs to take special care to lift the lamella without any rotation along this axis. After welding the TEM lamella to the copper grid, which should be aligned along the horizontal axis of the SEM image, an etching tool which etches horizontal to the SEM image must be used to shape the lamella as shown in figure 5.2 a). As well as the angle between the zone axis and the long axis of the lamella, one needs to align

the angle between the zone axis and the side facets in the depth direction as indicated in figure 5.2 b). Here, one needs to take the cone shape of the focussed Ga-beam into account. Previous studies have revealed that the best results have been achieved by tilting the lamella 1° with respect to the lower edge in the beam direction. Due to the single tilt capability of the *in situ* holder, a slight error in this angle can be corrected later during the investigation. The finished lamella with the electron transparent part in the middle is shown in figure 5.2 c). The U-shape of the lamella with the electron transparent part well secured between the thick regions is particularly suitable for deposition on to the thermal e-chip. Furthermore this shape enables the possibility to weld the lamella on three sides to the SiC membrane, which results in a very strong bond between the two parts and therefore enables a good thermal connectivity. The SEM image d) shows the lamella rotated 90° along its long axis. In this geometry the aforementioned side facet of the lamella is parallel to the thermal e-chip, which is also fixed to the SEM stage. A detailed description of the holder geometry used for this step is given in [41]. Care should be taken to rotate the TEM grid and the attached lamella in such a way that the longer sided facet faces down as depicted in the sketch in figure 5.2 d). By doing so, one has a suitable edge which is in direct contact with the SiC membrane and ensures a stable welding seam between the lamella and the membrane surface. Due to the small size of the lamella, it is not possible to see which side is the longer one with the stereomicroscope after removing the lamella from the FIB chamber. One must therefore correlate the front and the back side of the TEM grid with the shorter and longer side of the lamella, before exchanging the lamella. Due to the larger scale of the TEM grid it is possible to distinguish the front and the back side outside the FIB. To place the lamella onto the surface of the thermal e-chip, one needs to attach the manipulator needle as shown in figure 5.2 d). It is essential to omit the electron transparent part of the lamella during image generation with the Ga-beam. In order to be able to see both edges of the lamella even after the lamella is welded to the needle and not movable, one can use the beam shift function of the FIB to "move" around the area of interest. By doing so, one is able to first weld the needle to the appropriate position and then "move" to the other side of the lamella and cut it free from the TEM grid without penetrating the electron transparent region with the Ga-beam. The SEM image in figure 5.2 e) shows the lamella slightly above its final position on the thermal e-chip. Due to the aforementioned geometry alignment the lamella is now perfectly parallel to the surface of the SiC membrane and one is able to gently lay it down by aligning the electron transparent part directly over one SiN window. As mentioned above, the cone shape of the Ga-beam introduces a larger error in the angle between the zone axis and the surface of the lamella in depth direction (see figure 5.2 b). To correct this misalignment the thermal e-chip is rotated in such a way that the single tilt capability of the *in situ* holder can be used to correct this error. The final step consists of

removing the manipulator needle from the lamella carefully. Throughout that process one needs to avoid etching through the lamella and destroying the SiC membrane. The inset in figure 5.2 e) enables a top view on the lamella. Here the brighter overlapping areas are the tungsten depositions which holds the lamella in place. To prevent any bending during the later heating experiments, it is recommended to weld the lamella on three sides to the SiC membrane. Unfortunately the tungsten deposition leads to a uniform coverage of tungsten over the whole area and this is especially undesirable in the region of the electron transparent part of the lamella. Furthermore, the limited tilting capability of the SEM stage does not allow the tilting of the lamella enough in Ga-beam direction to result in an angle between the Ga-beam and the surface of around $4° - 7°$. To repolish the area of interest and remove surplus tungsten, one needs to mount the thermal e-chip on a pre tilted SEM stage (see figure 5.2 f). In addition, the chip needs to be mounted in such a way that the electron transparent part of the lamella is facing upwards as depicted in the inset in figure 5.2 f). By using a very low acceleration voltage and a gentle beam, one is able to remove the excess tungsten without destroying the SiC membrane as well as the SiN window.

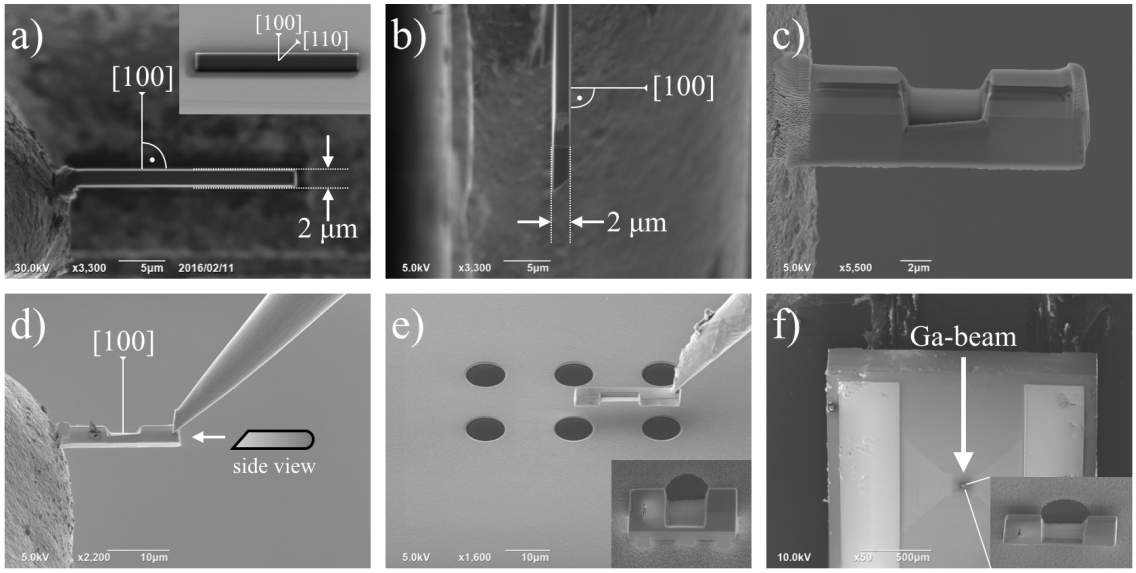

Figure 5.2: SEM image a) shows a top view of the TEM lamella mounted on the copper grid. A view of the front face of the lamella is shown in b). The finished lamella with the electron transparent part in the middle is shown in c). Image d) shows the lamella and the manipulator needle in the rearranged position for placement on to the thermal e-chip. Image e) shows the lamella slightly above the thermal e-chip. To polish the mounted lamella, the chip needs to be arranged as shown in the image f).

5.4 Preliminary System and Holder Preparation

To prepare the system for an experimental session, it is first necessary to stop the pump purge and fill all system pipes with nitrogen up to 1 atm. Furthermore, it is important to reconnect the electrical contacts of valves S1 and S2 and disconnect the pneumatic bypass between valves S1, S2 and V1 (see figure 4.1). As described in chapter 4.2, this home made bypass is necessary to pump purge the whole system and the gas storage locker at once. However, the gases can accidentally mix and harm the manifold if the bypass is not disconnected before starting an experiment. One can now safely disconnect the holder lines from the system and disassemble the holder tip after unloading the holder from the pump station. To remove any leftover carbon residuals, it is recommended to plasma clean all holder parts except the O-ring for around 10 minutes. After inspecting the O-ring, one can assemble all parts without using any kind of vacuum grease and tighten the screws with the torque wrench ($\approx 0.53\,\mathrm{N}$). In the following steps the electrical contact of the SiC membrane and the tightness of the holder must be checked. Therefore it is necessary to plug in the holder cable and load the holder into the pump station and evacuate it. The most reliable process to ensure the tightness of the holder is to start a pump purge of the holder tip between (1 - 600) hPa and monitor the pressure of the pumping stage during the cycles. If the pressure within the pumping stage stays constantly below $10^{-7}\,\mathrm{hPa}$ during the pump purge cycles one can be sure that the holder tip is sealed. To clean the assembled cell further it is recommended to pump purge the holder for at least one night between (0.4 - 600) hPa. During this last cleaning step it is suggested, to just pump purge the holder cycle isolated from the rest of the system. By doing so, one ensures that the clean system does not get in contact with contamination enclosed in the cell during assembling. If possible, one can also set an increased temperature on the thermal e-chip to efficiently remove any leftover carbon contamination and humidity.

5.5 Performance Check

To confirm that the procedure described above indeed facilitates the obtainment of zone-axis orientations of cross-section samples of single crystalline specimens in a single-tilt *in situ* holder, figure 5.3 a) and b) show comparable STEM images of the same sample. Here, the STEM image depicted in figure 5.3 a) was recorded in a conventional double tilt holder before the sample was transferred onto the thermal e-chip, whereas the STEM image displayed in figure 5.3 b) was recorded during the *in situ* investigation at 220 °C and 1,000 hPa of N_2 environment. The crystalline structure is shown on the right hand side of figure 5.3 a). In this image the different contrast between the Ga- and P-columns along the [100] zone-axis is clearly visible as indicated in the inset shown in figure 5.3 a).

Moreover, there is a strong difference in the intensity between the GaP region and the Ga(N,As,P), which results from the high As content in the quaternary material.

As one can see in the comparable STEM image depicted in figure 5.3 b), despite the elevated temperature, the N_2 environment, and the two SiN windows which have a total thickness of around 50 nm, it is possible to investigate the material under atomic resolution conditions inside the single-tilt *in situ* holder. This proves that it is possible to achieve zone-axis orientation of the sample through very accurate FIB preparation as presented in the text above. However, the direct comparison of the two insets show that the contrast of the STEM image recorded in the *in situ* holder becomes slightly worse and the P-columns are not visible which may be caused by the higher background intensity and a slight mistilt of the lamella.

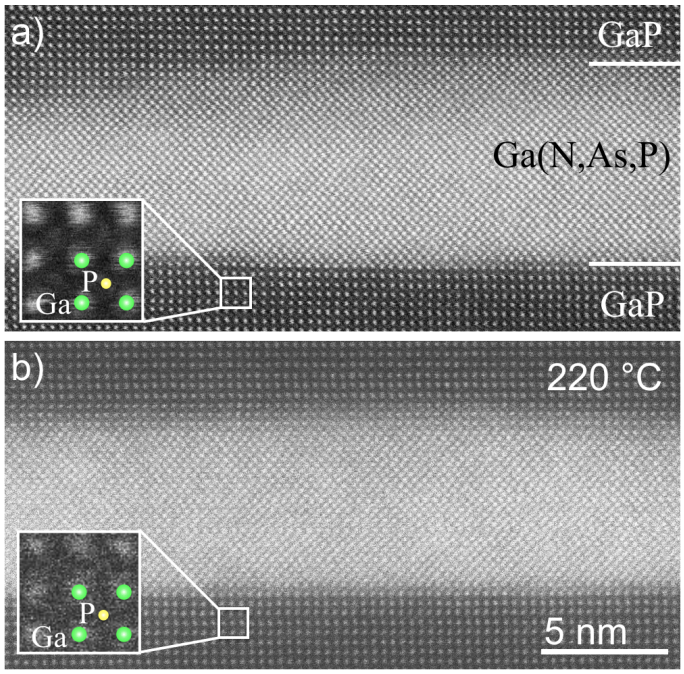

Figure 5.3: (a) STEM image of a FIB lamella before depositing the lamella in the environmental cell. b: STEM image of the same lamella in the cell at 220 °C and 1,000 hPa of N_2 environment. Four unit cells are shown enlarged as an inset in both images.

CHAPTER 6

In Situ Investigations

As mentioned in section 2.4, post-growth annealing is an effective way of improving crystal quality since it reduces the number of crystal defects. More importantly, this often leads to an improvement in device performance. The TEM experiments presented in this chapter should verify whether it is possible to study thermal annealing processes of III/V semiconductors in a desired atmosphere to prevent incongruent desorption of group V species. In doing so, the functionality of the setup will also be proven.

6.1 First *In Situ* Thermal Annealing Test on Ga(N,As,P)

The STEM images presented in figure 6.1 (a-c) show the Ga(N,As,P) sample during the unstabilized thermal annealing treatment in a 10 hPa N_2 environment. A detailed explanation of the sample structure is given in chapter 2.5. The single layers of the sample are annotated on the left hand side of the STEM image displayed in figure 6.1 a). In this image one can clearly see that the crystalline arrangement is still intact at 400 °C. Nevertheless, by comparing the STEM images depicted in figure 6.1 a) and figure 6.1 b), significant degradation of the structure at 600 °C is observable. The mechanism which causes the degradation is most likely P desorption due to incongruent desorption. This assessment is also supported by residual Ga droplets on the surface of the lamella. During the following experiments, the droplets move across the surface and begin to cluster on the upper surface of the lamella (see inset in figure 6.1 b). By further increasing the temperature up to 700 °C, the quantum well structure has been completely destroyed as shown in the STEM image figure 6.1 c). In contrast to the aforementioned unstabilized thermal annealing treatment, the STEM images depicted in figure 6.1 d) to f) show the annealing experiment carried out in 140 hPa TBP without additional carrier gas in the system. In this P-rich environment the P in the structure is prevented from desorbing. By comparing the STEM images displayed in figure 6.1 d), 6.1 e) and 6.1 f), one is

not able to see any noticeable destruction of the crystalline arrangement. Moreover, by comparing the STEM images depicted in figure 6.1 d) and 6.1 e) one can even see a slight improvement of the image quality in terms of the homogeneity of the contrast distribution. This effect may be caused by desorption of the amorphous layer, which originates from the preparation process. In summary, the comparison between the STEM images depicted in figure 6.1 a) to c) and d) to f) show a clear difference in the sample stability between the unstabilized and the group V stabilized thermal annealing experiment, and therefore prove the functionality of the *in situ* system introduced above.

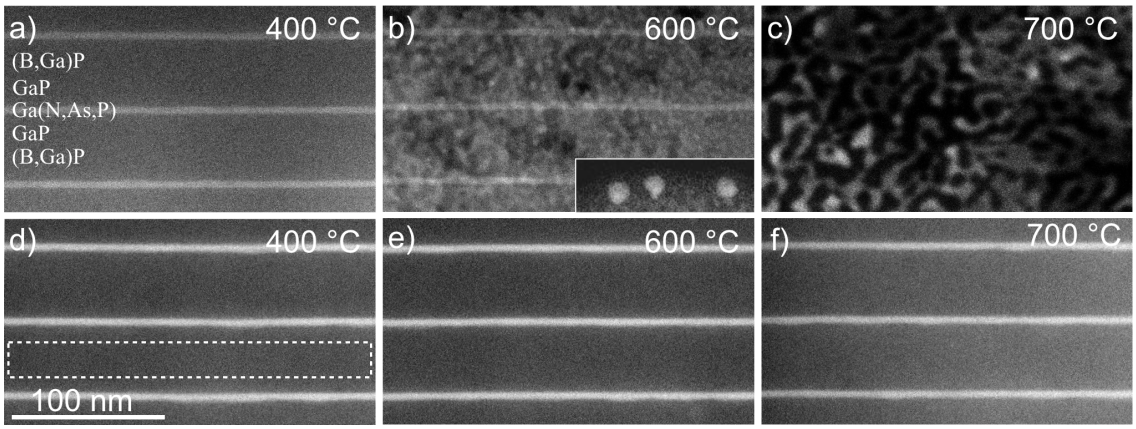

Figure 6.1: a-c: STEM images of the quantum well structure during the unstabilized thermal annealing process in a 10 hPa N_2 environment. In (a), annotated single layers can be seen on the left hand side. At the bottom right of (b) a sub image showing Ga droplets on the upper surface of the TEM lamella is presented. d–f: STEM images of the comparative thermal annealing experiment in a 140 hPa TBP environment.

6.2 Quantitative Analysis of P Desorption

To further investigate group V desorption and therefore the thermal stability of the sample depending on the environment in the *in situ* cell, the remaining TEM sample thickness was measured at each temperature step in the (B,Ga)P region. The corresponding area on the TEM lamella is marked with a dashed box in figure 6.1 d). The influence of the small amount of B ($\approx 3\%$) in the GaP is negligible in the analysis. The graph depicted in figure 6.2 a) shows the resulting thickness values.

It should be mentioned that the HAADF intensities were normalized with respect to the impinging beam following the procedure described in [89]. Furthermore, the contribution of the SiN window to the HAADF intensity was subtracted from the measured intensity of the area of interest. The actual thickness determination was done by comparing the intensity to complementary contrast simulations using the frozen phonon approximation available in STEMsim [90]. It should also be noted that the influence of temperature on

average HAADF intensity is rather small, i.e. a maximum of 0.67 % of the impinging beam intensity at a sample thickness of 200 nm. Nevertheless, the corresponding simulation intensities were used when comparing to the experimental intensities derived from the (B,Ga)P region.

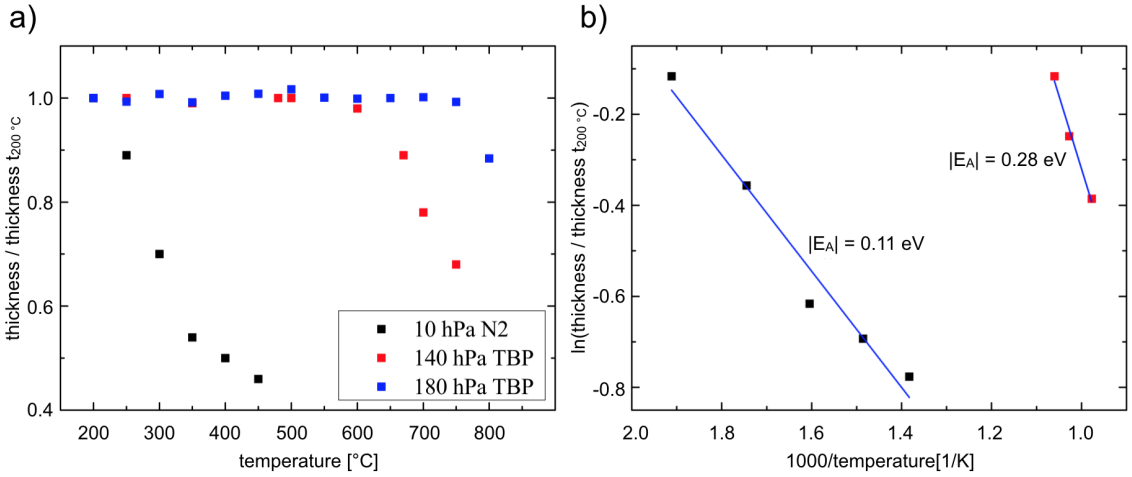

Figure 6.2: The plot (a) shows the thickness divided by $t_{200\,°C}$ depending on the temperature for different environments inside the *in situ* holder. The black data points indicate the thickness change of the sample during the unstabilized annealing investigation. The red and blue data points display the thickness change of the sample during the stabilized annealing in 140 hPa and 180 hPa TBP environments, respectively. The Arrhenius plot (b) shows the thickness divided by $t_{200\,°C}$ of the (B,Ga)P barrier as a function of the annealing temperature for the thermal annealing experiment at 10 hPa N_2 and 140 hPa TBP.

The data points presented in figure 6.2 a) show the derived thickness normalized to the thickness of each sample at 200 °C ($t_{200\,°C}$) as a function of the actual temperature. The black data points are the corresponding results for the unstabilized thermal annealing experiment. The associated STEM images are shown in figure 6.1 a) to c). In contrast, the red data points indicate the thickness change of the sample annealed in a 140 hPa TBP environment (see figure 6.1 d) to f)). To allow the comparison of the sample stability as a function of TBP pressure, the blue data points show the change of the thickness during the thermal annealing in a 180 hPa TBP environment (corresponding STEM images not shown here). By comparing the three processes one can see a significant difference in the starting temperature of the sample degradation and the degradation speed of each sample. Especially by comparing the unstabilized thermal annealing process (black data points) with the two group V stabilized processes (red and blue data points) one can already confirm the successful group V stabilization and therefore the functionality of the system. Furthermore, the greater stability of the sample up to higher temperatures with higher TBP pressure in the cell can also be confirmed by comparing the thickness change indicated by the red and blue data points. To gain a deeper understanding of the

actual desorption process, figure 6.2 b) shows an Arrhenius plot of the thickness divided by $t_{200\,°C}$ of the (B,Ga)P barrier as a function of the annealing temperature. The resulting activation energies are $|E_A| = 0.11\,eV$ for the sample annealed in a 10 hPa N_2 environment and $|E_A| = 0.28\,eV$ for the sample annealed at 140 hPa TBP. These numbers are significantly smaller than what Kobayashi et. al. found for GaP bulk material ($|E_A| = 1.18\,eV$). One possible reason for the deviation is the large surface to volume ratio, which needs to be taken into account for the thin TEM lamella. As such, the exact numbers are not comparable. However, the increase in the activation energy resulting from the P stabilized measurement further supports the statement that group V stabilization plays a crucial role in thermal annealing experiments of III/V semiconductor materials with different vapor pressures.

6.3 Thermally Introduced Bismuth Clustering in Ga(P,Bi) Layers

As already mentioned in chapter 2.5, the structural and optoelectronical properties of Ga(P,Bi) require a detailed growth and post-growth thermal annealing characterization of this material. L. Nattermann et. al. demonstrated how the highly metastable material Ga(P,Bi) could be deposited by MOVPE with fractions of Bi up to 8 % [53]. However, the defect free growth of thick Ga(P,Bi) with a high fraction of Bi without forming Bi clusters is still very challenging. One problem is the different growth temperature of the GaP layer compared to the Ga(P,Bi) layer. To incorporate high fraction of Bi it is necessary to grow the material at rather low temperature in terms of MOVPE of 400 °C. In contrast, former studies on GaP investigating the defect density and interface quality have shown that the optimal growth temperature of GaP is at around 625 °C [91]. Consequently, this results in a thermal treatment of each Ga(P,Bi) layer during the growth of the following GaP layer in a structured sample as is shown in chapter 2.5.

Due to the setup introduced in chapter 4 it is now possible to investigate structural changes during a thermal treatment *in situ* under high resolution conditions. Moreover, the investigations described in chapter 6.1 have proven that the setup is able to facilitate the experiments in an environment where incongruent desorption of group V species can be suppressed up to the growth temperature regime of MOVPE processes. It should be pointed out that due to the large difference in the surface to bulk ratio, the absolute values for the initial temperature at which the clustering takes place in the MOVPE process and inside the *in situ* cell may vary a little and are not directly comparable. Nevertheless, the trend is the same and therefore the investigation presented in the following sections allows *in situ* investigation of a specific MOVPE process inside the TEM under high resolution conditions.

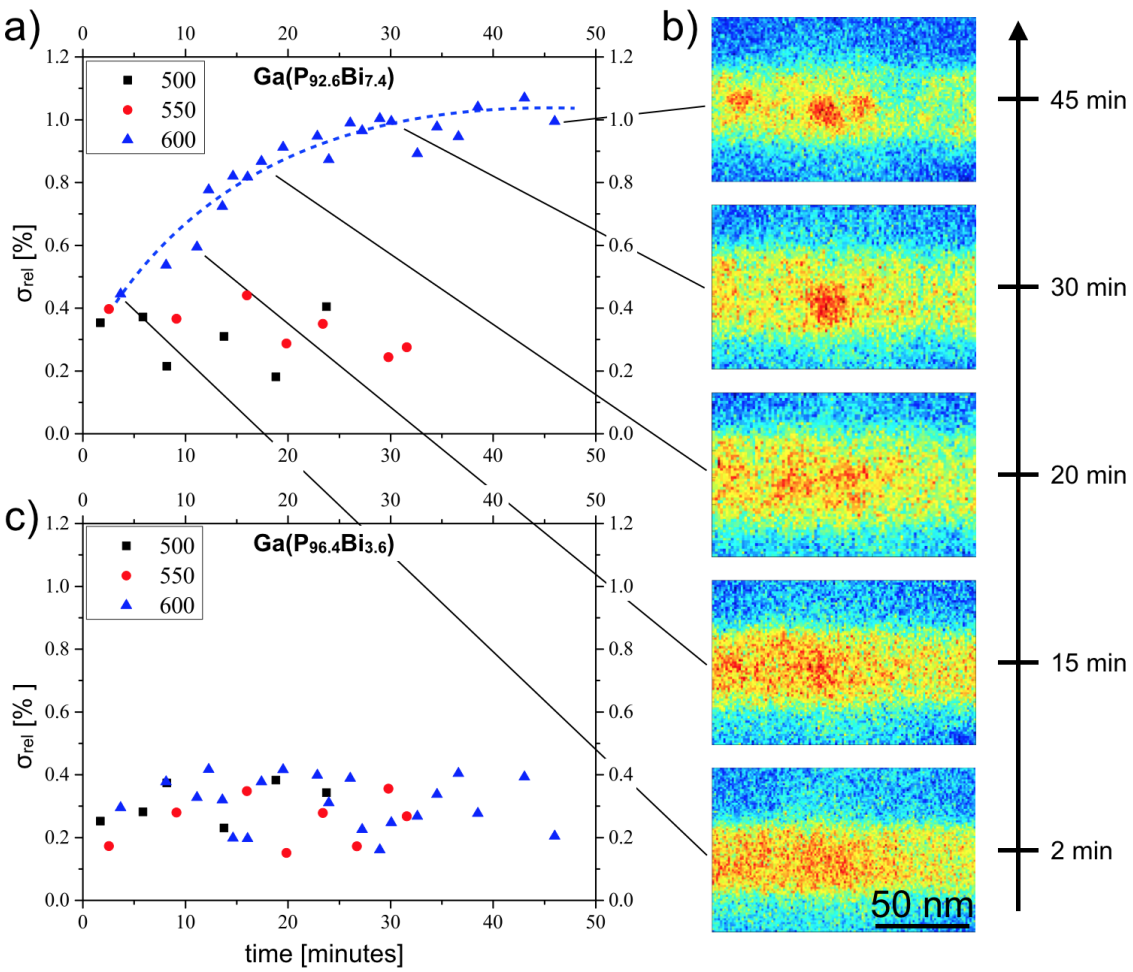

Figure 6.3: Plot (a) and (c) show σ_{rel}, i.e. the standard deviation of the intensity within the ternary Ga(P,Bi) layer divided by the mean intensity of the surrounding GaP matrix, as a function of time within the Ga(P,Bi) layer with 7.4 % and 3.6 % Bi, respectively. The temperature series were carried out at 500 °C (black squares), 550 °C (red dots) and 600 °C (blue triangles). The colour coded STEM images (c) show the formation of one big and two smaller Bi clusters within the Ga($P_{92.6}Bi_{7.4}$) layer over time

To ensure no contribution of sample degradation due to group V desorption, the results presented in figure 6.3 are carried out under a 180 hPa TBP environment. As depicted in figure 6.2 under this condition the sample shows no degradation up to approximately 750 °C. The measured standard deviation of the intensity within the ternary Ga(P,Bi) layer divided by the mean intensity of the surrounding GaP matrix, hereinafter designated as σ_{rel}, is a measure for the inhomogeneity of the Bi distribution of the corresponding Ga(P,Bi) layer, as has been shown on the example of Ga(N,As,P) by Wegele and co workers [92]. Figure 6.2 a) and c) show σ_{rel}, as a function of time within the Ga(P,Bi) layer with a Bi fraction of 7.4 % and 3.6 %. For every series the temperature was kept constant for 30 and 45 minutes, respectively. The HAADF STEM images recorded during every series

in two minute cycles are the basis for the Bi clustering study. The corresponding data for the σ_{rel} value within the Ga($P_{92.6}Bi_{7.4}$) layer for the three temperature steps is depicted in plot a) in figure 6.3.

By taking a look at the data points of the 500 °C and 550 °C time series, no increase in σ_{rel} can be observed. This leads to the conclusion that no local Bi enrichment takes places in this temperature regime. It should be mentioned that both temperatures are above the MOVPE growth temperature of 400 °C. By further increasing the temperature to 600 °C one can see the influence of the temperature on σ_{rel} within the Ga($P_{92.6}Bi_{7.4}$) layer which originates from Bi clustering. Figure 6.3 b) show color coded STEM images of the Bi cluster formation process over the time. It should be emphasized that post *in situ* energy dispersive X-ray spectroscopy (EDX) measurements confirmed that the cluster appearing in the STEM images consists of Bi. The time passed with respect to the start of the experiment at which each image is recorded is indicated at the very right hand side. Furthermore, the black lines between the plot (a) and (b) relate the STEM image with the corresponding data point. To further clarify the initial clustering temperature depending on the Bi fraction, plot c) in figure 6.3 shows σ_{rel} plotted agains time for a Ga(P,Bi) layer with a fraction of 3.6 % Bi. As one can see, no Bi enrichment could be observed for all three temperature series, i.e. 500 °C, 550 °C, and 600 °C, respectively.

The results presented in figure 6.3 indicate that the Bi containing layer grows without Bi clustering and the growth of the following GaP layer, which acts like a thermal treatment for the Ga(P,Bi) layer, leading to inhomogeneity of the Bi distribution. It should be emphasized one more time that there might be a difference between the initial cluster temperature for the thin TEM sample compared to the bulk material in the MOVPE machine.

6.4 First GaP Growth Experiments on Si Nanoparticles

In addition to the aforementioned stabilized thermal annealing experiment, GaP growth on Si was also investigated in the framework of this thesis. To enable a efficient substrate preparation, this investigation was done on Si nanoparticles. The nanoparticle were produced by G. Mannino and co workers by inductively coupled plasma chemical vapor deposition [93]. The electron transparent tip of one octahedral Si nanoparticle is shown in figure 6.4 a). The orientations of the crystalline side facets are marked at the corresponding position.

Unfortunately, the storage of the nanoparticles in isopropanol and the deposition on the thermal e-chip in air results in a approximately 20 nm thick SiO_x shell around the crystalline core of the particles. To achieve heteroepitaxial growth on the crystalline surface of the Si it is indispensable to remove the amorphous shell. The graph depicted

in figure 6.4 b) shows the thickness of the amorphous SiO_x layer along three sides of one particle depending on the annealing time in an $ArSiH_4$ (4 % SiH_4) environment at 1000 °C. As one can see it is possible to reduce the thickness of the amorphous layer by approximately 25 % within 7-8 minutes. To ensure no residual SiO_x layer remains, this cleaning procedure was carried out for one hour before starting the growth experiment.

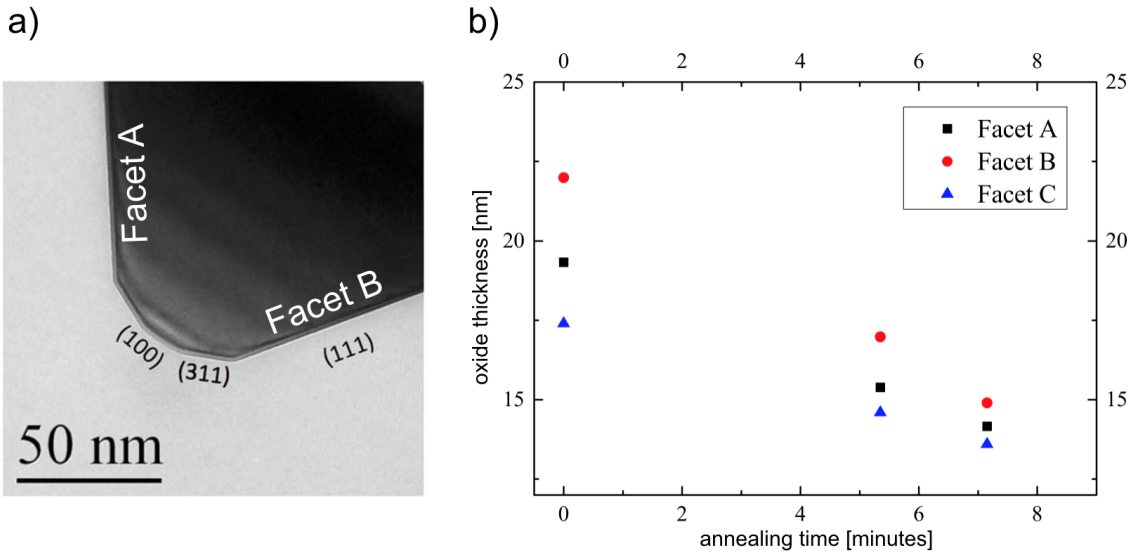

Figure 6.4: a) TEM image of a Si nanoparticle used as Si substrate for the GaP growth experiments on Si [93]. The crystal orientation of the side facets are labeled in the micrograph. b) shows the reduction of the SiO_x layer depending on the annealing time in an $ArSiH_4$ (4 % SiH_4) environment at 1000 °C.

The results of one of the first GaP growth experiments can be seen in figure 6.5. During this experiment, small amounts of TMGa were firstly inserted into the *in situ* cell and by varying the temperature in a range of 400 °C to 700 °C, it was possible to control the amount of decomposed TMGa. This was done until a certain amount of liquid Ga was on top of the Si nanoparticles. After a few pump purges with ultra pure nitrogen, small amounts of TBP were inserted into the cell and the temperature was again varied in the range mentioned before. This procedure was repeated for varying amounts of TMGa, TBP, and temperature until a layer was formed on the Si nanoparticles. Unfortunately, due to the formation of a thick carbon layer during the experiment, is was not possible to investigate the grown structure *in situ* under high resolution conditions. This C layer most likely results from the precursor molecules [94].

Post *in situ* investigation in a standard double tilt holder should verify the exact composition of the grown layer. Figure 6.5 a) shows the HAADF overview image of the investigated Si nanoparticle. The grown GaP layer as well as the C layer is marked with GaP and C, respectively. The images depicted in figure 6.5 b), c) and d) present the color

coded EDX results of P, Ga and O. By overlaying the images shown in figure 6.5 a), b) and c) (overlay not shown here), one can confirm that the bright layer labeled with GaP in image a) consists of GaP. Furthermore, by overlaying the all four images depicted in figure 6.5, one can also see that there is still a lot of oxygen contamination during the experiment in the *in situ* cell.

This results prove that it is possible to investigate III/V semiconductor growth *in situ* in the TEM.

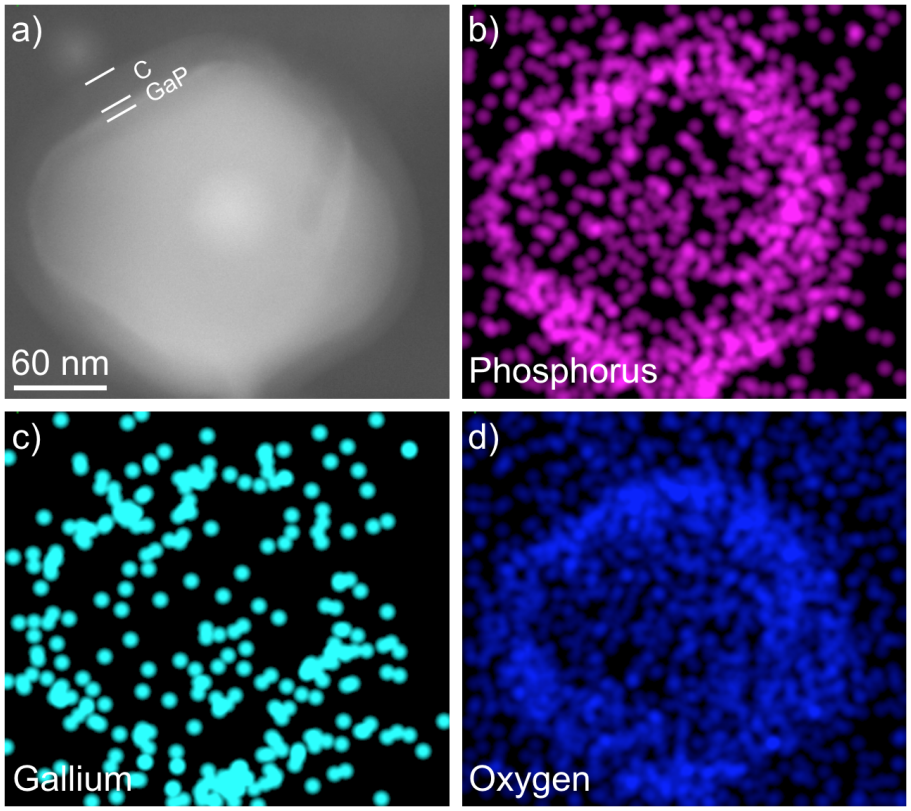

Figure 6.5: a) HAADF image of the Si nanoparticle after the GaP growth experiment. The GaP and C layers are labeled with GaP and C, respectively. b), c) and d) show the result of the post-growth EDX measurement. The investigated atom species are indicated at the lower left corner of the images b), c) and d).

CHAPTER 7

Summary and Outlook

This chapter sums up the needed modifications to the *in situ* system in order to insert potentially toxic and pyrophoric III/V semiconductor precursors into the TEM. Furthermore, the results from the experiments using this setup are summarized.

In order to handle toxic and phyrophoric precursors inside a TEM and therefore facilitate group V stabilized thermal annealing experiments, significant changes of the original *in situ* system (designed and produced by Protochips) are necessary. To further ensure safely when storing and transfering the precursors gases from the storage container to the manifold, a home made gas storage locker was built. Moreover, to prevent any type of contamination and ensure no precursor distributes into the air, the locker and the manifold form a closed system in which ultra pure N_2 is used as a carrier and purge gas. If necessary it is possible to switch to pure Ar or a ArH_2 ($4\,\%\,H_2$) mixture as carrier and purge gas. The home made gas storage locker provides three ports on the group III and group V side, respectively. These ports are mainly for the precursor container but can also be used to connect gas bottles if other purge and carrier gases are needed. All connections in the gas storage locker are welded where possible. If necessary, vacuum coupling radiation (VCR) metal gasket face seals with silver-plated stainless steel seals are used. To ensure that no toxic gases are released into the environment, a mini absorber is installed in the exhaust pipe. To take fire safety into account the locker complies with DIN 12925. This means that it is fire safe and that all openings close automatically in case of a fire inside the locker. Furthermore, an external ventilation system ensures that no toxic gases are released into the air. To further ensure safety during the whole process of gas transfer to the manifold and during the experiment, the systems are monitored by gas sensors.

To be able to investigate cross-sectional samples of metal organic vapor phase (MOVPE) grown crystalline structures under atomic resolution condition inside the *in situ* cell holder which has just single tilt capabilities, it is necessary to deposit a electron transparent focussed ion beam (FIB) lamella precisely perpendicular to its zone axis on the thermal

e-chip. To realize this geometry a reproducible FIB preparation technique was developed, which results in a partial electron transparent lamella perfectly aligned perpendicular to the selected zone axis. Moreover, the electron transparent part of the lamella is well protected between the thicker areas which prevent bending of the area of interest during the thermal treatment. The first performance checks prove that it is possible to achieve atomic resolution due to the accurate FIB preparation presented in this work.

To check the functionality of the system and prove that it is possible to investigate group V stabilized thermal annealing processes under high resolution condition, two annealing series of a Ga(N,As,P) sample were performed. During the first series N_2 was present in the *in situ* holder, while the second series of measurements were carried out in a tertiarybutylphosphine (TBP) environment. The sample annealed in a TBP environment shows favorable thermal stability up to 500 °C compared to the unstabilized sample, which begins to degrade at less than 300 °C. Subsequent data analysis was able to track the P desorption from the material by measuring the thickness of the sample during thermal annealing with and without stabilization. This analysis enables the possibility to calculate and compare the activation energy (E_A) of the P for the unstabilized and group V stabilized thermal annealing treatment.

Further investigation on the initial Bi cluster formation temperature and the cluster characteristic in terms of cluster size and formation time is determined by analysing the intensity distribution within Ga(P,Bi) layers with different fractions of Bi for three temperature series covering the MOVPE growth temperature regime. Due to the possibilities of the developed setup and the gained knowledge from the P desorption experiments on Ga(N,As,P), it was possible to study the dynamic Bi clustering processes in an environment which ensures that the results are not distorted by any destructive behavior of the crystal during the thermal treatment.

In addition to the group V stabilized thermal annealing experiment, GaP growth on Si was also investigated in the framework of this thesis. For these experiments facetted Si nanoparticles served as the Si substrate. By annealing the particle in an $ArSiH_4$ (4 % SiH_4) environment at 1000 °C for one hour, it was possible to remove the amorphous SiO_x shell around the crystalline core. These first results prove that it is possible to grow GaP on Si inside the *in situ* cell; nevertheless, the growth parameters need further investigation to enable high quality growth of GaP on Si under high resolution conditions.

7.1 Outlook

The focus of this work was to create the foundation for a new field of *in situ* research on III/V semiconductor materials. With the developed system it is now possible to further investigate MOVPE processes without the need of taking any destructive behavior of the crystalline sample due to group V desorption into account.

In terms of *in situ* thermal annealing experiments the results presented in this work are just the beginning and only scratching the surface of the potential applications. Further investigation at even higher resolution should be possible to investigate dynamic processes under atomic resolution conditions. Moreover, by further refinement of the FIB target preparation and placing a dislocation exactly in the electron transparent part of the lamella, investigation of dynamic processes of dislocation during the thermal treatment should be possible.

Another possibility is the investigation of actual growth processes *in situ* under high resolution conditions. Preliminary experiments, presented in the section 6.4 of this thesis, have shown that it is possible to investigate GaP growth on Si. Nevertheless, a lot of open questions concerning the amount of gas, the temperature and the substrate preparation inside the closed *in situ* cell need to be answered before a controlled crystal growth is possible.

CHAPTER 8

Scientific contributions

8.1 Preparation and Loading Process of Single Crystalline Samples into a Gas Environmental Cell Holder for *In Situ* Atomic Resolution Scanning Transmission Electron Microscopic Observation

Citation

R. Straubinger, A. Beyer, and K. Volz. Preparation and Loading Process of Single Crystalline Samples into a Gas Environmental Cell Holder for *In Situ* Atomic Resolution Scanning Transmission Electron Microscopic Observation. *Microscopy and Microanalysis*, 22(3):515–519, 2016[41]

Abstract

A reproducible way to transfer a single crystalline sample into a gas environmental cell holder for *in situ* transmission electron microscopic (TEM) analysis is shown in this study. As *in situ* holders have only single-tilt capability, it is necessary to prepare the sample precisely along a specific zone axis. This can be achieved by a very accurate focused ion beam lift-out preparation. We show a step-by-step procedure to prepare the sample and transfer it into the gas environmental cell. The sample material is a GaP/Ga(NAsP)/GaP multi-quantum well structure on Si. Scanning TEM observations prove that it is possible to achieve atomic resolution at very high temperatures in a nitrogen environment of 100,000 Pa.

Contributions

My contribution to this work was the planning and the development of the preparation technique introduced in this paper. In addition, I carried out all FIB preparations and

STEM investigations. Andreas Beyer helped to develop the preparation technique. Kerstin Volz supervised the work and secured the funding to support this study. All authors reviewed the manuscript.

Microsc. Microanal. 22, 515–519, 2016
doi:10.1017/S1431927616000593

Microscopy AND Microanalysis

Preparation and Loading Process of Single Crystalline Samples into a Gas Environmental Cell Holder for *In Situ* Atomic Resolution Scanning Transmission Electron Microscopic Observation

Rainer Straubinger,* Andreas Beyer, and Kerstin Volz

Faculty of Physics & Materials Science Center (WZMW), Philipps-Universität Marburg, 35032 Marburg, Germany

Abstract: A reproducible way to transfer a single crystalline sample into a gas environmental cell holder for *in situ* transmission electron microscopic (TEM) analysis is shown in this study. As *in situ* holders have only single-tilt capability, it is necessary to prepare the sample precisely along a specific zone axis. This can be achieved by a very accurate focused ion beam lift-out preparation. We show a step-by-step procedure to prepare the sample and transfer it into the gas environmental cell. The sample material is a GaP/Ga(NAsP)/GaP multi-quantum well structure on Si. Scanning TEM observations prove that it is possible to achieve atomic resolution at very high temperatures in a nitrogen environment of 100,000 Pa.

Key words: STEM, FIB preparation, III/V semiconductor, environmental cell, *in situ*

Introduction

Various functional materials require *in situ* information to optimize growth conditions. Consequently, techniques which are capable of determining the structure of materials should also be applied during growth to study formation of the structures under investigation. Aside from facilitating optimization of the growth of functional materials, this also gives important insights into growth kinetics. The number of publications on *in situ* transmission electron microscopic (TEM) techniques and studies have consequently risen significantly in the last few years (Suzuki et al., 1998; Hugo et al., 2003; Legros et al., 2008; Birajdar et al., 2012; Nielsen et al., 2013; Morrow et al., 2014; Imrich et al., 2015).

Before the development of gas cell specimen holders, *in situ* TEM was only possible by using environmental (E) TEMs, which are also able to study *in situ* reactions under high-resolution conditions (Boyes & Gai, 1997; Hofer et al., 1997; Schaffer et al., 2004; Kishita et al., 2009). Nevertheless, the most important drawback of the ETEM is the long gas path through which the electron beam must pass in the upper and lower region of the specimen (around 1 cm). This limits the resolution and, consequently, the pressure limit for high-resolution investigations is around 1,300 Pa (Allard et al., 2012). Furthermore, deposits of precursor gases can affect the microscope.

Closed cell holder designs were proposed to overcome some of these disadvantages (Creemer et al., 2008; Yaguchi et al., 2011). Advantages of the closed cell are a defined volume of gas and a much smaller gas path through which the electron beam must pass (around 4 μm). This enables high-resolution imaging up to pressures of 100,000 Pa. Furthermore, the formation of solid deposits in the TEM column can be avoided and toxic and pyrophoric chemicals can be used more straightforwardly than in ETEMs. The systems are compatible with most commercially used TEMs. Of course, there are also some disadvantages associated with gas cell holders: due to the thickness of the holder and the limited pole piece opening of the microscope, the measurement of energy-dispersive X-ray spectroscopy is nearly impossible. Furthermore, a window breakage under high pressure might influence the column pressure. Due to the single-tilt function of the holder, most of the actual work using gas cell holders is on nanoparticles or pores (Katz et al., 2012; Zhang et al., 2015), because the loading of the sample onto the holder is very easy with this method and it is not necessary to have a double-tilt holder to reach the zone axis of crystalline specimens. Another field of research using gas environmental cells is III/V semiconductor nanowires (Kallesøe et al., 2012; Hillerich et al., 2013). The impossibility of tilting gas cell holders on two axes poses severe challenges for *in situ* investigations of growth on single crystalline bulk substrates or in structured geometries. Hence, sample preparation and sample loading into the gas cell has to be optimized.

A process to prepare crystalline bulk samples by focused ion beam (FIB) and lift out of the FIB lamella in a controlled and reproducible way into the environmental holder (Protochips Inc., Raleigh, NC, USA, described in more detail in the Materials and Methods section) is shown in this study. The establishment of this routine enabled us to obtain high-resolution scanning TEM (STEM) images in zone-axis orientation in a gas cell holder having only single axis tilt capability. The samples investigated in this study are Ga(NAsP) laser structures grown on an Si (001) substrate.

Received September 8, 2015; accepted March 1, 2016
*Corresponding author. rainer.straubinger@physik.uni-marburg.de

Materials and Methods

The samples were prepared for STEM investigation using a JIB 4601F (JEOL GmbH, Freising, Bayern, Germany), which contains a scanning electron microscope (SEM) and an FIB. In combination with a manipulator needle (Kleindiek Nanotechnik GmbH, Reutlingen, Baden-Württemberg, Germany), it is possible to prepare a lift-out lamella of an area of interest in a specific crystal orientation (target preparation). A double C_s-corrected JEOL JEM-2200 FS operating at 200 kV was used for TEM observation. The images were acquired in STEM mode by using a high-angle annular dark-field detector. This provides an intuitive way to distinguish between the different regions in the structure of the sample. A Ga(NAsP) quantum well structure on an Si substrate was chosen for this study. The samples were grown by metalorganic vapor phase epitaxy. The GaP/Si templates serve as a pseudo substrate consisting of a GaP layer about 100 nm thick nucleated on an exactly oriented Si (001) substrate. A more detailed description of the defect-free nucleation of GaP on Si (001) and on the growth of the Ga(NAsP) laser structure is given in Liebich et al. (2011), Volz et al. (2011), and Gies et al. (2014). It is, of course, important to examine these single crystalline samples in a low-index zone axis for a detailed investigation of, for example, structural changes during annealing processes.

In Situ Setup

The *in situ* system used is designed and produced by Protochips Inc. The atmosphere system consists of a TEM single-tilt holder (Allard et al., 2012), a gas supply manifold, and a control unit. The system was modified for our investigations to insert potentially toxic and pyrophoric III/V semiconductor precursors by adding a gas storage locker. The whole system is monitored by gas sensors to ensure safety. Details of the modified setup will be presented elsewhere. The parts of the system relevant to the present study are discussed in more detail in the following section.

Figure 1a shows a sketch of the front part of the holder. The tip of the holder is composed of two silicon environmental chips (e-chips) (E) with SiN windows and a lid (A). In combination with two O-rings (C), the chips form the environmental cell which is sealed against the vacuum of the microscope up to a pressure of 100,000 Pa. With the help of a ceramic membrane that covers most of the surface of the thermal e-chip, one can control the temperature precisely up to 1,000°C. For TEM investigation, the sample is mounted on the thermal e-chip (Fig. 1b), which is based on an Si wafer (300 μm thick) (F) with an SiN window (30 nm thick) in the middle. There is a ceramic heating membrane with a thickness of around 120 nm (H) on top of this window. The membrane has nine holes, each with a diameter of 10 μm. The sample needs to be placed directly over one of these holes, as will be explained in detail later. Two gold spacers (5 μm thick) (G) on the sides of the chip determine the later cell volume and are used as contacts. The second chip also includes an SiN window, which locks the cell and closes the electrical contact

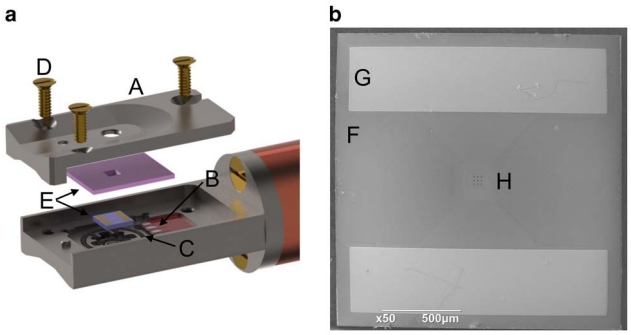

Figure 1. (**a**) Sketch of the atmosphere holder tip: (A) lid, (B) flexible circuit, (C) O-rings, (D) brass screws, (E) e-chip pair (Protochips Inc., Raleigh, NC, USA). **b:** SEM image of the thermal e-chip. (F) Si-based chip, (G) gold spacer 5 µm thick. (H) Electron transparent part of the chip comprised of the SiN window and the perforated ceramic membrane.

(B) between the thermal e-chip and the holder. The gas atmosphere and the temperature in the cell can be controlled precisely with the manifold and the control unit.

Results

Sample Preparation and Initial Imaging Test

A reproducible way to transfer a single crystalline FIB lamella in a specific zone axis onto the thermal e-chip is introduced in the following section. Any conventional FIB setup can be used for the first steps. In our case, the FIB working stage is modified as shown in Figure 2. First, the sample, in our case a cleaved piece of a GaP/Si (001) wafer, is mounted with conductive silver on the sample holder. Si exhibits distinct cleavage planes that can be used to determine the wafer orientation and, thus, to prepare the FIB lamella later in a certain crystal direction (e.g., parallel to a cleavage plane). The conventional size of FIB lamellae is around $25 \times 3\,\mu m^2$. Height of the lamellae ranges from 4 to 6 μm. The steps to achieve an optimum prepared conventional cross-section FIB lamella, including the deposition of a protection layer, the lift-out of the lamella, and the sample mounting on the TEM grid, is well described, for example, in the study by Schaffer et al. (2012). It is very critical for our intended application that the sample lays flat on the surface of the e-chip. However, due to redeposition and the broadening of the high-intensity Ga beam, the front and back planes of FIB lamellae are not usually parallel to each other. In order to ascertain that the later sample is in the zone axis and lays flat on the surface of the e-chip, it is necessary to modify the lamella in such a way that the front and back planes are parallel and that the planes are exactly perpendicular to the initial surface of the sample. This can be achieved by thinning the lamella with a gentle beam and a tilt of around 1° into the Ga beam to compensate for the broadening of the beam. It is essential that the entire sample is $<2\,\mu$m in thickness after the last step to make sure that the lamella fits between the two e-chips. Otherwise, it is possible that the lamella touches the window of the second

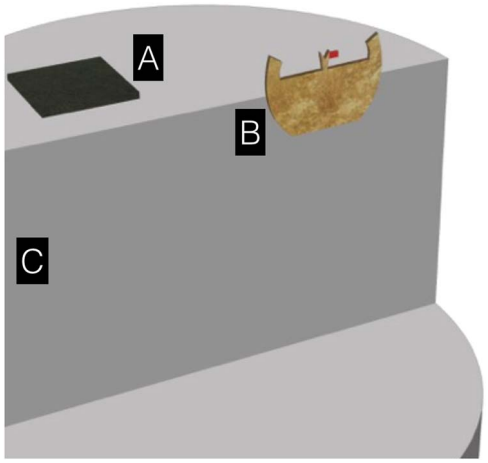

Figure 2. Sketch of the mounted cleaved piece of a GaP/Si (001) wafer (A) and TEM grid (B) on the FIB working stage (C). The lamella is highlighted in red. As shown, the TEM grid must be mounted perpendicular to the sample surface. The grid can be fixed by using a clamp or double-sided carbon duct tape. It is helpful to fix the sample to the FIB working stage using conductive silver to avoid charging.

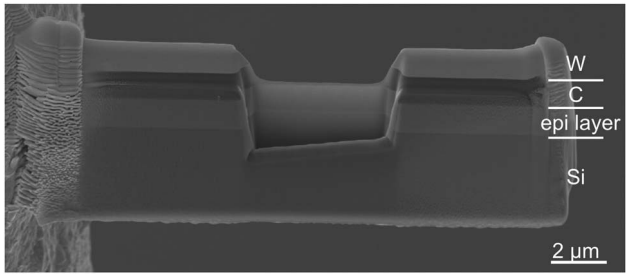

Figure 3. SEM image of the finished FIB lamella, which has a maximum thickness of 2 µm and two parallel side-faces. The electron transparent part is protected between thicker regions of the lamella. The structure of the lamella is marked on the right hand side. The epitaxial layer consists of a GaP/Ga(NAsP)/GaP multi quantum well structure.

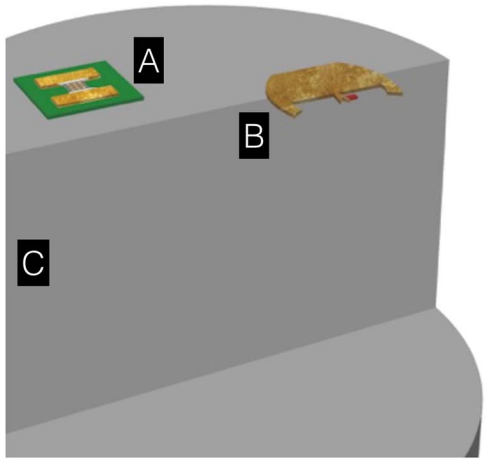

Figure 4. Sketch of the mounted e-chip (A) and TEM grid (B) with the lamella on the FIB working (C) stage. The side surface of the lamella is now in a parallel position to the e-chip.

e-chip during assembly of the cell. This would cause the window to break.

The easiest and most stable way to handle the finished lamella and to protect the electron transparent part is to prepare the lamella using a method similar to the H-bar method (Giannuzzi & Stevie, 1999). This preparation results in an electron transparent window in the middle of the lamella (compare Fig. 3). To reduce the Ga implantation and the damage produced by the Ga impact during preparation, it is advisable to reduce the Ga beam energy from 30 kV to 1 kV during the thinning process. Due to FIB preparation there will be some Ga implantation that might affect the later experiment. This is of course not an issue for the III/V semiconductor samples investigated in this study. An SEM image of the finished lamella as it can be used for STEM or TEM investigation in the *in situ* holder is shown in Figure 3. Further experiments have shown that it is also possible to place an FIB lamella with an electron transparent tip on the e-chip. The drawback of this preparation is that the electron transparent part is less stable compared with the H-bar lamella and, therefore, the transfer to the chip needs to be executed very carefully. Nevertheless, the lamella with the electron transparent tip shows better image quality during STEM observation compared with lamellae prepared using the H-bar technique. This is probably due to less redeposition during the thinning of the electron transparent part. The loading process is explained using the example of the H-bar lamella in the following section.

After finishing the lamella, the working stage of the FIB needs to be unloaded to bring the TEM grid with the mounted lamella into position for transferring the lamella to the e-chip. The easiest way to turn the side surface of the lamella into a parallel position to the e-chip is to mount the TEM grid on the FIB working stage, as shown in Figure 4. The TEM grid is fixed in the right position by using conductive silver. Furthermore, the conductive silver helps the avoidance of charging effects during the next steps. It should be noted here that specific FIB geometries and position of the manipulator needles need to be taken into account when mounting all pieces, otherwise, a part of the TEM grid might cover the lamella so that the manipulator needle cannot reach the positions required. The e-chip is mounted in the same position as the wafer was previously mounted by using two pieces of carbon duct tape. The window of the e-chip should not stick to the carbon duct tape to avoid rupturing the window.

After loading the second working stage, the manipulator needle is brought near the lamella, as shown in the SEM image in Figure 5a. Depending on the FIB system, this needs to be carried out under a certain angle between the FIB working stage and the manipulator needle. In our case (JIB 4601F), the positioning of the needle is best carried out at an angle of 53°. It is, of course, advisable not to record any image of the electron transparent part by using the Ga beam. The lamella is lifted with the needle from the TEM grid. Special care should be taken to cut the lamella in an area where its

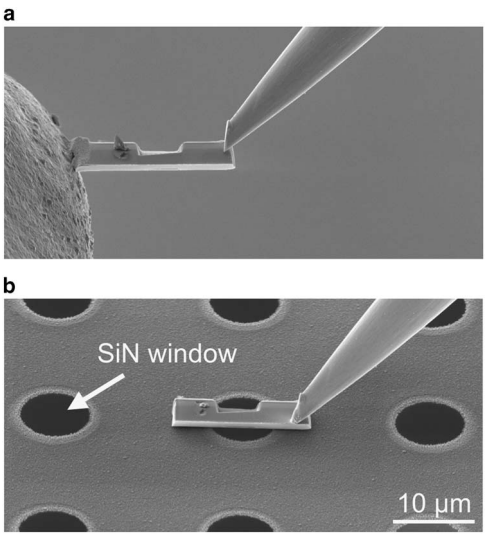

Figure 5. (**a**) SEM image of the rotated FIB lamella with positioned manipulator needle. **b:** SEM image of the FIB lamella in its final position above the SiN widows of the e-chip.

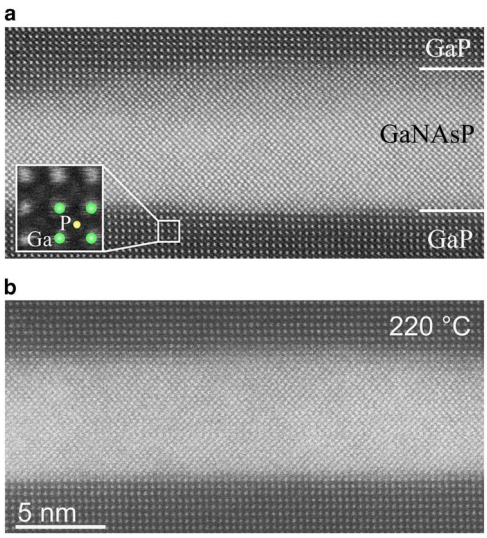

Figure 6. (**a**) STEM image of a FIB lamella before depositing the lamella in the environmental cell. An exemplary unit cell is shown enlarged as an inset. **b:** STEM image of the same lamella in the cell at 220°C and 1,000 Pa of N_2 environment.

front and back planes are parallel and without any residue of the tungsten deposition, otherwise, the lamella will not lay flat on the e-chip. After the lamella is free from the TEM grid, the lamella is moved to the right position on the e-chip. The SEM image (Fig. 5b) shows the lamella in its final position on the thermal e-chip. It is necessary to position the electron transparent part of the lamella precisely over the center SiN window of the e-chip. The transport of the lamella to the e-chip needs to be carried out under the same angle as the second lift-out, otherwise the lamella is not parallel to the surface of the ceramic membrane. The largest possible misalignment during the preparation is the tilt around the long axis of the lamella. To compensate for that misalignment, the lamella is deposited in such a way that the long axis is perpendicular to the gold spacer. By depositing tungsten on two to three positions on the edge of the lamella, one can fix it to the e-chip. Removing the manipulator needle is the last critical point. It is required to carefully etch away the connection between the needle and the lamella without destroying the e-chip by etching into the SiN window or redepositing a large amount of material onto the electron transparent part of the lamella.

It will be shown in the following section that the procedure described previously indeed facilitates obtainment of zone-axis orientations of cross-section samples of single crystalline specimens in a single-tilt holder. Figure 6a shows an STEM image of the Ga(NAsP) quantum well structure embedded in GaP at atomic resolution using a conventional double-tilt holder. This image was taken before the lamella was transferred into the e-chip. The different contrast between the Ga- and P-columns along the [100] zone axis is clearly visible (compare inset Fig. 6a). Furthermore, there is a strong difference in the intensity between the GaP region and the Ga(NAsP), which results from the high As content in the quaternary material. Figure 6b shows the same sample at a different region under the same magnification, but here the sample is mounted in the environmental cell and heated at 220°C in 1,000 Pa N_2 environment. The temperature was set to minimize carbon deposition during imaging. It is possible to achieve zone-axis orientation of the sample due to the very accurate FIB preparation. Furthermore, despite the N_2 environment and the two SiN windows which have a total thickness of around 50 nm, it is possible to observe atomic resolution for the FIB lamella mounted on the e-chip, as described previously. It can be seen by directly comparing both images in Figure 6b that the contrast becomes slightly worse and the P-columns are not visible. Deterioration of the STEM image (Fig. 6b) is possibly due to a slight mistilt of the lamella or the broadening of the electron beam due to the SiN windows. As mentioned before there might be a Ga-containing layer on the sample due to the Ga milling process in the FIB. The melting point for pure Ga is around 30°C (Adams et al., 1952). Thus, heating the sample to much higher temperatures than this leads to a melting of the implanted Ga and the formation of liquid Ga on the surface of the lamella (observed in our own heating experiments). This should be no problem for Ga-containing material, but it might be a problem for experiments with materials that interact with Ga such as Si (Werner et al., 2014). Nevertheless, this image proves that it is possible to investigate single crystalline structures at atomic resolution in the environment cell in a specific zone axis.

Summary and Outlook

This paper proves the possibility of transferring a single crystalline sample in a specific zone axis on the e-chip of an environmental cell holder by FIB lift-out. Due to the single-tilt function of this holder, it is necessary to prepare the lift-out lamella precisely along a specific zone axis if one is aiming for atomic resolution investigations. This can be

achieved by a very accurate FIB preparation. The preparation needs to be carried out precisely perpendicular to the zone axis and it is necessary to avoid any misalignment between the front and back plane of the lamella. This preparation facilitates the possibility of investigating atomic resolution STEM observations in an e-cell holder under high pressures and elevated temperatures. In the special case of the Ga(NAsP), the sample starts to evaporate at temperatures higher than 600°C. Metalorganic III/V semiconductor precursors, which are toxic and pyrophoric, will be supplied to the cell in future experiments. Hence, it is demonstrated that it will be possible to investigate growth kinetics and structure formation processes of materials in a specific crystallographic zone axis at atomic resolution *in situ*.

References

Adams, G.B. Jr., Johnston, H.L. & Kerr, E.C. (1952). The heat capacity of gallium up from 15 to 320 K. The heat of fusion at the melting point. *J Am Chem Soc* **74**, 4784.

Allard, L.F., Overbury, S.H., Bigelow, W.C., Katz, M.B., Nackashi, D.P. & Damiano, J. (2012). Novel MEMS-based gas-cell/heating specimen holder provides advanced imaging capabilities for in situ reaction studies. *Microsc Microanal* **18**, 656–666.

Birajdar, B.I., Antesberger, T., Butz, B., Stutzmann, M. & Spiecker, E. (2012). Direct in situ transmission electron microscopy observation of Al push up during early stages of the Al-induced layer exchange. *Scr Mater* **66**, 550–553.

Boyes, E.D. & Gai, P.L. (1997). Environmental high resolution electron microscopy and applications to chemical science. *Ultramicroscopy* **67**, 219–232.

Creemer, J.F., Helveg, S., Hoveling, G.H., Ullmann, S., Molenbroek, A.M., Sarro, P.M. & Zandbergen, H.W. (2008). Atomic-scale electron microscopy at ambient pressure. *Ultramicroscopy* **108**, 993–998.

Giannuzzi, L.A. & Stevie, F.A. (1999). A review of focused ion beam milling techniques for TEM specimen preparation. *Micron* **30**, 197–204.

Gies, S., Zimprich, M., Wegele, T., Kruska, C., Beyer, A., Stolz, W., Volz, K. & Heimbrodt, W. (2014). Annealing effects on the composition and disorder of Ga(N,As,P) quantum wells on silicon substrates for laser application. *J Cryst Growth* **402**, 169–174.

Hillerich, K., Dick, K.A., Wen, C.Y., Reuter, M.C., Kodambaka, S. & Ross, F.M. (2013). Strategies to control morphology in hybrid group III-V/group IV heterostructure nanowires. *Nano Lett* **13**, 903–908.

Hofer, F., Grogger, W., Kothleitner, G. & Warbichler, P. (1997). Quantitative analysis of EFTEM elemental distribution images. *Ultramicroscopy* **67**, 83–103.

Hugo, R.C., Kung, H., Weertman, J.R., Mitra, R., Knapp, J.A. & Follstaedt, D.M. (2003). In-situ TEM tensile testing of DC magnetron sputtered and pulsed laser deposited Ni thin films. *Acta Mater* **51**, 1937–1943.

Imrich, P.J., Kirchlechner, C., Kiener, D. & Dehm, G. (2015). Internal and external stresses: In situ TEM compression of Cu bicrystals containing a twin boundary. *Scr Mater* **100**, 94–97.

Kallesøe, C., Wen, C.Y., Booth, T.J., Hansen, O., Bøggild, P., Ross, F.M. & Mølhave, K. (2012). In situ TEM creation and electrical characterization of nanowire devices. *Nano Lett* **12**, 2965–2970.

Katz, M.B., Duan, Y., Graham, G.W., Pan, X. & Allard, L.F. (2012). In situ observation of the evolution of Pt particles in a perovskite-based catalyst during redox cycling at high temperature and atmospheric pressure with atomic resolution. *Microsc Microanal* **18**, 1120–1121.

Kishita, K., Sakai, H., Tanaka, H., Saka, H., Kuroda, K., Sakamoto, M., Watabe, A. & Kamino, T. (2009). Development of an analytical environmental TEM system and its application. *J Electron Microsc* **58**, 331–339.

Legros, M., Gianola, D.S. & Hemker, K.J. (2008). In situ TEM observations of fast grain-boundary motion in stressed nanocrystalline aluminum films. *Acta Mater* **56**, 3380–3393.

Liebich, S., Zimprich, M., Beyer, A., Lange, C., Franzbach, D.J., Chatterjee, S., Hossain, N., Sweeney, S.J., Volz, K., Kunert, B. & Stolz, W. (2011). Laser operation of Ga(NAsP) lattice-matched to (001) silicon substrate. *Appl Phys Lett* **99**, 071109.

Morrow, B.M., McCabe, R.J., Cerreta, E.K. & Tomé, C.N. (2014). *In-situ* TEM observation of twinning and detwinning during cyclic loading in Mg. *Metall Mater Trans A Phys Metall Mater Sci* **45**, 36–40.

Nielsen, M.H., Aloni, S. & De Yoreo, J.J. (2013). In situ TEM imaging of $CaCO_3$ nucleation reveals coexistence of direct and indirect pathways. *Science* **218**, 213–218.

Schaffer, B., Grogger, W. & Kothleitner, G. (2004). Automated spatial drift correction for EFTEM image series. *Ultramicroscopy* **102**, 27–36.

Schaffer, M., Schaffer, B. & Ramasse, Q. (2012). Sample preparation for atomic-resolution STEM at low voltages by FIB. *Ultramicroscopy* **114**, 62–71.

Suzuki, S., Bower, C. & Zhou, O. (1998). *In-situ* TEM and EELS studies of alkali–metal intercalation with single-walled carbon nanotubes. *Chem Phys Lett* **285**, 230–234.

Volz, K., Beyer, A., Witte, W., Ohlmann, J., Nmeth, I., Kunert, B. & Stolz, W. (2011). GaP-nucleation on exact Si (0 0 1) substrates for III/V device integration. *J Cryst Growth* **315**, 37–47.

Werner, K., Beyer, A., Oelerich, J.O., Baranovskii, S.D., Stolz, W. & Volz, K. (2014). Structural characteristics of gallium metal deposited on Si (001) by MOCVD. *J Cryst Growth* **405**, 102–109.

Yaguchi, T., Suzuki, M., Watabe, A., Nagakubo, Y., Ueda, K. & Kamino, T. (2011). Development of a high temperature-atmospheric pressure environmental cell for high-resolution TEM. *J Electron Microsc* **60**, 217–225.

Zhang, S., Chen, C., Cargnello, M., Fornasiero, P., Gorte, R.J., Graham, G.W. & Pan, X. (2015). Dynamic structural evolution of supported palladium–ceria core–shell catalysts revealed by in situ electron microscopy. *Nat Commun* **6**, 7778.

8.2 *In Situ* Thermal Annealing Transmission Electron Microscopy (TEM) Investigation of III/V Semiconductor Heterostructures Using a Setup for Safe Usage of Toxic and Pyrophoric Gases

Citation

R. Straubinger, A. Beyer, T. Ochs, W. Stolz, and K. Volz. In Situ Thermal Annealing Transmission Electron Microscopy (TEM) Investigation of III/V Semiconductor Heterostructures Using a Setup for Safe Usage of Toxic and Pyrophoric Gases. *Microscopy and Microanalysis*, 23(04):751–757, 2017[40]

Abstract

In this study we compare two thermal annealing series of III/V semiconductor heterostructures on Si, where during the first series nitrogen is present in the *in situ* holder. The second, comparative, measurement is done in a tertiarybutylphosphine (TBP) environment. The sample annealed in a TBP environment shows favorable thermal stability up to 500°C compared to the unstabilized sample, which begins to degrade at less than 300°C. Evaporation of P from the material is tracked qualitatively by measuring the thickness of the sample during thermal annealing with and without stabilization. Finally, we investigate the *in situ* thermal annealing processes at atomic resolution. Here it is possible to study phase separation as well as the diffusion of As from a Ga(NAsP) quantum well in the surrounding GaP material during thermal annealing. To make these investigations possible we developed an extension for our *in situ* transmission electron microscopy setup for the safe usage of toxic and pyrophoric III/V semiconductor precursors. A commercially available gas cell and gas supply system were expanded with a gas mixing system, an appropriate toxic gas monitoring system and a gas scrubbing system. These components allow *in situ* studies of semiconductor growth and annealing under the purity conditions required for these materials.

Contributions

All co-authors planned the modifications to the *in situ* setup and the structure of the home made gas storage locker. Thomas Ochs and I built the gas storage locker and installed all required safety equipment. I executed all experiments and together with Andreas Beyer we carried out the data analysis. Kerstin Volz and Wolfgang Stolz supervised the work and secured the funding to support this study. All authors reviewed the manuscript.

Microsc. Microanal. 23, 751–757, 2017
doi:10.1017/S1431927617012351

Microscopy AND Microanalysis

In Situ Thermal Annealing Transmission Electron Microscopy (TEM) Investigation of III/V Semiconductor Heterostructures Using a Setup for Safe Usage of Toxic and Pyrophoric Gases

Rainer Straubinger, Andreas Beyer,* Thomas Ochs, Wolfgang Stolz, and Kerstin Volz

Faculty of Physics and Materials Science Center, Philipps-Universitat Marburg Ringgold, Hans-Meerwein-Straße 6, Marburg, Hessen 35032, Germany

Abstract: In this study we compare two thermal annealing series of III/V semiconductor heterostructures on Si, where during the first series nitrogen is present in the *in situ* holder. The second, comparative, measurement is done in a tertiarybutylphosphine (TBP) environment. The sample annealed in a TBP environment shows favorable thermal stability up to 500°C compared to the unstabilized sample, which begins to degrade at less than 300°C. Evaporation of P from the material is tracked qualitatively by measuring the thickness of the sample during thermal annealing with and without stabilization. Finally, we investigate the *in situ* thermal annealing processes at atomic resolution. Here it is possible to study phase separation as well as the diffusion of As from a Ga(NAsP) quantum well in the surrounding GaP material during thermal annealing. To make these investigations possible we developed an extension for our *in situ* transmission electron microscopy setup for the safe usage of toxic and pyrophoric III/V semiconductor precursors. A commercially available gas cell and gas supply system were expanded with a gas mixing system, an appropriate toxic gas monitoring system and a gas scrubbing system. These components allow *in situ* studies of semiconductor growth and annealing under the purity conditions required for these materials.

Key words: *in situ*, TEM, STEM, III/V semiconductor, stabilized thermal annealing

Introduction

In situ (scanning) transmission electron microscopy [(S)TEM] has proven to be a suitable method to investigate dynamic processes in material structures. The compatibility of modern micro-electromechanical-based *in situ* TEM holders with most modern TEMs makes this technique feasible for a wide range of research. New holder designs, such as the closed cell holder from Protochips Inc., (Morrisville, NC, USA) have been developed. These allow investigations in different atmospheres at pressures of up to 1,000 hPa and temperatures of up to 1,000°C. A detailed characterization of these holders is shown in Allard et al. (2012). The aforementioned pressure and temperature ranges match the growth and postgrowth annealing conditions during metal organic vapor phase epitaxy (MOVPE) and, consequently, the usage of *in situ* TEM holders enables the possibility of studying MOVPE processes under high resolution condition.

The positive influence of postgrowth annealing on the performance of devices, such as III/V dilute nitride Ga(NAsP) heterostructures on (001) Si-substrates, is well known and has been investigated by various *ex situ* techniques (Buyanova et al., 2000; Kunert et al., 2006; Gies et al., 2014). Nevertheless, III/V semiconductor growth and the study of annealing processes under high resolution conditions have not been widely studied *in situ* in TEM (Wen et al., 2011; Diaz et al., 2012). This is possibly due to the complications involved in handling the necessary precursor gases. To overcome this issue when handling toxic and pyrophoric group III and group V precursors—such as tertiarybutylphosphine (TBP), trimethylgallium (TMGa), or hydride based precursors—and insert these in large amounts into the TEM, it is necessary to modify the *in situ* system accordingly. After modifying the system, it is possible to study the growth kinetics and thermal annealing processes of III/V semiconductors. In order to do this, an in-depth understanding of growth mechanisms and postgrowth annealing processes of III/V semiconductor are key factors in successfully developing new material systems.

In this paper a detailed description of the required modifications to inject the necessary types of gases into the atmosphere of the system (Protochips Inc., Morrisville, NC, USA) is presented. Subsequently, the functionality of the system is verified to show that it is possible to study the group V stabilized annealing processes of Ga(NAsP) structures, as well as the surrounding GaP material on Si substrate, *in situ* in the TEM. During one annealing series N_2 is present in the *in situ* holder. The comparative measurement is done in a TBP environment. In this P-rich environment the P in the crystal structure is prevented from evaporation. Afterwards, the evaporation of P is quantified using the remaining TEM

Received November 17, 2016; accepted June 19, 2017
*Corresponding author. andreas.beyer@physik.uni-marburg.de

sample thickness as a measure. Finally, we investigate the structural changes in the sample at atomic resolution conditions as a function of the annealing temperature.

Experimental Methods

In this study a closed *in situ* TEM holder is used, which consists of an e-chip paired with 20-nm thick electron-transparent SiN windows placed between two O-rings and a lid (Protochips Inc). The thermal e-chip is coated with a SiC membrane, and varying the applied voltage across this membrane allows for precise control over the temperature of the chip. After assembly, the holder tip forms a closed cell which is sealed against the vacuum of the TEM. This closed cell holder design allows for observations at atmospheric pressures of up to 1,000 hPa and temperatures reaching up to 1,000°C, with a heating rate of 5°C/s. A more detailed characterization of the holder is provided in Allard et al. (2012). In order to inject toxic and pyrophoric III/V semiconductor precursors like TBP or TMGa into the TEM, some major changes to the system are necessary. Figure 1a shows a sketch of the modified system line plan. On the left hand side one can see the line plan of the manifold and below that one can see the holder. These were both produced by Protochips Inc. Next to the holder tip one can see an enlarged side view of the two e-chips, with a sample mounted on the thermal e-chip. To achieve the best resolution the sample is mounted in the STEM configuration. In this setup the sample is mounted on the top SiN window in the direction of the beam. For a better understanding of the geometry of this setup, the electron beam direction is marked with an arrow in Figure 1a. The manifold consists of two tanks, as shown in Figure 1a, where tanks 1 and 2 are used for the experimental gas and vacuum tank, respectively. Due to a lower pressure level in the vacuum tank, the experimental gas is sucked in from the experimental gas tank through the holder tip and into the vacuum tank. Thus, it is possible to precisely adjust the gas flow rate. Furthermore, it is possible to modify the constant pressure level in the holder tip. On the right hand side in Figure 1a, a schematic of our custom-built gas storage locker can be seen. In order to get a better understanding of the structure, a photo of the aforementioned gas storage locker is shown in Figure 1b. To take fire safety into account the locker complies with DIN 12925. This means that it is both fire safe and that all openings close automatically in case of a fire inside the locker. Furthermore, this functionality is reviewed annually. The line system consists of electro-polished stainless steel pipes with a diameter of 1/4 inch for the main pipes and 1/8 inch for both the precursor container connectors and the connection lines to the manifold. As far as possible, all connections between pipes were welded. Vacuum coupling radiation (VCR) metal gasket face seals (Swagelok, Cleveland, OH, USA) with silver-plated stainless steel seals were used to connect the pipes where necessary. Before the first test run the seal integrity of the system and every weld was tested using a helium leak checker. A mini absorber (CS Cleaning Systems AG, Ismaning 85737, Germany; Fig. 1b labeled as A) ensures that no toxic gases are released into the environment. Furthermore, the locker consists of three ports on the group III line (Fig. 1b labeled as B) and three ports on the group V line (Fig. 1b labeled as C). The precursors are stored in stainless steel containers (Fig. 1b labeled as F). To ensure safety and to stay below the German MAK level, the maximum level of gas allowed in the air per cubic meter, the containers are only filled with a gas phase up to a pressure compatible with the MAK values for the room size used. The precursor gases

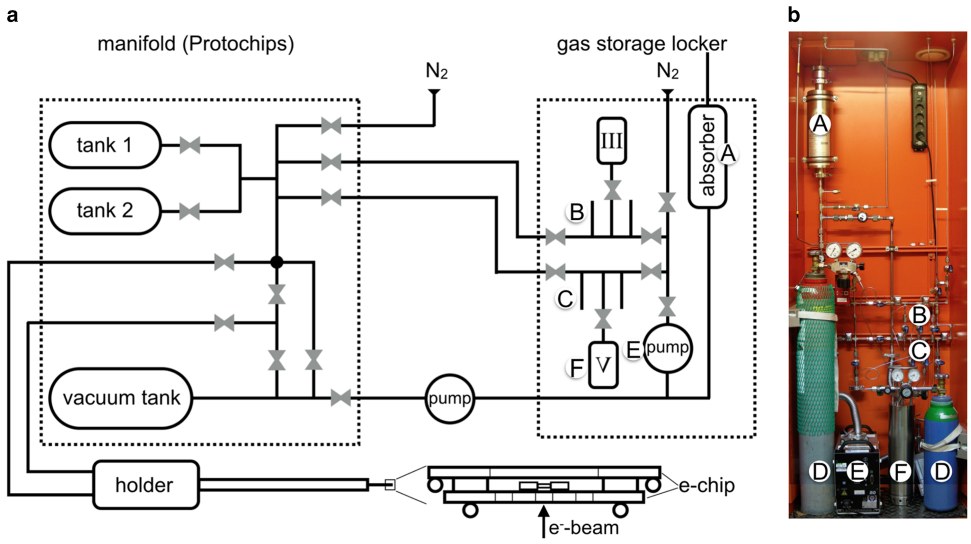

Figure 1. A sketch of the modified system line plan is shown in (**a**). On the left hand side one can see the line plan of the manifold and below the holder, which are designed and produced by Protochips Inc. Next to the holder tip one can see an enlarged side view of the two e-chips with mounted sample on the thermal e-chip. On the right hand side one can see our custom-built gas storage locker. **b:** Photo of the custom-built gas storage locker with connected gas bottles and precursor containers.

are transfilled up to the desired level into the stainless steel containers in an MOVPE machine. The pump (Fig. 1 labeled as E) in the gas storage locker is used to evacuate all gas lines of the custom-built system. In addition, an external ventilation system ensures that no toxic gases distribute in the air. The manifold and locker form a closed system in which high-purity N_2 is used as carrier and purge gas. If necessary, it is possible to switch the carrier gas to pure argon (Fig. 1b labeled as D) or an Ar/H_2 (Fig. 1b labeled as D) mixture (4% H_2). The overall system is monitored by gas sensors (Dräger, Lübeck, Germany) to ensure safety. On conclusion of the experiment, the whole system is cleaned by alternating between 1 and 600 hPa of high-purity N_2 gas for several pump/purge cycles.

The test samples for this study were grown by MOVPE. GaP/Si (001) templates serve as pseudo substrates for a III/V laser structure. These consist of a GaP layer ~100 nm thick, nucleated on an exact Si (001) substrate. Ga(NAsP)/GaP/(BGa)P heterostructures were grown on these templates to achieve a laser integrated on Si. A more detailed description of the defect-free nucleation of GaP on Si (001) and the growth of the Ga(NAsP)/GaP/(BGa)P/Si laser structure is given in Liebich et al. (2011) and Volz et al. (2011). A detailed characterization of the quality of the quantum well structure is given in Wegele et al. (2016*b*). The key reason why these samples were chosen is the behavior of the quantum well structure during thermal annealing. Changes in the composition and homogeneity take place during this process, which it may be possible to investigate *in situ* in the TEM. A detailed description of these structural changes and their correlation with the optoelectronic properties of the quantum well during rapid thermal annealing (RTA) is given in Gies et al. (2014) and Wegele et al. (2016*a*). The samples were prepared for the *in situ* annealing STEM investigation using a focused ion beam (FIB; JIB 4601 F; JEOL, Freising, Germany) system. A detailed description of the preparation and loading process of the specimens is given in Straubinger et al. (2016). In summary, an electron transparent lamella was prepared out of a wafer piece as described in Schaffer et al. (2012). Afterwards, the lamella was turned by 90° along its longer axis and mounted with the electron transparent region precisely above the electron transparent SiN window of the thermal e-chip (Protochips Inc, Morrisville, NC, USA). A double C_s-corrected JEOL JEM-2200 FS operating at 200 kV in combination with the gas cell holder was used for the TEM observations. The images were recorded in high angle annular dark field (HAADF) mode. The acquired images were normalized with respect to the impinging beam following the procedure described in He & Li (2014). The contribution of the SiN windows to the HAADF intensity was subtracted from the measured intensity of the crystalline samples. Using the frozen phonon approximation available in STEMsim (Rosenauer & Schowalter, 2007), complementary contrast simulations were carried out. A super cell consisting of 7×7 unit cells of GaP projected along the [010] direction was used to calculate 15 phonon configurations. The influence of applied temperature on HAADF intensity was modeled by adjusting the Debye–Waller factors to the experimental temperatures, as shown in Schowalter et al. (2008). By comparing the simulated HAADF intensities to the experimental intensities, the thickness of the TEM sample can be determined as successfully shown in Beyer et al. (2016).

Results

This paper is organized as follows: first, quantitative thermal annealing experiments both with and without P stabilization are compared to prove the functionality of the system used. Next, evaporation of P from the samples is compared by measuring the quantitative thickness from the HAADF intensity at different temperatures. Finally, we investigate *in situ* thermal annealing processes at atomic resolution conditions. From this, it is possible to measure the inhomogeneity of the quantum wells with increasing temperature by analyzing the standard deviation of the group V column intensities at each temperature step. Furthermore, we study the diffusion of As constituents from the quantum well in the surrounding GaP material during thermal annealing.

As mentioned in the introduction, postgrowth annealing is an effective way to improve layer quality by reducing crystal defects, which leads to improvement of the performance of devices such as lasers. The following experiment should verify whether it is possible to study thermal annealing processes for III/V semiconductors in any desired atmosphere in the TEM. In doing so, the functionality of the setup will also be proven. Figure 2 shows the quantum well structure as introduced in the experimental methods chapter. The STEM images (Figs. 2a to 2c) show the structure during the unstabilized thermal annealing experiments in a 10 hPa N_2 environment. Figure 2a shows the intact quantum well structure at 400°C, with the single layers in the sample annotated on the left hand side. By comparing Figures 2a and 2b one can already see a significant degradation of the structure at 600°C. This degradation is caused by evaporation of P. By taking a closer look at the STEM image (Fig. 2b) one can see small droplets that remain on the surface. An example of one of these droplets is marked with a white arrow. During the following experiments, the droplets move across the surface and begin to cluster on the upper surface of the lamella (compare inset Fig. 2b). *Ex situ* energy dispersive X-ray spectroscopy measurements show that the droplets composed of Ga. This confirms the assumption that the destruction of the layer is caused by evaporation of P while Ga remains on the surface. Figure 2c shows the same area of the sample at 700°C, in which the quantum well structure has been completely destroyed. Figures 2d to 2f show a different lamella of the same material. However, the annealing experiment was carried out in 140 hPa TBP without additional carrier gases in the system. In this P-rich environment the P in the structure is prevented from evaporating. By comparing Figures. 2d and 2e one can even see a slight improvement of the image quality in terms of the

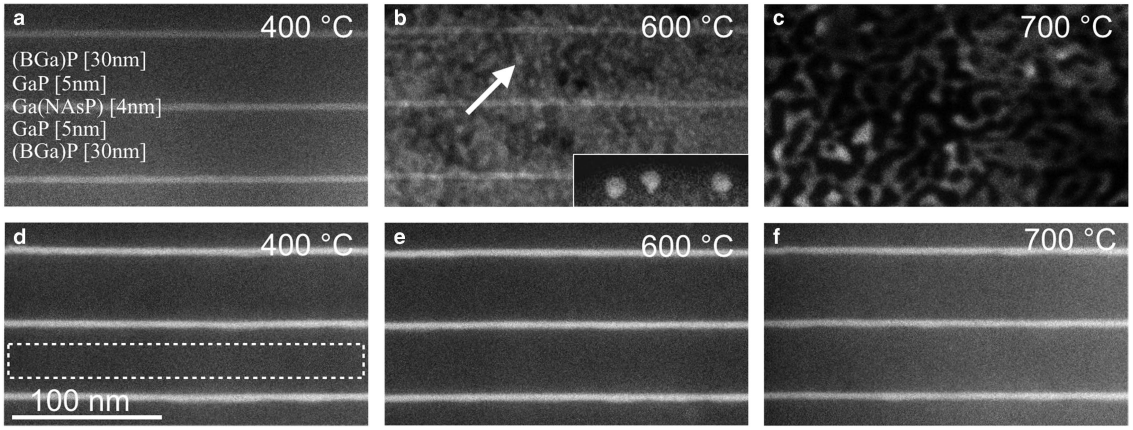

Figure 2. a-c: STEM images of the quantum well structure during the unstabilized thermal annealing process in a 10 hPa N_2 environment. In (**a**), annotated single layers can be seen. To the bottom right of (**b**) a sub image of Ga droplets on the upper surface of the TEM lamella can be seen. **d–f:** The annealing process in a 140 hPa TBP environment.

homogeneity of the contrast distribution. This effect may be caused by evaporation of the amorphous layer, which originates from the preparation of the lamella and polishing the surfaces in the FIB, or it may be caused by the thinning of the sample. This positive effect was also observed in further annealing experiments. Figure 2f shows the structure at 700°C. By comparing Figures 2d, 2e, and 2f, one is not able to see any noticeable destruction of the structure. By comparing Figures 2c and 2f), one can clearly see the difference between the stabilized and unstabilized annealing processes. Thickness measurements verify that the sample annealed in 140 hPa TBP remains undamaged until 500°C and starts to degrade slowly by 600°C. It is worth noting that all images in Figure 2 are shown in their individual intensity scales to visualize their respective morphologies and that the absolute intensity scales of the images change during the thermal treatment; this is because the thickness of the TEM sample changes due to evaporation of P.

In the following, evaporation of P from the (BGa)P barrier will be quantified by measuring the remaining thickness of the TEM sample. In Figure 3a, the simulated HAADF intensities of GaP are plotted against the TEM sample thickness for a selection of different temperatures used in these experiments. As can be seen in this figure, the influence of temperature on average HAADF intensity is rather small, i.e. at maximum effect, 0.67% of the impinging beam intensity at a sample thickness of 200 nm. Nevertheless, we used the corresponding simulation when comparing the experimental intensities derived from the (BGa)P region, which is marked with a dashed box in Figure 2d, to the simulated intensities in order to determine the actual sample thickness. The influence of the small amount of B (≈3%) in the GaP is negligible in the analysis. The plot in Figure 3b shows the derived thicknesses divided by $t_{200°C}$ (the thickness of each sample at 200°C). The black data points indicate the thickness change of the sample annealed in a 10 hPa N_2 environment. The red data points indicate the thickness change of the sample annealed in a 140 hPa TBP environment. By comparing both processes one can see a significant difference in evaporation of P from the samples. As indicated in Figures 2a to 2c, the sample immediately starts to degrade when increasing temperature without stabilization (black data points, Fig. 3b). In contrast to this, the red data points show the much more stable behavior of the same sample structure annealed in a 140 hPa TBP environment, which appears to show no significant degradation until 500°C. In the temperature range of around 600°C the sample starts to degrade. To get a better insight into the evaporation process, Figure 3c shows an Arrhenius plot of the thickness divided by $t_{200°C}$ of the (BGa)P barrier as a function of the annealing temperature. The resulting activation energies are $|E_A| = 0.11$ eV for the sample annealed in a 10 mbar N_2 environment and $|E_A| = 0.28$ eV for the sample annealed at 140 mbar TBP. These numbers are significantly smaller than what was found for GaP bulk material. In the work of Kobayashi & Kobayashi (1991), the activation energy of evaporation GaP bulk material was calculated as 1.18 eV. In the case of a thin TEM lamella one needs, however, to take into account that the large surface to volume ratio plays a crucial role in the evaporation process. As such, the exact numbers are not comparable. However, the increase in the activation energy resulting from the P stabilized measurement further supports the statement that group V stabilization is important for thermal annealing experiments involving III/V semiconductors. Moreover, these values will serve as qualitative references for future growth and annealing studies.

The STEM images in Figure 4 show the annealing behavior of the Ga(NAsP) quantum well and surrounding GaP in a temperature range from 250 to 450°C at atomic resolution under unstabilized conditions. Due to beam introduced carbon deposition in the sub −200°C temperature regime, the starting temperature of this series was chosen to be 250°C. Each image is separated, with the STEM image on the left hand side and the color-coded group V column intensity map on the right hand side. The scale of color-coding is shown on the far right hand with respect to the intensity of the GaP barrier. The single layers are annotated

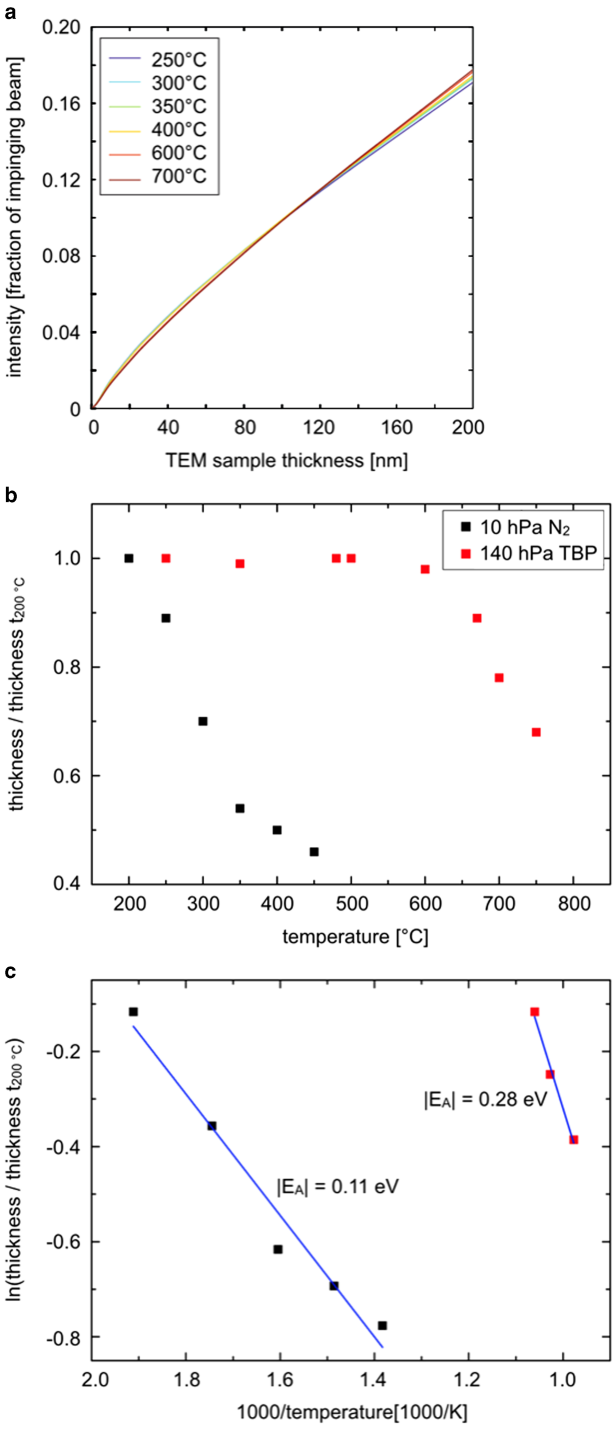

Figure 3. The simulated HAADF intensities of GaP are drawn against the TEM sample thickness for different temperatures in (**a**). The plot (**b**) shows the thickness divided by t_{200} °C in the temperature range investigated. The black data points indicate the thickness change of the sample during the unstabilized annealing. The red data points indicate the thickness change of the sample during the stabilized annealing in 140 hPa TBP environment. The Arrhenius plot (**c**) shows the thickness divided by t_{200} °C of the (BGa)P barrier as a function of the annealing temperature. The colour-coding is the same as in plot (**b**).

on the far left hand side. Figure 4a shows the sample structure at 250°C. At this temperature, the contrast within the Ga(NAsP) quantum well is still homogenously distributed. This can be further confirmed by the color-coded group V intensity map. In addition, the color-coded group V intensity map shows a distinct interface between the quantum well and the lower GaP material. It should be noted that the sample has already begun to degrade at this temperature (compared with the black data points in Fig. 3b). By comparing the quantum well regions in Figures 4a and 4b one can already see a slight blurring of the contrast, and thus a spreading of the group V column intensities. This process sets in at the evaporation temperature of P shown in the previous experiment (compared with Fig. 3, black data points). The aforementioned intensity change within the quantum well can be caused by either phase separation or composition changes due to the different evaporation temperatures of the group V constituents in the quantum well. As the ratio between the average group V column intensities within the center part of the quantum well and the average group V column intensities in the GaP barrier stays constant, i.e. the averaged quantum well composition does not change, temperature induced phase separation is the more likely cause for the observation. In future, studies using different group V stabilization conditions will give a detailed insight into this process. Due to thermal drift, the images recorded at higher temperatures have a slight streaky contrast. With increasing temperature, one can see the proceeding phase separation of group V constituents within the quantum well (compare color-coded intensity distribution of the group V columns within the quantum well in Fig. 4c). By comparing the color-coded group V intensity map in Figure 4c with the maps at lower temperatures it is possible to see that the group V constituents also diffuse into the surrounding GaP layer. This diffusion process with increasing temperature is also supported by the color-coded group V intensity map shown in Figure 4d. The same process can also be seen by comparing the STEM intensity distribution at the lower interfaces of the quantum well with increasing temperatures. Intensity measurements, as shown later on, provide quantitative support for this behavior. By increasing the temperature further, the sample was completely destroyed within seconds.

The phase separation with increasing temperature, as mentioned above, can also be determined by measuring each group V column's mean intensity and associated standard deviation (σ_i). Figure 5a shows the σ_i divided by the mean intensity in the quantum well region as function of the annealing temperature. It should be noted here that normalizing the standard deviation to the intensity is necessary as the STEM HAADF detectors have noise, which is proportional to the signal. An increase in phase separation within the quantum well with increasing temperature is clearly visible. Figure 5b shows the intensity of the group V columns along the lower Ga(NAsP)/GaP interface normalized to their mean intensity in the Ga(NAsP) region. The region plotted in Figure 5b is marked with a white arrow in the STEM image in Figure 4c. The images used in this

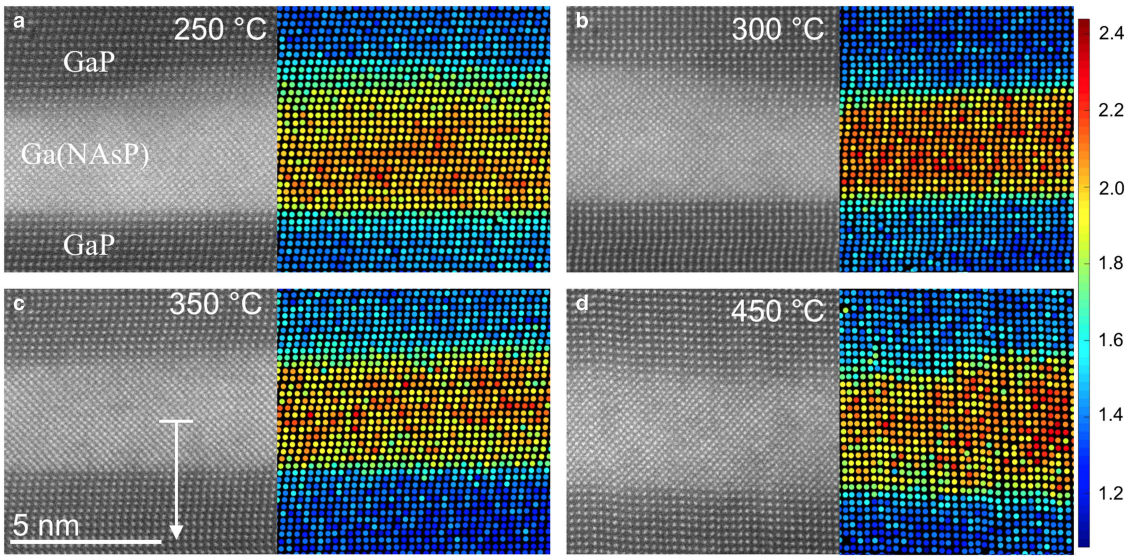

Figure 4. Thermal treatment of the Ga(NAsP) quantum well at atomic resolution conditions in a 10 hPa N2 environment. The single layers are annotated in (**a**). Each image is separated in the STEM image (**a,c**) and the colour-coded group V column intensity map (**b,d**). The scale of colour-coding is shown on the far right side with respect to the intensity of the GaP barrier. The white arrow in (**c**) marks the line scan region for further investigation, which is introduced later in the text.

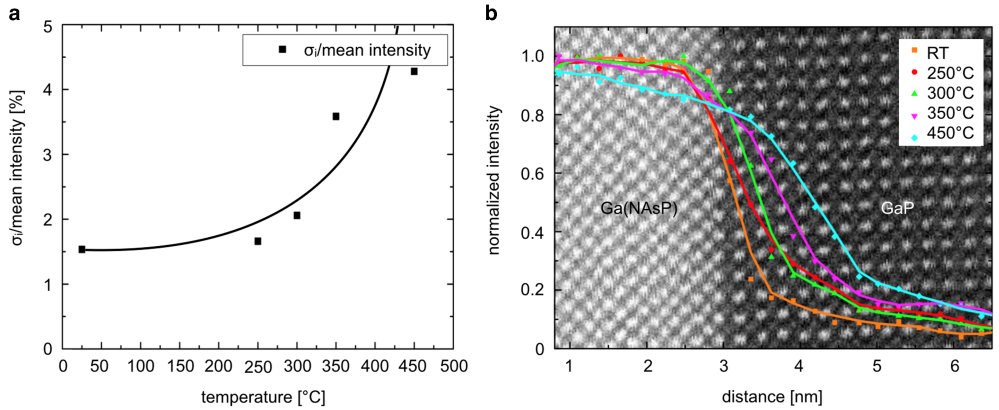

Figure 5. Plot (**a**) shows the standard deviation of the intensity divided by the mean intensity of the group V columns within the quantum well in the temperature range investigated. Plot (**b**) shows the normalized intensity of the group V columns along the Ga(NAsP)/GaP interface. The STEM image in the background shows an Ga(NAsP)/GaP interface at room temperature. Furthermore, the plotted region is marked in the STEM image Figure 4c with a white arrow.

analysis were adjusted to make sure that the lower interface between the quantum well and the surrounding GaP material were properly aligned. The orange data points represent the group V column intensities at room temperature. This measurement was done in the double tilt holder before the sample was placed on the thermal e-chip. The STEM image shown in the background of the plot is also recorded in the double tilt holder at room temperature. By taking a closer look at the orange data points it is possible to observe a nearly abrupt interface between the quantum well and the surrounding GaP material after growth. This can be seen by the group V intensity dropping within two group V layers by a factor of 5. Compared to that the red (250°C), green (300°C), magenta (350°C), and cyan (450°C) data points represent the group V intensities at increasing annealing temperatures. This series shows a significant increase in the group V column intensity within the GaP close to the Ga(NAsP)/GaP interface. This increase in intensity indicates that As (atomic number 33) diffuses from the quantum well into the surrounding material and replaces P (atomic number 15) in the group V columns during the annealing process. As mentioned before, the blurring of the Ga(NAsP)/GaP interface is also visible in the STEM images in Figures 4a to 4c. By comparing the highest temperature measurement (450°C) with the room temperature measurement, it can been seen that the group V intensities drop within 8 group V layers to the same level that the room temperature measurement reaches within two group V layers. When

comparing these results to the aforementioned thermal annealing experiments shown in Gies et al. (2014) and Wegele et al. (2016*b*), one should keep in mind the difference in annealing procedures. Compared to the *in situ* annealing system, which allows for a heating rate of 5°C/s, the RTA reactor enables a much faster heating rate of 50°C/s, resulting in very short annealing times on the order of 10 s. Furthermore, the sample annealed in the RTA is bulk material compared with a very thin TEM lamella annealed in the *in situ* system. Both techniques can result in significantly different diffusion behavior between the two experimental setups. Nevertheless, both experimental approaches support the prediction of group V constituents from the Ga(NAsP) quantum well diffusing into the surrounding material.

In summary, this study demonstrates that it is possible to investigate thermal annealing processes like material phase separation and diffusion *in situ* in the TEM at atomic resolution conditions under the safe supply of toxic and pyrophoric gases.

Summary

This paper shows that it is possible to handle toxic and pyrophoric III/V semiconductor precursors for both growth and group V stabilized thermal annealing processes in the TEM. The suggested modifications to the *in situ* system needed to achieve this goal were described. Two annealing series of a Ga(NAsP) quantum well structure and the surrounding GaP/(BGa)P material were observed to verify the functionality of the system. One thermal treatment was done in an environment of 10 hPa N_2. The second, comparative, measurement was done in an environment of 140 hPa TBP. In this P-rich environment the P in the crystal is prevented from evaporation. The sample annealed in a TBP environment showed thermal stability up to 500°C compared with the sample without stabilization, which began to degrade at less than 300°C. For quantitative comparisons, the sample thicknesses of both TEM lamellae were compared over the annealing temperature range. The results of the thickness measurements support the success of the stabilized annealing experiment. Finally, we investigated *in situ* thermal annealing processes at atomic resolution conditions. In this series the phase separation of group V constituents can be directly observed, which results in a blurring of the contrast and thus a spreading of the group V column intensities. By plotting the standard deviation (σ_i) divided by the mean intensity over the temperature range investigated it is possible to determine the increase in inhomogeneity with increasing temperature. Finally, it is possible to study the diffusion of As from the quantum well into the surrounding GaP material during thermal annealing by measuring the group V column intensities along the Ga(NAsP)/GaP interface.

References

Allard, L.F., Overbury, S.H., Bigelow, W.C., Katz, M.B., Nackashi, D.P. & Damiano, J. (2012). Novel MEMS-based gas-cell/heating specimen holder provides advanced imaging capabilities for in situ reaction studies. *Microsc Microanal* **18**, 656–666.

Beyer, A., Belz, J., Knaub, N., Jandieri, K. & Volz, K. (2016). Influence of spatial and temporal coherences on atomic resolution high angle annular dark field imaging. *Ultramicroscopy* **169**, 1–10.

Buyanova, I.A, Pozina, G., Hai, P.N., Thinh, N.Q., Bergman, J.P., Chen, W.M., Xin, H.P. & Tu, C.W. (2000). Mechanism for rapid thermal annealing improvements in undoped GaN_xAs_{1-x} / GaAs structures grown by molecular beam epitaxy. *Appl Phys Lett* **77**, 2325.

Diaz, R.E., Sharma, R., Jarvis, K., Zhang, Q. & Mahajan, S. (2012). Direct observation of nucleation and early stages of growth of GaN nanowires. *J Cryst Growth* **341**, 1–6.

Gies, S., Zimprich, M., Wegele, T., Kruska, C., Beyer, A., Stolz, W., Volz, K. & Heimbrodt, W. (2014). Annealing effects on the composition and disorder of Ga(N,As,P) quantum wells on silicon substrates for laser application. *J Cryst Growth* **402**, 169–174.

He, D.S. & Li, Z.Y. (2014). A practical approach to quantify the ADF detector in STEM. *J Phys Conf Ser* **522**, 12017.

Kobayashi, N. & Kobayashi, Y. (1991). As and P deposition from III-V semiconductor surface in metalorganic chemical vapor deposition studied by suface photo-absorption. *Jpn J Appl Phys* **30**, 1699–1701.

Kunert, B., Reinhard, S., Koch, J., Lampalzer, M., Volz, K. & Stolz, W. (2006). First demonstration of electrical injection lasing in the novel dilute nitride Ga (NAsP)/GaP-material system. *Physica Status Solidi (c)* **3**, 614–618.

Liebich, S., Zimprich, M., Beyer, A., Lange, C., Franzbach, D.J., Chatterjee, S., Hossain, N., Sweeney, S.J., Volz, K., Kunert, B. & Stolz, W. (2011). Laser operation of Ga(NAsP) lattice matched to (001) silicon substrate. *Appl Phys Lett* **99**, 71109.

Protochips (2016). Protochips http://www.protochips.com/.

Rosenauer, A. & Schowalter, M. (2007). STEMSIM—A new software tool for simulation of STEM HAADF Z-contrast imaging. In *Microscopy of Semiconducting Materials (Proceedings in Physics)*, Cullis, A.G. & Midgley, P.A. (Eds.), pp. 169–172. Dordrecht, The Netherlands: Springer.

Schaffer, M., Schaffer, B. & Ramasse, Q. (2012). Sample preparation for atomic-resolution STEM at low voltages by FIB. *Ultramicroscopy* **114**, 62–71.

Schowalter, M., Rosenauer, A., Titantah, J.T. & Lamoen, D. (2008). Computation and parametrization of the temperature dependence of Debye-Waller factors for group IV, III-V and II-VI semiconductors. *Acta Crystallogr A Found Crystallogr* **65**, 5–17.

Straubinger, R., Beyer, A. & Volz, K. (2016). Preparation and loading process of single crystalline samples into a gas environmental cell holder for in situ atomic resolution scanning transmission electron microscopic observation. *Microsc Microanal* **22**, 515–519.

Volz, K., Beyer, A., Witte, W., Ohlmann, J., Nmeth, I., Kunert, B. & Stolz, W. (2011). GaP-nucleation on exact Si (0 0 1) substrates for III/V device integration. *J Cryst Growth* **315**, 37–47.

Wegele, T., Beyer, A., Gies, S., Zimprich, M., Heimbrodt, W., Stolz, W. & Volz, K. (2016a). Correlation of the nanostructure with optoelectronic properties during rapid thermal annealing of Ga (NAsP) quantum wells grown on Si(001) substrates. *J Appl Phys* **119**, 025705.

Wegele, T., Beyer, A., Ludewig, P., Rosenow, P., Duschek, L., Jandieri, K., Tonner, R., Stolz, W. & Volz, K. (2016b). Interface morphology and composition of Ga(NAsP) quantum well structures for monolithically integrated LASERs on silicon substrates. *J Phys D Appl Phys* **49**, 75108.

Wen, C.Y., Tersoff, J., Hillerich, K., Reuter, M.C., Park, J.H., Kodambaka, S., Stach, E.A. & Ross, F.M. (2011). Periodically changing morphology of the growth interface in Si, Ge, and GaP nanowires. *Phys Rev Lett* **107**, 1–4.

8.3 Thermally Introduced Bismuth Clustering in Ga(P,Bi) Layers under Group V Stabilised Conditions Investigated by Atomic Resolution *In Situ* (S)TEM.

Citation

R. Straubinger, M. Widemann, J. Belz, L. Nattermann, A. Beyer and K. Volz. Thermally Introduced Bismuth Clustering in Ga(P,Bi) Layers under Group V Stabilised Conditions Investigated by Atomic Resolution *In Situ*. Submitted (S)TEM. Submitted to *Scientific Reports* (2018)

Abstract

We report the formation of Bi clusters in Ga(P_{1-x},Bi_x) layers during an *in situ* (scanning) transmission electron microscopy ((S)TEM) annealing investigation. The non-destructive temperature regime in dependence on the tertiarybutylphosphine (TBP) pressure in the *in situ* cell was investigated to ensure that the results are not distorted by any destructive behaviour of the crystal during the thermal treatment. The following annealing series of the Ga($P_{92.6}Bi_{7.4}$) and Ga($P_{96.4}Bi_{3.6}$) layers reveals that the threshold temperature at which the Bi clustering takes place is 600°C in the Ga($P_{92.6}Bi_{7.4}$) layer. Further thermal treatments up to 750°C show a relationship between the Bi fraction in the Ga(P_{1-x},Bi_x) layer and the initial temperature at which the Bi clustering takes place. Finally, we investigate one Bi cluster at atomic resolution conditions. In these conditions, we found that the Bi cluster crystallized in a rhombohedral phase, aligning with its {101} planes parallel to the Ga(P,Bi) {202} planes.

Contributions

The MOVPE growth of the sample was executed by Lukas Nattermann. The preparation of the TEM specimens for this study as well as the acquisition of the STEM micrographs was performed by me and Max Widemann. The data analysis was carried out by myself Jürgen Belz and Andreas Beyer. Kerstin Volz supervised the work and secured the funding to support this study. All authors reviewed the manuscript.

Thermally Introduced Bismuth Clustering in Ga(P,Bi) Layers under Group V Stabilised Conditions Investigated by Atomic Resolution *In Situ* (S)TEM.

R. Straubinger, M. Widemann, J. Belz, L. Nattermann, A. Beyer* and K. Volz

*Correspondence to [andreas.beyer@physik.uni-marburg.de]

Faculty of Physics and Materials Science Center, Philipps-Universität Marburg, Hans-Meerwein-Straße 6, Marburg, Hessen 35032, Germany

Abstract:

We report the formation of Bi clusters in Ga(P_{1-x},Bi_x) layers during an *in situ* (scanning) transmission electron microscopy ((S)TEM) annealing investigation. The non-destructive temperature regime in dependence on the tertiarybutylphosphine (TBP) pressure in the *in situ* cell was investigated to ensure that the results are not distorted by any destructive behaviour of the crystal during the thermal treatment. The following annealing series of the Ga($P_{92.6}Bi_{7.4}$) and Ga($P_{96.4}Bi_{3.6}$) layers reveals that the threshold temperature at which the Bi clustering takes place is 600 °C in the Ga($P_{92.6}Bi_{7.4}$) layer. Further thermal treatments up to 750 °C show a relationship between the Bi fraction in the Ga(P_{1-x},Bi_x) layer and the initial temperature at which the Bi clustering takes place. Finally, we investigate one Bi cluster at atomic resolution conditions. In these conditions, we found that the Bi cluster crystallized in a rhombohedral phase, aligning with its {101} planes parallel to the Ga(P,Bi) {202} planes.

Introduction:

Bi containing III/V semiconductor materials have seen growing interest due to their strong reduction of the band gap energy even with a small fraction of Bi[1–3]. Furthermore, a growing Bi content leads to a drastic increase of spin-orbit splitting[4]. For example in GaAs the band gap is reduced by about 90 meV per percent of Bi incorporation[2]. With a Bi fraction higher than 10 % the spin-orbit splitting becomes even larger than the band gap[5,6]. Due to this modification Auger recombination processes can be suppressed, leading to an increased efficiency in photonic devices. Several bismide materials showed similar properties to those mentioned ones in Ga(As,Bi) promising new applications in optoelectronics[7–11]. Further theoretical calculations on the properties Ga(P,Bi), which could be a promising candidate for tuning the emission of optical sources as well as for the fabrication of laser devices emitting in the telecommunication wavelength, were reported[12]. Since GaP can be grown nearly lattice matched on Si[13] the dynamic processes. *In situ* (scanning) transmission electron microscopy ((S)TEM) has been proven to be an outstanding technique for these kind of observations[21,22]. The compatibility of modern *in situ* holders with most TEMs makes this technique feasible for a wide range of research. *In situ* TEM systems, such as the Atmosphere system[23] developed and produced by Protochips Inc. (Morrisville, NC, USA), are enabling observations at gas pressures up to 1,000 hPa and temperatures of 1,000 °C. With these specifications the experimental growth conditions in terms of temperature and precursor pressure of MOVPE, which is commonly used to fabricate novel III/V semiconductor compounds, can be realized.

In this paper we use *in situ* (S)TEM to investigate the threshold temperature at which the local Bi clustering take place. Further we investigate the cluster formation process as a function of the Bi fraction of the Ga(P,Bi) layers under group V stabilized conditions. Furthermore, we give a detailed insight into the Bi cluster characteristics under atomic resolution conditions.

possibility to grow Ga(P,Bi) devices on Si exists[14]. The fabrication of materials with a high fraction of Bi is, however, challenging due to its highly metastable nature. Furthermore, the grown Bi containing materials have to have a very high quality in terms of crystal defects to be practical for optoelectronic applications. The investigation by Christian et al.[15] demonstrated a Bi incorporation of 3.2 % in GaP using a molecular beam epitaxy (MBE) setup. Later results on metal organic vapor phase epitaxy (MOVPE) grown Ga(P,Bi) samples by Nattermann et al.[14] showed a Bi incorporation of up to 8 %. In addition, *in situ* information with regards to Bi cluster formation during growth and post growth annealing is missing. Furthermore, the mechanisms involved are not yet understood[16,17]. Beside all successes, the optimization of growth conditions for functional III/V semiconductor materials is still very challenging as can be seen by the growing body of publications within this field[18–20]. In particular *in situ* information promises to deliver details about the growth mechanisms and can therefore help to improve the growth parameters. One of the advantages of *in situ* methods is that they are able live insights into

Experimental Methods:

The Ga(P_{1-x},Bi_x)/GaP sample studied in this work was grown by MOVPE using a commercially available Aixtron horizontal reactor system (AIX 200-reactor) with gas foil rotation. Triethylgallium (TEGa), tertiarybutylphosphine (TBP), and trimethylbismuth (TMBi) were used as precursors for Ga, P and Bi, respectively. The growth temperature for the Ga(P_{1-x},Bi_x) layer was set to 400 °C, while the GaP barriers growth temperature was set to 625 °C to remove surplus Bi from the surface. Further information, including a more detailed description of the MOVPE growth procedure of the Ga(P_{1-x},Bi_x)/GaP sample

is summarized thoroughly by Nattermann et al.[24]. The sample used for the present study consists of two 55 nm thick $Ga(P_{1-x},Bi_x)$ layers with Bi fractions of x=3.6 % and x=7.4 %, separated by GaP barriers with an approximate thickness of 100 nm. The Bi fraction of each $Ga(P_{1-x},Bi_x)$ layer is determined using secondary ion mass spectrometry (SIMS), with complementary high resolution X-ray diffraction (HRXRD) measurements taken for comparative purposes. Here a HRXRD pattern was simulated around the (004)-GaP substrate peak, assuming the GaBi lattice constant to be 6.33 Å[3]. Due to the micrometre sized spot of the XRD, the resulting content values represent an average values. Since potential clusters may exhibit a rhombohedral structure[16], it is unlikely that they influence these (004) rocking curves at all. The sample preparation for the presented *in situ* study was done using a JEOL JIB 4601F FIB system. The detailed preparation process of the lamella and the loading procedure of the finished specimen into the *in situ* cell will not be repeated here, but a detailed description can be found in Straubinger et al.[25]. In summary, an electron transparent lamella was prepared out of a wafer piece as described in Schaffer et al.[26]. Upon completion, the lamella was rotated by 90° along the long axis and mounted with the electron transparent section positioned precisely above the electron transparent SiN window of the thermal e-chip produced by Protochips Inc. The STEM investigations were performed in a double-C_S corrected JEOL JEM 2200 FS field emission TEM operating at 200 kV. For the *in situ* investigation, a modified atmosphere system with a gas environmental cell holder from Protochips Inc. was used. A detailed description of the system, the specifications, and the required modifications are given in Straubinger et al.[27]. This setup allows for high resolution (S)TEM investigation of III/V semiconductor materials in the growth temperature regime and under the necessary group V stabilization, which is indispensable when aiming to avoid group V desorption. Image generation was carried out in high angle annular dark field (HAADF) mode, also known as Z-contrast mode[28,29] due to the underlying Rutherford-like distribution of the scattered electrons. Hence, the detected intensity is proportional to $Z^{1.6-2}$, which helps to intuitively distinguish between different elements. In order to allow for determining thickness in later stages, the acquired images were normalized with respect to the impinging beam following the procedure described in He & Li[30]. The HAADF intensity is corrected by subtracting the intensity contribution of the SiN windows from the measured intensity of the crystalline sample. This approximation is justified because both SiN windows are amorphous and highly defocused. Subsequent comparison with complementary contrast simulation using the frozen phonon approximation available in STEMsim[31] was used to determine the lamella thickness. A more detailed description of all simulation parameters is given in[27].

Results and discussion:

This paper is organized as follows: first, by tracking the lamella thickness over the temperature for different TBP pressures in the *in situ* cell, it should be ensured that the following measurements are not influenced by any destructive behaviour of the crystal structure due to P desorption. Next, the initial Bi cluster formation temperature and the cluster characteristic in terms of cluster size and formation time is determined by analysing the intensity distribution within the $Ga(P_{1-x},Bi_x)$ layers for three temperature series covering the MOVPE growth temperature regime. Here, one question to be answered refers to the time during which the local Bi enrichment takes place in the growth process. Subsequent annealing studies at temperatures significantly above the growth temperature will ascertain the relationship between the Bi fraction in the $Ga(P_{1-x},Bi_x)$ layer and the initial Bi clustering temperature. Finally, a closer insight into the crystalline structure of the Bi clusters within the $Ga(P_{92.6},Bi_{7.4})$ layer will be given.

Figure 1 shows a HAADF STEM overview image of the investigated structure as grown, i.e without thermal treatment. As mentioned in the experimental section the sample consists of two $Ga(P_{1-x},Bi_x)$ layers with a different Bi content. The Bi fraction is indicated on the right hand side of the image. Every $Ga(P_{1-x},Bi_x)$ layer has a thickness of around 55 nm and is surrounded by approximately 100 nm of GaP. Due to the large atomic number of Bi (Z = 83), the clusters appear brighter in the HAADF STEM image. Some Bi enriched areas can be observed on the left hand side in the very top $Ga(P_{92.6},Bi_{7.4})$ layer. Due to the thickness of the lamella and the resulting overlay of the rhombohedral crystal structure of a pure Bi cluster and the surrounding zincblende host material, it is not possible to determine whether the bright areas are rhombohedral Bi clusters or Bi enriched zincblende $Ga(P_{1-x},Bi_x)$. Therefore, we will refer to the bright areas within the $Ga(P_{1-x},Bi_x)$ layer as clusters in the following. This is justified because the post thermal annealing investigation at a thin sample region reveals that the bright areas, which occur due to the thermal annealing, consist of rhombohedral Bi[16] as will be shown later. By taking a closer look at the areas around the brighter areas in figure 1 (some examples are marked by white arrows), a contrast variation is observable. These appearances might originate from Bi depleted tracks left from moving Bi during the cluster formation. Before investigation of the detailed characteristics of the Bi clusters, it should be clarified whether the cluster formation happens during the growth of the $Ga(P_{1-x},Bi_x)$ layer itself taking place at 400 °C or during the growth of overlying GaP layer acting as a 625 °C thermal annealing for the lower $Ga(P_{1-x},Bi_x)$ layers. To ensure no contribution of already existing Bi clusters, the experiments were carried out in areas with a homogeneous Bi distribution.

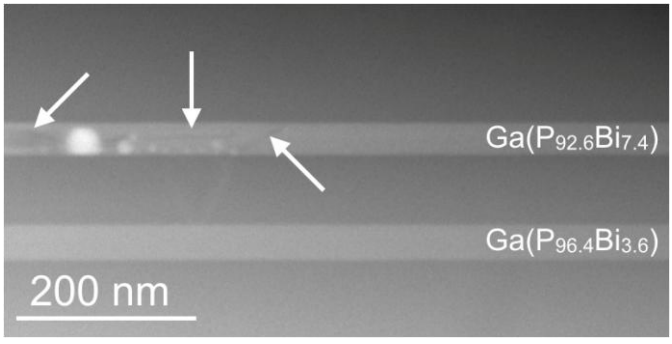

Figure 1: HAADF STEM overview image of the dedicated structure containing two 55 nm thick $Ga(P_{1-x},Bi_x)$ layers with different fractions of Bi embedded in approximately 100 nm thick GaP barriers. Some of the brighter appearing Bi clusters can be observed on the left hand side in the very top $Ga(P_{92.6},Bi_{7.4})$ layer. Around the brighter areas a contrast variation is observable which might originates from Bi depleted tracks left from moving Bi. (marked with white arrows).

To facilitate the investigation of III/V semiconductor materials *in situ* in the TEM at growth temperature regime, the crystal structure must be stabilized during the *in situ* annealing investigation to prevent group V desorption. This ensures that the observed changes do not occur due to structural degradation. One method to measure the sample destruction is to track the TEM lamella thickness during the *in situ* experiment. By doing so it is possible to identify the non-destructive temperature range in dependence of the group V stabilization. Figure 2 shows the results of these thickness measurements. Here, the thickness divided by the initial thickness ($t_{200\ °C}$) over the temperature is shown for an unstabilized environment and two different TBP pressures in the *in situ* cell. The red dots belong to the unstabilized annealing experiment, the black squares and blue triangles show the results of the thermal treatment experiments applying 140 hPa and 180 hPa TBP, respectively. It should be mentioned that the thickness measurement in the unstabilized experiment and in the annealing series with 140 hPa TBP in the cell was carried out on a different TEM lamella within a GaP region with approximately 3% B which is negligible in the analysis. By comparing the stabilized with the unstabilized experiment one can clearly see the tremendous difference in the sample stability during the thermal treatment. Furthermore, by comparing the thermal treatment experiment under 140 hPa TBP (black squares) and 180 hPa TBP (blue triangles) environments, the different non-destructive temperature regimes can be seen directly. With 180 hPa TBP in the cell the crystal structure is thermally stable up to 750 °C, whereas the sample annealed in the 140 hPa TBP environment starts to degrade at around 600 °C. As a result of these findings, all further *in situ* annealing investigations discussed in this paper are carried out under a 180 hPa TBP stabilization.

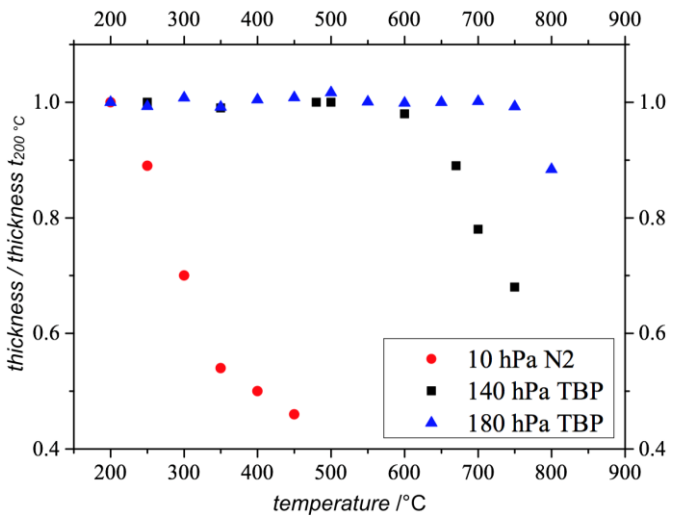

Figure 2: Plot showing the thickness divided by initial thickness ($t_{200\ °C}$) versus the temperature. The three measurements compare the non-destructive temperature regime of the GaP region of the TEM lamella without group V stabilization (red dots) with two different amounts of TBP (black squares 140 hPa TBP, blue triangles 180 hPa TBP) in the cell during the thermal annealing[27].

To identify the initial temperature at which the clustering takes place the temperature was gradual increased by 50 °C starting with 300 °C which is significantly below the growth temperature of 400 °C and 625 °C, respectively. For every series the temperature was kept for 30 to 45 minutes. The HAADF STEM images recorded during every series in an approximately two minute cycles are the basis for the Bi clustering study within the $Ga(P_{1-x},Bi_x)$ layer. The measured standard deviation of the intensity within the ternary $Ga(P_{1-x},Bi_x)$ layer divided by the mean intensity of the surrounding GaP matrix, hereinafter designated as σ_{rel}, is a measure for the inhomogeneity of the Bi distribution of the corresponding $Ga(P_{1-x},Bi_x)$ layer, as has been shown on the example of Ga(N,As,P) by Wegele and co workers[32]. It should be pointed out that due to the large difference in the surface to bulk ratio and the relaxed strain in the thin lamella, the absolute value for the initial temperature above which the clustering takes place in the MOVPE process and inside an electron transparent TEM lamella are not directly comparable. Nevertheless, the trend is the same and therefore the results presented in the following allow an *in situ* investigation of a specific MOVPE process inside the (S)TEM under high resolution conditions. Plot (a) in figure 3 shows the σ_{rel} within the $Ga(P_{92.6}Bi_{7.4})$ layer gained from the aforementioned HAADF STEM images over the time for three temperature steps. By taking a look at the data points of the 500 °C time series (black squares), no increase in σ_{rel} can be observed. This indicates that no local Bi enrichment takes place. It should be mentioned that this temperature is already 100 °C above the $Ga(P_{1-x},Bi_x)$ layer growth temperature of 400 °C. Also, by further increasing the temperature by 50 °C to 550 °C (red dots) no change in the structure is visible. The blue triangles represent the time series at 600°C, here the influence of the temperature on σ_{rel} within the $Ga(P_{92.6}Bi_{7.4})$ layer which originates from Bi clustering can be seen. It should be emphasised that post *in situ* energy dispersive X-ray spectroscopy (EDS) measurements shown in figure 5 (b) prove that the observable bright areas consists of Bi and do not consist of Ga which might form Ga droplets on the surface as observed in destructive temperature regimes. To better illustrate the process of Bi clustering a dashed line as a guide to the eye is added to the annealing series done at 600 °C in figure 3 (a). Taking a closer look at the curvature of this line, the time course of the structural change is directly observable. The clustering of Bi within the $Ga(P_{92.6}Bi_{7.4})$ layer takes around 40 minutes before the clusters reach a stable size. Later investigation, shown in figure 4, at higher temperatures will clarify whether the cluster size increases further with rising temperatures or if there is a stable Bi cluster formation over the whole temperature regime above the threshold temperature. The colour coded STEM images presented in figure 3 (b) show the formation of one big and two smaller Bi clusters during the temperature series at 600 °C. It is worth noting

that the very long investigation time of this experiment and the presence of the group V precursor gas in the *in situ* cell results in a carbon coating over the time which caused a reduction of the contrast in the STEM images. Therefore, the HAADF intensity in the micrographs presented in figure 3 (b) is color-coded from blue to red, since it enhances the visibility of the clusters. The time passed with respect to the start of the experiment at which each image is recorded is indicated at the very right hand side.

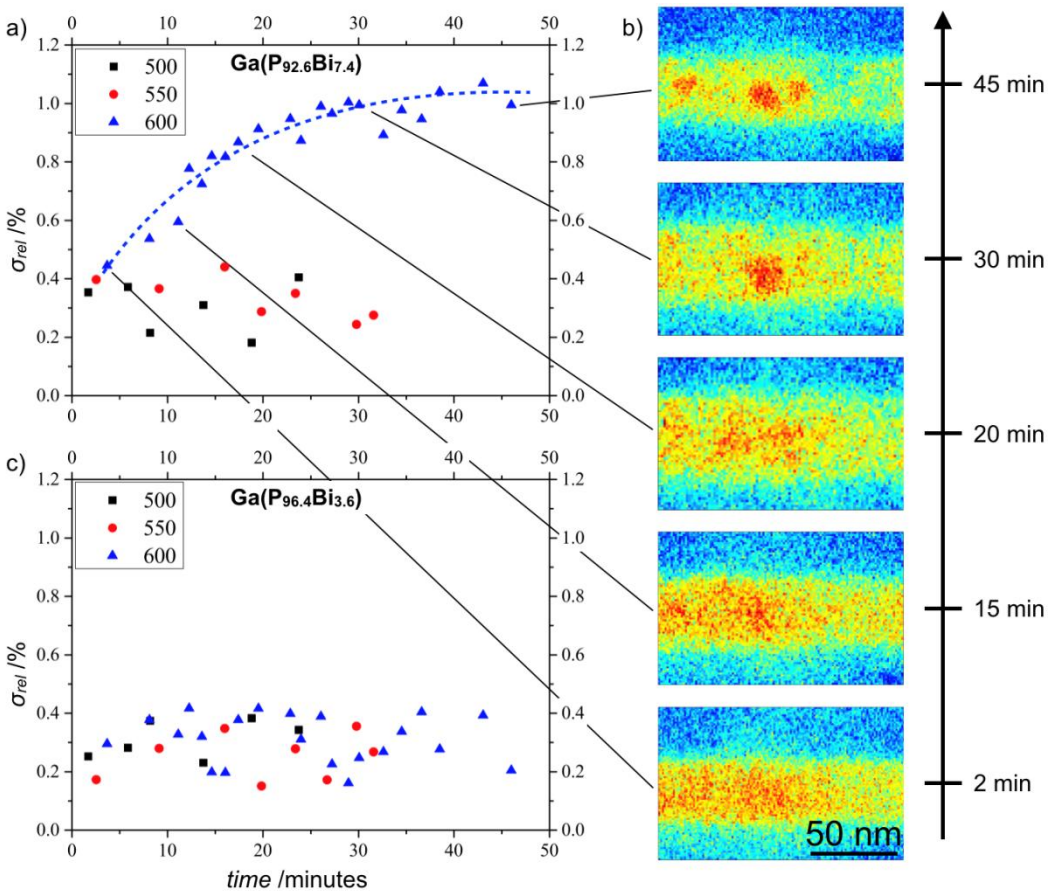

Figure 3: Plot (a) and (c) show σ_{rel}, i.e. standard deviation of the intensity within the ternary $Ga(P_{1-x},Bi_x)$ layer divided by the mean intensity of the surrounding GaP matrix, over the time within the $Ga(P_{1-x},Bi_x)$ layer with 7.4 % and 3.6% Bi, respectively. The temperature series were carried out at 500 °C (black squares), 550 °C (red dots) and 600 °C (blue triangles). The colour coded STEM images (b) show the formation of one big and two smaller Bi clusters within the $Ga(P_{92.6}Bi_{7.4})$ layer over time.

Furthermore, the black lines between the plot (a) and (b) relate the STEM image with the corresponding data point. It should be mentioned that the STEM images in figure 3 (b) show only a part of the larger images investigated to generate the data points presented in figure 3 (a). To further compare the Bi clustering in dependence of the Bi fraction, plot (c) in figure 3 shows σ_{rel} drawn over the time within the $Ga(P_{96.4}Bi_{3.6})$ layer. Here, no Bi clustering could be observed for all three temperature series, i.e. 500 °C, 550 °C, and 600 °C. Overall, the results presented in figure 3 already answer the question regarding the time during which the local Bi enrichment occurs within the growth process. It thus can be concluded that the $Ga(P_{92.6}Bi_{7.4})$ layer structure might grow without Bi clusters, and due to the subsequent GaP layer which has a growth temperature of 625 °C, the inhomogeneity of the Bi distribution takes place. This result is further supported by *ex-situ* investigations on $Ga(P_{92.6}Bi_{7.4})$ layers without a GaP cap, where no Bi clusters appear in the structure. Further experiments significantly above the growth temperature should demonstrate the relationship between the temperature at which Bi clustering takes place and the Bi fraction in the $Ga(P_{1-x},Bi_x)$ layer as well as if the cluster size in the $Ga(P_{92.6}Bi_{7.4})$ layer further increases with rising temperature. To further investigate the initialisation temperature with regard to the Bi fraction, the plots in figure 4 show σ_{rel} for the same $Ga(P_{1-x},Bi_x)$ layers presented in figure 3 but at temperatures significantly above the growth temperatures. It should be noted that the measurements of the $Ga(P_{92.6}Bi_{7.4})$ layer were carried out at a thinner section on the lamella, therefore the values of σ_{rel} are slightly different compared to the values in figure 3 (a). However, a closer look at the plot (a) in figure 4 reveals that there is no further inhomogeneity in the Bi distribution caused by increasing the temperature from 650 °C up to 750 °C. This confirms the previous observation that the Bi cluster formation reaches a stable size which is steady against higher temperatures. Due to the large spreading of the data points presented in figure 4 (b), dashed lines are added to the $Ga(P_{96.4}Bi_{3.6})$ layer measurements as a guide to the experiment. By comparing the series recorded at 650 °C (black squares) and the series measured at 700 °C (red dots), one cannot see any hint of Bi clustering which would lead to an increase of σ_{rel}. In contrast to that, it can be assumed that there is a rising σ_{rel} value in the annealing series recorded at 750 °C within the $Ga(P_{96.4}Bi_{3.6})$ layer. From that point of view one can speculate that the Bi fraction in the $Ga(P_{1-x},Bi_x)$ layers is directly related to the initial clustering temperature.

Unfortunately, it is not possible to further increase the temperature to investigate the Bi clustering in the Ga($P_{96.4}Bi_{3.6}$) layer without destroying the crystal structure in a 180 hPa TBP environment. Further studies carried out at higher TBP pressures will investigate this correlation in more detail.

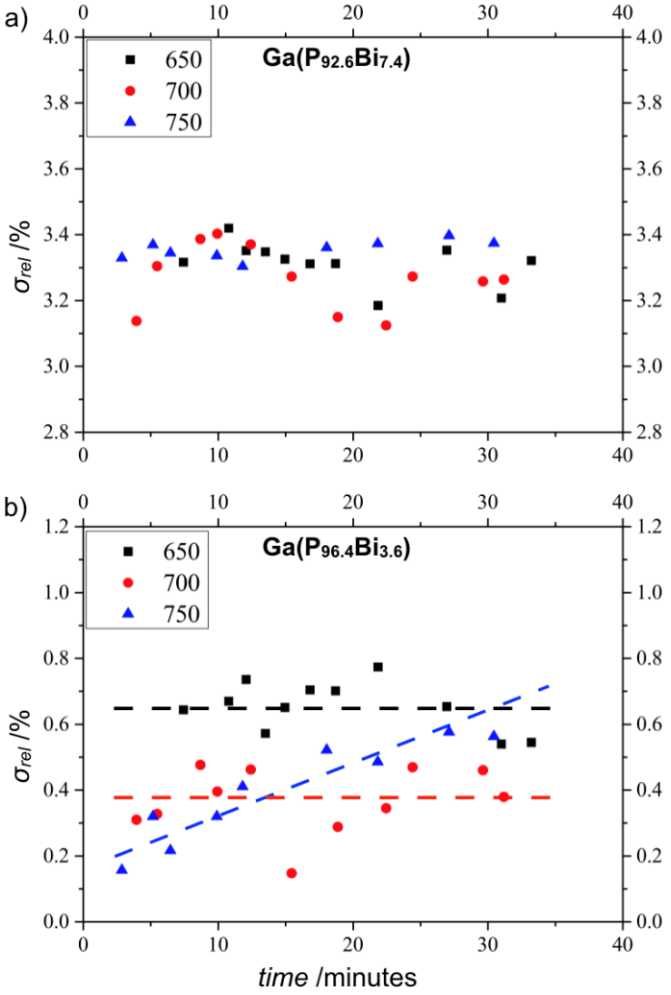

Figure 4: Plot (a) and (b) show σ_{rel} over the time within the Ga($P_{1-x}Bi_x$) layers with 7.4 % and 3.6% Bi. These measurements were performed at 650 °C (black squares), 700 °C (red dots) and 750 °C (blue triangles).

Figure 5 (a) shows a atomic resolution HAADF STEM image of one Bi cluster recorded in the Ga($P_{92.6}Bi_{7.4}$) layer after the thermal annealing experiment. To have tilting capability in both directions and orientate the sample precisely along the [010] viewing direction, the image is recorded in a standard double tilt holder. Here, the lattice planes corresponding to rhombohedral single crystal Bi are clearly resolved. The single crystalline lattice parameter for Bi were determined and published by D. Schiferl and C.S. Barrett [33]. Two rhombohedral Bi {101} planes with a spacing of 0.327 nm are highlighted in figure 5 (a) with white dashed lines. The inset in figure 5 (b) shows the inverted FFT of the STEM image shown in figure 5 (a). The FFT was calibrated using the {200} reflections of Ga(P,Bi) which retain the spacing of pure GaP due to the tetragonal distortion. Here the parallelism between the Bi {101} and the Ga(P,Bi) {202} planes is clearly visible. The aforementioned contrast variation resulting from Bi depleted regions due to migrating Bi during the formation of Bi cluster can also seen in the STEM image in figure 5 (a) at the lower right edge of the Bi cluster. The preferred moving direction seems to be along the [-101] and [101] direction. This was also observed in STEM images at higher magnifications. The plot in figure 5 (b) shows the EDS results of the region at the Bi cluster (black line) and for comparison at a region within the Ga($P_{92.6}Bi_{7.4}$) layer but without Bi clusters (red line). The counts per second (cps) over the energy in keV is plotted in the energy range around the $Bi_{M\alpha}$ edge. This result proves that the bright areas in the STEM images consist of Bi.

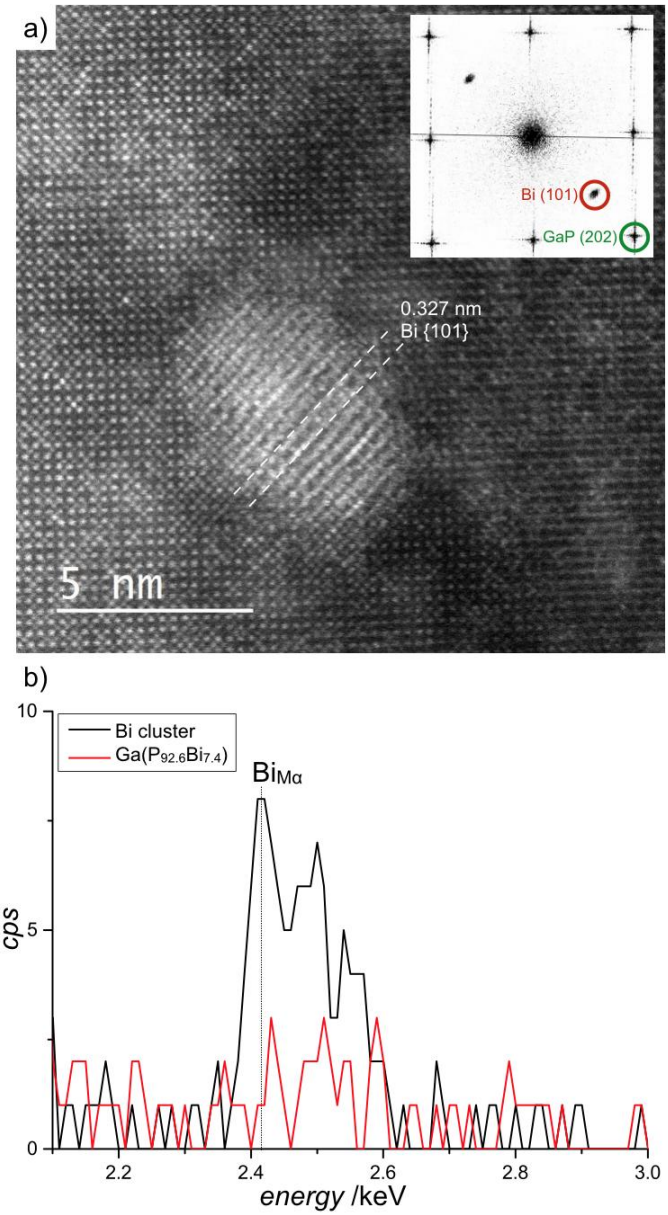

Figure 5: Atomic resolution HAADF STEM image of the Ga($P_{92.6}Bi_{7.4}$) layer. The brighter region in the middle of the image shows a Bi cluster embedded in the Ga($P_{92.6}Bi_{7.4}$) layer. The inset shows the inverted FFT of the STEM image shown in figure 5 (a). Plot (b) shows the EDS result of the $Bi_{M\alpha}$ edge derived from the region at the Bi cluster (black line) and from a region without any local Bi enrichment (red line).

Summary:

In this paper, we first demonstrate that the used *in situ* setup facilitates the investigation of III/V semiconductor materials in a TEM at growth temperature regime since it provides the necessary group V stabilization. Moreover, we

determine the temperature above which the Bi clustering takes place. We find that this initial temperature depends on the actual Bi fraction within the $Ga(P_{1-x},Bi_x)$ layers. By investigating the $Ga(P_{1-x},Bi_x)$ layers at even higher temperatures, we were able to conclude that there is no further Bi rearrangement. The process is most likely limited by the Bi amount available in the thin TEM lamella. Comparing these results to the findings of the as grown sample suggests that the Bi clustering during the MOVPE growth process most likely took place during the growth of the subsequent GaP layer which acts as a 625 °C thermal treatment of the lower $Ga(P_{1-x},Bi_x)$ layer. Finally, a closer look at the at a representative Bi cluster reveals its rhombohedral structure and its orientation relation to the Ga(P,Bi) matrix.

References

1. Alberi, K. *et al.* Valence band anticrossing in $GaBi_xAs_{1-x}$. *Appl. Phys. Lett.* **91,** 51909 (2007).
2. Francoeur, S. *et al.* Band gap of $GaAs_{1-x}Bi_x$, 0<x<3.6%. *Appl. Phys. Lett.* **82,** 3874–3876 (2003).
3. Tixier, S. *et al.* Molecular beam epitaxy growth of $GaAs_{1-x}Bi_x$. *Appl. Phys. Lett.* **82,** 2245–2247 (2003).
4. Fluegel, B. *et al.* Giant spin-orbit bowing in $GaAs_{1-x}Bi_x$. *Phys. Rev. Lett.* **97,** 67205 (2006).
5. Sweeney, S. J. & Jin, S. R. Bismide-nitride alloys: Promising for efficient light emitting devices in the near- and mid-infrared. *J. Appl. Phys.* **113,** 43110 (2013).
6. Usman, M., Broderick, C. A., Lindsay, A. & O'Reilly, E. P. Tight-binding analysis of the electronic structure of dilute bismide alloys of GaP and GaAs. *Phys. Rev. B - Condens. Matter Mater. Phys.* **84,** 245202 (2011).
7. Ludewig, P. *et al.* Electrical injection Ga(AsBi)/(AlGa)As single quantum well laser. *Appl. Phys. Lett.* **102,** 242115 (2013).
8. Das, S. K., Das, T. D., Dhar, S., de la Mare, M. & Krier, A. Near infrared photoluminescence observed in dilute GaSbBi alloys grown by liquid phase epitaxy. *Infrared Phys. Technol.* **55,** 156–160 (2012).
9. Bushell, Z. L. *et al.* Growth and characterisation of Ga(NAsBi) alloy by metal–organic vapour phase epitaxy. *J. Cryst. Growth* **396,** 79–84 (2014).
10. Das, T. D. The effect of Bi composition on the properties of $InP_{1-x}Bi_x$ grown by liquid phase epitaxy. *J. Appl. Phys.* **115,** 173107 (2014).
11. Das, S. C., Das, T. D. & Dhar, S. Infrared absorption and Raman spectroscopy studies of InSbBi layers grown by liquid phase epitaxy. *Infrared Phys. Technol.* **55,** 306–308 (2012).
12. Samajdar, D. P., Das, T. D. & Dhar, S. Valence band anticrossing model for $GaSb_{1-x}Bi_x$ and $GaP_{1-x}Bi_x$ using k.p method. *Mater. Sci. Semicond. Process.* **40,** 539–542 (2015).
13. Volz, K. *et al.* GaP-nucleation on exact Si (0 0 1) substrates for III/V device integration. *J. Cryst. Growth* **315,** 37–47 (2011).
14. Nattermann, L. *et al.* MOVPE growth of Ga(PBi) on GaP and GaP on Si with Bi fractions up to 8%. *J. Cryst. Growth* **463,** 151–155 (2017).
15. Christian, T. M., Beaton, D. A., Mascarenhas, A. & Alberi, K. Bismuth incorporation into gallium phosphide. *Proc. SPIE* **10174,** 101740F (2016).
16. Wu, M., Luna, E., Puustinen, J., Guina, M. & Trampert, A. Formation and phase transformation of Bi-containing QD-like clusters in annealed GaAsBi. *Nanotechnology* **25,** 205605 (2014).
17. Luna, E. *et al.* Spontaneous formation of three-dimensionally ordered Bi-rich nanostructures within $GaAs_{1-x}Bi_x$/GaAs quantum wells. *Nanotechnology* **27,** 325603 (2016).
18. Döscher, H. *et al.* GaP-interlayer formation on epitaxial GaAs(100) surfaces in MOVPE ambient. *J. Cryst. Growth* **464,** 2–7 (2017).
19. Paszuk, A. *et al.* In situ preparation of Si p-n junctions and subsequent surface preparation for III-V heteroepitaxy in MOCVD ambient. *J. Cryst. Growth* **464,** 14–19 (2017).
20. Navarro, A. *et al.* MOVPE growth of GaP on Si with As initial coverage. *J. Cryst. Growth* **464,** 8–13 (2017).
21. Unocic, K. A., Shin, D., Unocic, R. R. & Allard, L. F. NiAl Oxidation Reaction Processes Studied In Situ Using MEMS-Based Closed-Cell Gas Reaction Transmission Electron Microscopy. *Oxid. Met.* **88,** 495 (2017).
22. Hudak, B. M. *et al.* Real-time observation of the solid-liquid-vapor dissolution of individual tin(IV) oxide nanowires. *ACS Nano* **8,** 5441–5448 (2014).
23. Allard, L. F. *et al.* Novel MEMS-Based Gas-Cell/Heating Specimen Holder Provides Advanced Imaging Capabilities for In Situ Reaction Studies. *Microsc. Microanal.* **18,** 656–666 (2012).
24. Nattermann, L. *et al.* MOVPE growth of Ga(PBi) on GaP and GaP on Si with Bi fractions up to 8%. *J. Cryst. Growth* **463,** 151–155 (2017).
25. Straubinger, R., Beyer, A. & Volz, K. Preparation and Loading Process of Single Crystalline Samples into a Gas Environmental Cell Holder for In Situ Atomic Resolution Scanning Transmission Electron Microscopic Observation. *Microsc. Microanal.* **22,** 515–519 (2016).
26. Schaffer, M., Schaffer, B. & Ramasse, Q. Sample

preparation for atomic-resolution STEM at low voltages by FIB. *Ultramicroscopy* **114,** 62–71 (2012).

27. Straubinger, R., Beyer, A., Ochs, T., Stolz, W. & Volz, K. In Situ Thermal Annealing Transmission Electron Microscopy (TEM) Investigation of III/V Semiconductor Heterostructures Using a Setup for Safe Usage of Toxic and Pyrophoric Gases. *Microsc. Microanal.* **23,** 751–757 (2017).

28. Pennycook, S. J. Z-contrast stem for materials science. *Ultramicroscopy* **30,** 58–69 (1989).

29. Pennycook, S. J. & Jesson, D. E. High-resolution Z-contrast imaging of crystals. *Ultramicroscopy* **37,** 14–38 (1991).

30. He, D. S. & Li, Z. Y. A practical approach to quantify the ADF detector in STEM. *J. Phys. Conf. Ser.* **522,** 12017 (2014).

31. Rosenauer, A. & Schowalter, M. in *Microscopy of Semiconducting Materials* 170–172 (Springer, Dordrecht, 2007). doi:10.1007/978-1-4020-8615-1_36

32. Wegele, T. *et al.* Correlation of the nanostructure with optoelectronic properties during rapid thermal annealing of Ga(NAsP) quantum wells grown on Si(001) substrates. *J. Appl. Phys.* **119,** (2016).

33. Schiferl, D. & Barrett, C. S. The crystal structure of arsenic at 4.2, 78 and 299°K. *J. Appl. Crystallogr.* **2,** 30–36 (1969).

8.4 Local sample thickness determination via scanning transmission electron microscopy defocus series

Citation

A. Beyer, R. Straubinger, J. Belz, and K. Volz. Local sample thickness determination via scanning transmission electron microscopy defocus series. *Journal of Microscopy*, 262(2): 171–177, 2016[95]

Abstract

The usable aperture sizes in (scanning) transmission electron microscopy ((S)TEM) have significantly increased in the past decade due to the introduction of aberration correction. In parallel with the consequent increase of convergence angle the depth of focus has decreased severely and optical section- ing in the STEM became feasible.Here we apply STEMdefocus series to derive the local sample thickness of a TEM sample. To this end experimental as well as simulated defocus series of thin Si foils were acquired. The systematic blurring of high resolution high angle annular dark field images is quantified by evaluating the standard deviation of the image intensity for each image of a defocus series. The derived dependencies exhibit a pronounced maximum at the optimum defocus and drop to a background value for higher or lower values. The full width half maximum (FWHM) of the curve is equal to the sample thickness above a minimum thickness given by the size of the used aperture and the chromatic aberration of themicroscope. The thicknesses obtained from experimen- tal defocus series applying the proposed method are in good agreement with the values derived from other established methods. The key advantages of this method compared to others are its high spatial resolution and that it does not involve

Contributions

My contribution of this work was the preparation of an electron transparent TEM lamella with perfectly parallel side facets. Andreas Beyer and myself executed the experimental data. Andreas Beyer and Jürgen Belz analyzed the data. Kerstin Volz supervised the work and secured the funding to support this study. All authors reviewed the manuscript.

Journal of Microscopy

Journal of Microscopy, Vol. 262, Issue 2 2016, pp. 171–177 doi: 10.1111/jmi.12284
Received 9 April 2015; accepted 3 June 2015

Local sample thickness determination via scanning transmission electron microscopy defocus series

A. BEYER, R. STRAUBINGER, J. BELZ & K. VOLZ
Materials Science Center and Faculty of Physics, Philipps-Universität Marburg, 35032 Marburg, Germany

Key words. STEM, aberration correction, silicon, defocus series.

Summary

The usable aperture sizes in (scanning) transmission electron microscopy ((S)TEM) have significantly increased in the past decade due to the introduction of aberration correction. In parallel with the consequent increase of convergence angle the depth of focus has decreased severely and optical sectioning in the STEM became feasible. Here we apply STEM defocus series to derive the local sample thickness of a TEM sample. To this end experimental as well as simulated defocus series of thin Si foils were acquired. The systematic blurring of high resolution high angle annular dark field images is quantified by evaluating the standard deviation of the image intensity for each image of a defocus series. The derived dependencies exhibit a pronounced maximum at the optimum defocus and drop to a background value for higher or lower values. The full width half maximum (FWHM) of the curve is equal to the sample thickness above a minimum thickness given by the size of the used aperture and the chromatic aberration of the microscope. The thicknesses obtained from experimental defocus series applying the proposed method are in good agreement with the values derived from other established methods. The key advantages of this method compared to others are its high spatial resolution and that it does not involve any time consuming simulations.

Introduction

Defocus series in transmission electron microscopy (TEM) mode are well known and applied regularly for a variety of materials (Kirkland *et al.*, 1980; Kirkland, 1984; Op De Beeck *et al.*, 1996). However, changing the defocus in scanning TEM (STEM) mode deliberately is rather new. Nevertheless, due to the large condenser apertures usable in C_S–corrected microscopes and the resulting reduction of depth of focus Δz_{DOF}, one can obtain valuable information on the three-dimensional structure of a sample (Borisevich *et al.*, 2006; Einspahr & Voyles, 2006; Behan *et al.*, 2009). The depth of focus is given by

$$\Delta z_{DOF} = \frac{1.7\lambda}{\alpha^2}, \quad (1)$$

where α is the semiconvergence angle of the electron probe (Cosgriff *et al.*, 2008). Utilizing this depth sensitivity, STEM defocus series were for example used to measure the chromatic aberration constant (C_C) of the used microscope (Kuramochi *et al.*, 2009), to investigate the distribution of dopant atoms (Borisevich *et al.*, 2006) within a sample or to measure the size of nanoparticles (Behan *et al.*, 2009).

Here we show how STEM defocus series can be used to determine the actual sample thickness by evaluating the systematic blurring of the image when changing defocus. The sample thickness is an indispensible parameter for the quantification of (S)TEM images, therefore many different methods have been proposed to determine it. Utilizing measurements in reciprocal space convergent beam electron diffraction (CBED) can be applied (Buxton *et al.*, 1976; Eades, 1986) in TEM mode whereas position averaged CBED (PACBED) (Lebeau *et al.*, 2010) is valuable in STEM mode. In real space the sample thickness can for example be determined by comparing high-angle annular dark field (HAADF) intensity to adequate simulations (Rosenauer *et al.*, 2009) Furthermore, as energy filters become widespread electron energy loss spectroscopy (EELS) is applied regularly (Egerton & Malac, 2005). Another method which utilizes STEM defocus series is proposed in Grillo & Carlino (2008). In contrast to the method proposed in this manuscript, the method of Grillo and Carlino relies on the evaluation of Fourier component with respect to the applied defocus.

The approach presented in this paper is comparably simple but is only applicable for crystalline materials in zone axis geometry. Nevertheless, we will show that its inherent advantages over other techniques make it suitable to accompany quantitative high resolution HAADF measurements.

The paper is organized as follows: we will investigate the physical effects occurring when changing the defocus with the help of multislice frozen phonon simulations. This allows determining the decisive dependencies without any disturbing influences from experimental noise, aberrations of the lenses in the microscope and inhomogenities of the sample. Accordingly we will derive a method to determine the sample thickness and demonstrate its applicability in real samples. Finally, we will compare our results to the ones of other established

Correspondence to: A. Beyer, Materials Science Center and Faculty of Physics, Philipps-Universität Marburg, Hans-Meerwein-Straße 6, 35032 Marburg, Germany. Tel: +49 6421 28 25704; fax: +4964212828935; e-mail: andreas.beyer@physik.uni-marburg.de

techniques, that is, EELS and the comparison of measured and simulated HAADF intensity.

Experiment

To investigate the dependence of the HAADF intensities on the defocus we choose silicon as a model system as it is one of the most commonly used materials in the semiconductor industry. Furthermore, its material parameters are well known. However, there is no limitation to this material. A JEOL JIB-4601F FIB/SEM was used to prepare plan parallel electron transparent samples with defined thicknesses, as by standard grinding preparation technique a thickness gradient cannot be avoided. The so called FIB lift-out technique is well established and described, for example, in Schaffer *et al.* (2012). To investigate the later TEM sample along the [010] zone axis the lamella was prepared with an angle of 45° with respect to the cleave edges of the substrate. With the help of the manipulator needle it is possible to lift the (20 μm × 2 μm × 4 μm, length × width × depth) lamella out of the sample and fix it to a TEM lift-out grid. During the thinning to a final thickness of (30–50) nm, the angle between the lamella and the gallium beam was gradually reduced, ensuring that the bottom and top surface of the electron transparent area are parallel and without any thickness gradient. Meanwhile, the voltage was lowered from 30 kV to 3 kV at the final polishing step.

The samples were characterized in a double aberration corrected JEOL JEM-2200 FS. The microscope was operated at E_0 = 200 kV, the annular detector collects scattered intensity in the range between 73 mrad and 173 mrad and the used condenser aperture results in a semiconvergence angle of the beam of 24 mrad. Image series were acquired changing the defocus from −75 nm to 50 nm using an increment of 3 nm, which was calibrated using the CEOS corrector software. The images were normalized with respect to the impinging beam similar to the approach used in literature (LeBeau & Stemmer, 2008; He & Li, 2014). The actual beam current was determined to 25.3 pA by imaging the direct beam on the Ultrascan 1000 CCD camera.

To model the scattering process complementary image simulations were carried out using the frozen phonon approximation of the STEMSIM code (Rosenauer & Schowalter, 2008). Defocus series were simulated varying the defocus from −65 nm to 15 nm in steps of 1 nm for different sample thicknesses up to 50 nm. The residual aberrations measured in the experiment were used as input parameters for the formation of the electron probe in the simulation. To model the effect of chromatic aberration, simulated images for different defoci were summed weighting their individual contribution by a Gaussian function with a full width half maximum (FWHM) of Δz_{CC}, which is connected to the chromatic aberration coefficient C_C by

$$\Delta z_{CC} = 2\, C_C \times \frac{dE}{E_0}\sqrt{(2\log 2)}. \qquad (2)$$

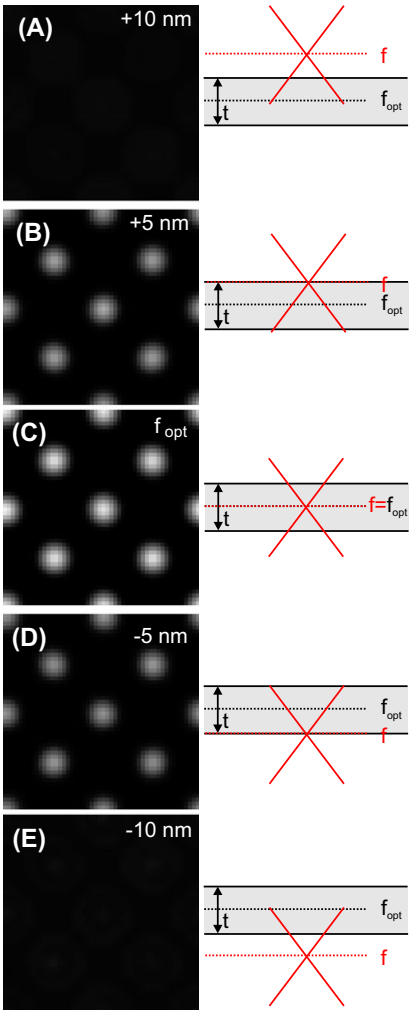

Fig. 1. Exemplary images from simulated HAADF intensity of Si for defocus values around the optimum defocus f_{opt} (A)–(E). The right panel illustrates the position of the focus with respect to the sample.

For the JEOL JEM-2200 FS microscope with a C_C of 1.5 mm and a dE of 0.42 eV follows a Δz_{CC} of 7.5 nm at 200 kV acceleration voltage (Kuramochi *et al.*, 2009). Complementary thickness measurements were carried out utilizing EELS using a condenser semiangle of 24 mrad and a collection angle of 9.5 mrad. The evaluation was done by applying the Kramers–Kronig sum rule (Egerton & Malac, 2005) to the energy loss spectrum which is implemented in the Digital Micrograph software.

Results

Changing the defocus away from its optimum value given by Haider (2000) qualitatively results in loss of contrast ultimately leading to the loss of spatial resolution (Kuramochi *et al.*, 2009).

This behaviour is summarized in Figure 1 where in the left panel simulated HAADF images of a Si area with the width of

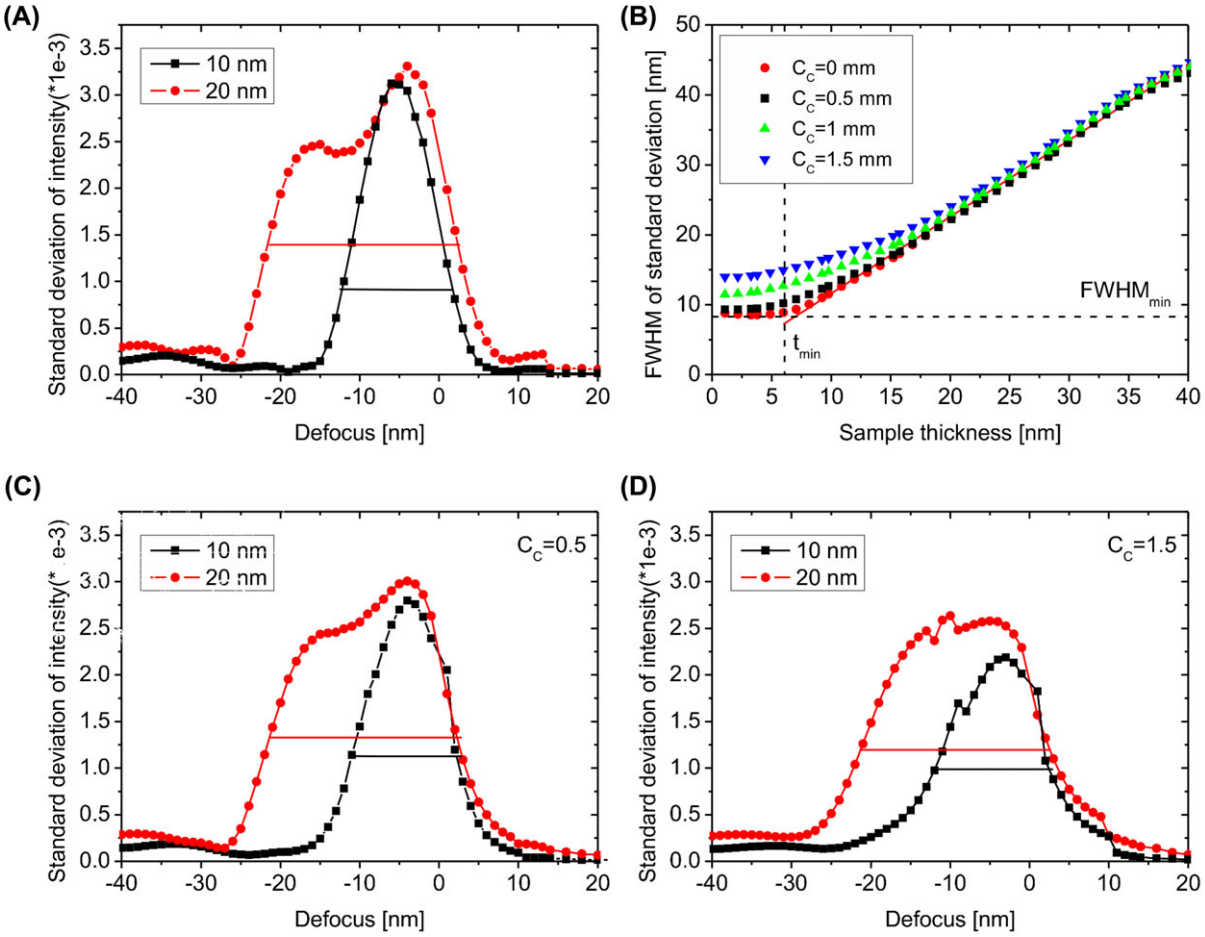

Fig. 2. Standard deviation of the HAADF intensity (STD_I) of simulated images with respect to the used defocus for a sample thickness of 10 nm (black) and 20 nm (red) (A). Please note that the y axis is in units of 10^{-3}. The FWHM of the curves increases with the sample thickness (B). Above a minimum thickness t_{min} the FWHM exhibits a linear behaviour. Taking into account C_C, the maximum of the standard deviation is quenched ($C_C = 0.5$ mm; (C)) and $C_C = 1.5$ mm; (D)) and t_{min} is increased.

one unit cell and a thickness of approximately 10 nm (18 unit cells) in electron beam direction are shown for different defocus values. The intensity scale is kept constant for all images and is chosen according to the dynamic range of Figure 1(C), that is, the image with the highest contrast. The right panel illustrates the position of the focus with respect to the optimum focus f_{opt} for each simulation. The depicted images in Figure 1 serve as examples, all conclusions drawn in the following are based on the whole dataset consisting of 80 individual simulations for defocus values from −65 nm to 15 nm for sample thicknesses up to 50 nm. At the optimum defocus value (Fig. 1(C)) the image exhibits the maximum contrast as the HAADF intensity is high on the atomic columns and small in the background between the columns. By changing the defocus by 10 nm in positive (Fig. 1(A)) or negative (Fig. 1(E)) direction the intensity on the atomic columns decreases drastically whereas the mean intensity remains constant, finally resulting in the vanishing of the contrast.

A good measure to quantify this behaviour is the standard deviation of the intensity (STD_I) of the simulated image. It is worth noting that the image contrast, given by $(I_{max} - I_{min})/(2I_{mean})$, is an adequate measure as well. The terms I_{max} and I_{min} denote the maximum and minimum image intensity, respectively, and I_{mean} is the mean image intensity. Nevertheless, the standard deviation of the image intensity is less sensitive to experimental noise. The STD_I of the simulated defocus series of the 10 nm thick sample are drawn as black data points versus the defocus values in Figure 2(A). The STD_I exhibits a pronounced maximum at the optimum defocus and drops to a background value for higher or lower values. The horizontal black line represents the FWHM of the curve and is just a guide to the eye. In the following, the actual FWHM values were derived by fitting a Gaussian to the data. The corresponding graph for a sample twice as thick, that is, 20 nm, is shown with red dots. The shape of the curve is more complex compared to the one of the 10 nm thick sample, that is, the

maximum is no longer symmetric around the optimum focus. As the shape of the electron probe is nearly symmetric with respect to the defocus for small aberrations, we attribute this behaviour to the propagation of the beam through the sample. However, the most notable difference between the graphs for the two different thicknesses is the increase in FWHM. This means the defocus can be changed over a wider range, still retaining image contrast. Roughly speaking, as long as the focus is inside the sample the image will appear sharp. If the focus is outside of the sample the image will blur. To verify this, the determined FWHM values are drawn as red data points versus the thickness of the simulated samples in Figure 2(B). For samples with thicknesses below a minimum t_{min} the determined FWHM value remains constant. This is when the sample thickness is smaller than Δz_{DOF}, which is 7.4 nm here (Eq. 1). In this region, the change of the image with defocus is mainly due to the shape of the probe and not due to the sample. Above this minimum thickness, the FWHM increases monotonically with the sample thickness. The fitted curve (red line in Fig. 2(B)) has a slope of 1.037 ± 0.00623, so the width is directly proportional to the sample thickness. Therefore, the local sample thickness can be determined by evaluating the standard deviation of the intensity of a defocus series.

For actual electron microscopes, chromatic aberration has to be considered which significantly influences the HAADF intensity and quenches the contrast in real images (Kuramochi *et al.*, 2009; Dwyer *et al.*, 2012). In a defocus series, a finite C_{C} causes that the set defocus is not distinct but is smeared out. This is usually described by a Gaussian with a FWHM Δz_{CC}, given by (Eq. 2), centred around the set defocus (Kuramochi *et al.*, 2009). To model the effect of the chromatic aberration, simulated images within a defocus range depending on Δz_{CC} were summed up. The contribution of each individual image was weighted according to a Gaussian function. The dependence of the standard deviation of the image intensity on the defocus for $C_{\mathrm{C}} = 0.5$ mm ($\Delta z_{\mathrm{CC}} = 2.5$ nm) and $C_{\mathrm{C}} = 1.5$ nm ($\Delta z_{\mathrm{CC}} = 7.5$ nm) is shown in Figures 2(C) and (D), respectively. Comparing these graphs to the one without C_{C} (Fig. 2(A)) it becomes obvious that the maximum is quenched, reflecting the loss of image contrast due to chromatic aberration (Kuramochi *et al.*, 2009; Dwyer *et al.*, 2012). Moreover, the curves smear out, while the effect is much more prominent for the thinner sample, resulting in a larger FWHM value. The determined FWHM values of the curves for all simulated thicknesses are drawn in Figure 2(B). It is visible that t_{min} increases with increasing C_{C}. Its value is given by $(\Delta z_{\mathrm{DOF}} + \Delta z_{\mathrm{CC}})^{\frac{1}{2}}$.

Before we apply this method to a real sample we will briefly discuss its inherent limitations and advantages. The biggest disadvantage compared to other methods is that it is limited to crystalline samples in zone axis geometry as it is based on the systematic loss of contrast. The spatial resolution is laterally in the angstrom range as an image of a few atomic columns is necessary to quantify the loss of contrast. As already stated above the minimum thickness t_{min} which can be determined accurately is given by the size of the used aperture when chromatic aberration is neglected. Following Eq. (1), a semiconvergence angle of 65 mrad would be needed to achieve a t_{min} of 1 nm. Due to the correction of higher order aberrations in the current generation of instruments values above 40 mrad are already reported (Sawada *et al.*, 2014). However, the preparation of such thin specimens is not trivial (Voyles *et al.*, 2003). When a finite C_{C} is taken into account, the minimum determinable thickness is significantly increased. For the parameters of the used JEOL JEM-2200 FS, Δz_{DOF} is 7.4 nm and Δz_{CC} is 7.5 nm, accordingly the minimum sample thickness which can be measured is around 11 nm. However, the maximum measurable thickness t_{max} is determined by the loss of contrast in thick samples. Here effects like multiple scattering, absorption and beam broadening lead to an additional loss of intensity on the columns which will influence the standard deviation of an experimental image and quench the effect of changing the defocus. Therefore, t_{max} also depends on the studied sample material.

Experimental defocus series of Si in a [010] projection were acquired to prove the applicability of the introduced method. The zone axis was aligned very carefully utilizing the CBED pattern on the CCD camera, to avoid an unintentional tilt of the crystal. As observed, for example, in Yamazaki *et al.* (2002), small object tilts can result in an intensity difference between atomic columns of a silicon dumbbell in [110] projection. As this effect is caused by an asymmetry of the probe tails we think this effect is minor in the used C_{S}-corrected microscope. Moreover, the effect should be even less prominent in the [010] projection investigated in this study, as the separation of the atomic columns is bigger.

The sample thickness at the region of the defocus series was also measured using established methods, that is, the comparison of the measured HAADF intensity with simulation (Rosenauer *et al.*, 2009) and EELS (Egerton & Malac, 2005).

Therefore, in Figure 3(A), the simulated HAADF intensity of Si averaged across one unit cell is drawn versus the sample thickness. The mean intensity of the 30 experimental images is $(1.05 \pm 0.002)\%$ of the impinging beam which leads to a local thickness t_{HAADF} of (24.5 ± 0.5) nm. The corresponding EELS spectrum acquired in the same region is shown in Figure 3(B). Applying the Kramers–Kronig method (Egerton & Malac, 2005), a thickness t_{EELS} of (36.4 ± 3) nm was derived. Both methods confirm that the region has a thickness above the expected t_{min} of 15 nm therefore the thickness should be measureable via a defocus series.

Exemplary sections of images from the acquired experimental defocus series are shown in Figures 4(A)–(E). The actual acquired images have a larger field of view of around (5×5) nm^2 sampled by (512×512) pixels. A region of only (80×80) pixels is shown in Figure 4 to increase the visibility of the decisive image features. In analogy to the simulated data (Figs. 1(A)–(E)) the intensity scale is adjusted according to the image with the highest contrast, that is, Figure 4(C). Like the

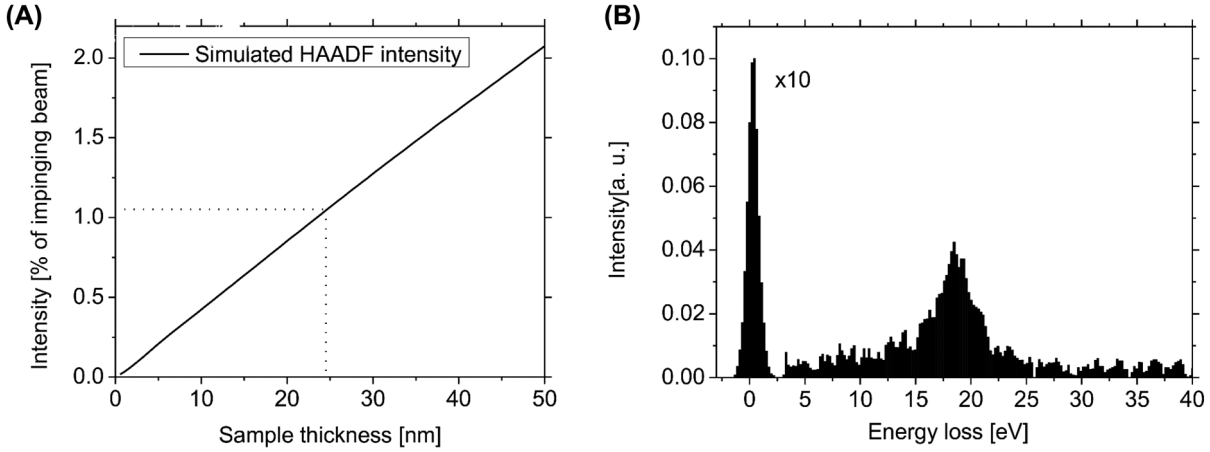

Fig. 3. Simulated HAADF intensity in dependence of the sample thickness (A). The dotted line represents the measured intensity in the region of interest (1.05%) and the deduced thickness (24.5 nm). Low loss EELS spectrum of the same region (B). Evaluation according to Kramers–Kronig sum rule (Egerton & Malac, 2005) leads to a thickness of 36 nm.

corresponding simulated data the experimental images show the expected behaviour, that is, the loss of contrast at high defocus values. The dependence of the measured standard deviation of the intensity on the defocus is shown as black curve in Figure 4(K). For better comparability the axes were chosen on the same scale as the simulated data (Fig. 2).

As expected, the graph exhibits a maximum at the optimum defocus value. Compared to the corresponding graph derived from the simulated data (Fig. 2(A)) the asymmetric shape is resembled very well, whereas the maximum is less pronounced which reflects the worse signal-to-noise ratio compared to the simulation. Moreover, the minimum value of the standard deviation is not zero due to the presence of additional experimental noise. This noise is in the range of 10^{-3} and is of the same order of magnitude as the investigated change of STD_I when changing the defocus. Therefore the evaluation is deteriorated. To increase the signal-to-noise ratio and facilitate the evaluation, the experimental data were treated according to the procedure described in the following.

The individual atomic columns in the image were detected with the help of the Peak Pairs software (Galindo *et al.*, 2007). With an in house written Matlab code a region around each peak was defined. In this example, a width of (80 × 80) pixels was chosen. Afterwards the intensities of the corresponding pixels in each region were summed up and divided by the number of regions, which is 894 here. From this follows a representative averaged region with highly increased signal-to-noise ratio. The atom positions were found in the image exhibiting the highest contrast and were retained for the remaining images. In this way still corresponding parts of the crystal were summed up and the signal-to-noise ratio can be increased drastically, even if the sample is drifting in between images. This becomes obvious when comparing the unprocessed defocus series (Figs. 4(A)–(E)) to the corresponding processed images (Figs. 4(F)–(J)). Due to the improved contrast even at defoci far away from the optimum as in Figures 4(H), (F) and (J), the atomic columns become visible in the processed images. The standard deviation of the image intensity of the processed images with respect to the defocus is drawn as red curve in Figure 4(K). We decided to apply this averaging method because the more straight-forward low pass filter may artificially influence the contrast within an image and therefore interfere with the subsequent evaluation, whereas our approach leaves the contrast unaffected. For comparison the STD_I graph derived from the low pass filtered series is drawn as green curve in Figure 4(K). The averaging procedure decreased the noise level so drastically, that a wide range of defoci can be evaluated now. The asymmetric shape of the curve becomes even clearer from the averaged data (red curve). The determined width of the curve is 26 nm. Following the conclusions drawn from Figure 2(D), the local sample thickness is 27 nm. The maximum value of the experimental defocus curve is still reduced in comparison to the simulated data as the contrast is still worse in the experiment, presumably due to the presence of residual aberrations or a finite source size neglected in the simulation. Therefore, to finally compare simulation and experiment both were normalized to their respective maximum and are drawn in Figure 4(L). The agreement between the experimental (red line) and the simulated curve (black line) derived for a sample thickness of 27 nm and a C_C of 1.5 mm is very good. The thicknesses derived from the defocus series is in very good agreement with the value from HAADF intensity whereas there is a notable deviation from the value derived from the EELS measurement.

There are several possible reasons for the small discrepancy between the thickness values derived by the different methods. The defocus series is rather insensitive to any amorphous layers introduced by the FIB preparation whereas HAADF

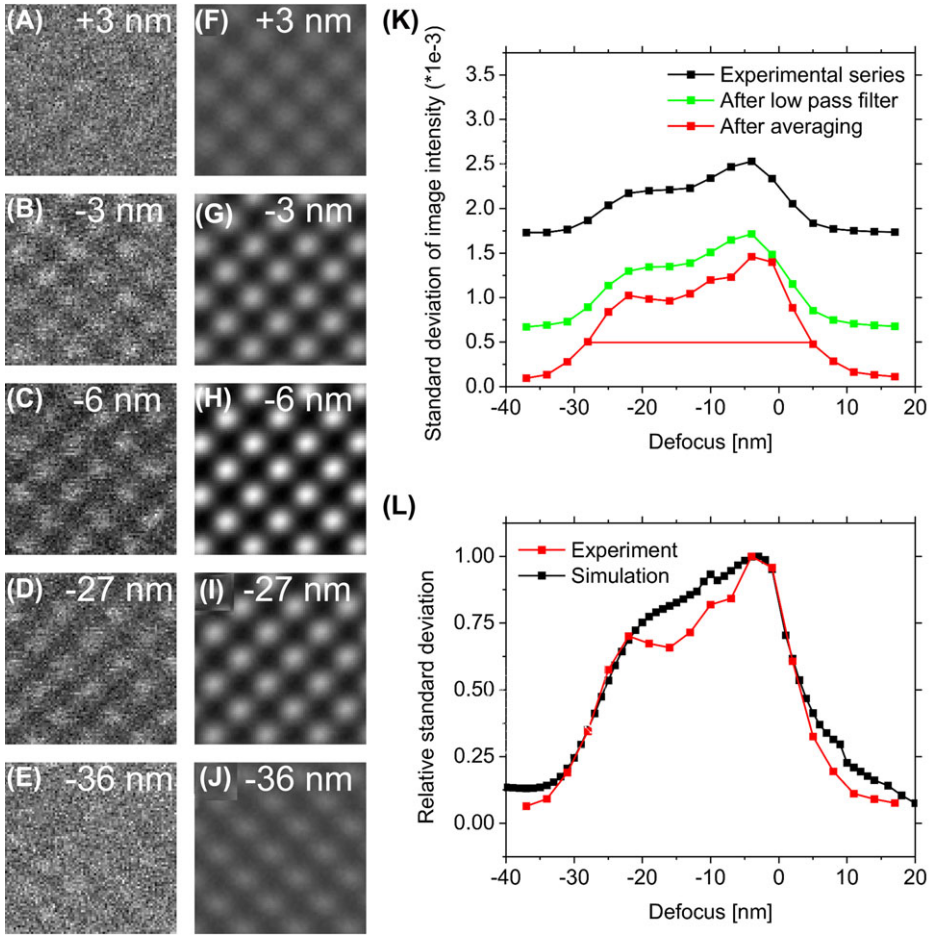

Fig. 4. Sections of experimental defocus series (A)–(E). The signal-to-noise ratio is significantly increased by an averaging procedure (F)–(J). The dependence of the STD_I on the defocus for the unprocessed (black curve), the low pass filtered (green curve) and the averaged data (red curve) is shown in (K). Please note that the y axis is in units of 10^{-3}. The averaged experimental data (red curve) are compared to the simulated data (black curve) in (L). Both datasets were normalized to their respective maximum.

intensity and in particular the EELS signal will be significantly influenced by the presence of additional non crystalline material. This may be the reason why the thickness value derived by EELS is higher as the value derived from the defocus series. As the defocus method relies on the acquisition of a series of images it is particularly sensitive to drift. Whereas drift in x- or y-direction is negligible if the sample is periodic, drift in z-direction leads to an unintentional change in defocus and a subsequent error in thickness determination. To minimize the effect of mechanical drift, the measurement was not acquired directly after the insertion of the holder and the stage was allowed to settle for several minutes before each measurement. In addition the sampling and the dwell time were reduced to acquire a full series in less than 3 minutes. Supplementary time dependent focus measurements utilizing the CEOS software verify that the focus change over 3 minutes is below 5 nm.

Although the presented method is limited to crystalline material in zone axis, it is very suitable to accompany quantitative high-resolution HAADF STEM, because of its accuracy and spatial resolution. Moreover, it is especially suitable for sample thicknesses investigated in HRSTEM in contrast to CBED which usually is more accurate at thicker samples (Buxton *et al.*, 1976; Eades, 1986). Furthermore the presented method profits from high semiconvergence angles which handicap the application of PACBED due to the complicated overlapping of discs. The presumably biggest advantage is its simplicity as it does not involve time consuming simulations. It only requires an experimental focal series and the calibration of the focus step of the microscope. The proposed method is also compatible with the one proposed by Grillo and Carlino, with which complementary evaluation could be done in the Fourier domain. Moreover, it is worth noting that the sample thickness is not the only quantity retrievable from such defocus series. With more advanced evaluation accompanied by additional simulation even more valuable information on the three-dimensional structure of a sample may be gained. With a well-known

sample, the problem might as well be inverted and a defocus series may be used to investigate the used electron probe and determine unknown microscope parameters.

Conclusions

This paper shows the benefit of defocus series in STEM via the example of sample thickness determination. High-resolution STEM images systematically blur when changing the defocus away from its optimum value. The thicker the samples the larger is the range of defoci, in which the image remains sharp. The standard deviation of the intensity can be used to quantify this behaviour. The standard deviation shows a peak around the optimum defocus and the FWHM of this peak is directly proportional to the sample thickness. Accordingly by evaluating an experimental defocus series it is possible to derive the local sample thickness with very high accuracy. The determined thickness values are in good agreement to those of other established techniques.

Acknowledgements

This work has been supported by German Science Foundation (DFG) in the framework of GRK 1782 ('Functionalization of semiconductors') and SFB 1083 ('Structure and dynamics of internal interfaces').

References

Behan, G., Cosgriff, E.C., Kirkland, A.I. & Nellist, P.D. (2009) Three-dimensional imaging by optical sectioning in the aberration-corrected scanning transmission electron microscope. *Philos. Transact.: Ser. A, Math., Phys., Eng. Sci.* **367**, 3825–3844.

Borisevich, A.Y., Lupini, A.R. & Pennycook, S.J. (2006) Depth sectioning with the aberration-corrected scanning transmission electron microscope. *Proc. Nat. Acad. Sci. U.S.A.* **103**, 3044–3048.

Buxton, B.F., Eades, J.A., Steeds, J.W. & Rackham, G.M. (1976) The symmetry of electron diffraction zone axis patterns. *Philos. Transact. R. Soc. A: Math., Phys. Eng. Sci.* **281**, 171–194

Cosgriff, E.C., D'Alfonso, A.J., Allen, L.J., Findlay, S.D., Kirkland, A.I. & Nellist, P.D. (2008) Three-dimensional imaging using aberration-corrected scanning transmission and confocal electron microscopy. *J. Phys.: Conf. Ser.* **126**, 1–4.

Dwyer, C., Maunders, C., Zheng, C.L., Weyland, M., Tiemeijer, P.C. & Etheridge, J. (2012) Sub-0.1 nm-resolution quantitative scanning transmission electron microscopy without adjustable parameters. *Appl. Phys. Lett.* **100**, 012036.

Eades, J.A. (1986) Convergent-beam techniques in transmission electron microscopy. *Appl. Surf. Sci.* **26**, 280–293.

Egerton, R.F. & Malac, M. (2005) EELS in the TEM. *J. Electr. Spectrosc. Related Phenom.* **143**, 43–50.

Einspahr, J.J. & Voyles, P.M. (2006) Prospects for 3D, nanometer-resolution imaging by confocal STEM. *Ultramicroscopy* **106**, 1041–1052.

Galindo, P.L., Kret, S., Sanchez, A.M. et al. (2007) The Peak Pairs algorithm for strain mapping from HRTEM images. *Ultramicroscopy* **107**, 1186–1193.

Grillo, V. & Carlino, E. (2008) Novel method for the measurement of STEM specimen thickness by HAADF imaging. *Mircroscopy of Semiconducting Materials 2007, Springer Proceedings in Physics* **120**, 165–168.

Haider, M. (2000) Upper limits for the residual aberrations of a high-resolution aberration-corrected STEM. *Ultramicroscopy* **81**, 163–175.

He, D.S. & Li, Z.Y. (2014) A practical approach to quantify the ADF detector in STEM. *J. Phys.: Conf. Ser.* **522**, 1–4.

Kirkland, E.J. (1984) Improved high resolution image processing of bright field electron micrographs. *Ultramicroscopy* **26**, 151–172.

Kirkland, E.J., Siegel, B.M., Uyeda, N. & Fujiyoshi, Y. (1980) Digital reconstruction of bright field phase contrast images from high resolution electron micrographs. *Ultramicroscopy* **5**, 479–503.

Kuramochi, K., Yamazaki, T., Kotaka, Y., Ohtsuka, M., Hashimoto, I. & Watanabe, K. (2009) Effect of chromatic aberration on atomic-resolved spherical aberration corrected STEM images. *Ultramicroscopy* **110**, 36–42.

Lebeau, J.M., Findlay, S.D., Allen, L.J. & Stemmer, S. (2010) Position averaged convergent beam electron diffraction: theory and applications. *Ultramicroscopy* **110**, 118–125.

LeBeau, J.M. & Stemmer, S. (2008) Experimental quantification of annular dark-field images in scanning transmission electron microscopy. *Ultramicroscopy* **108**, 1653–1658.

Op De Beeck, M., Van Dyck, D. & Coene, W. (1996) Wave function reconstruction in HRTEM: the parabola method. *Ultramicroscopy* **64**, 167–183.

Rosenauer, A., Gries, K., Müller, K., Pretorius, A., Schowalter, M., Avramescu, A., Engl, K. & Lutgen, S. (2009) Measurement of specimen thickness and composition in Al(x)Ga(1-x)N/GaN using high-angle annular dark field images. *Ultramicroscopy* **109**, 1171–1182.

Rosenauer, A. & Schowalter, M. (2008) STEMSIM—A New Software Tool for Simulation of STEM. Microscopy of Semiconducting Materials 2007 **120**, 170–172.

Sawada, H., Sasaki, T., Hosokawa, F. & Suenaga, K. (2014) Resolution enhancement at a large convergence angle by a delta corrector with a CFEG in a low-accelerating-voltage STEM. *Micron* **63**, 35–39.

Schaffer, M., Schaffer, B. & Ramasse, Q. (2012) Sample preparation for atomic-resolution STEM at low voltages by FIB. *Ultramicroscopy* **114**, 62–71.

Voyles, P.M., Grazul, J.L. & Muller, D.A. (2003) Imaging individual atoms inside crystals with ADF-STEM. *Ultramicroscopy* **96**, 251–273.

Yamazaki, T., Kawasaki, M., Watanabe, K., Hashimoto, I. & Shiojiri, M. (2002) Effect of small crystal tilt on atomic-resolution high-angle annular dark field STEM imaging. *Ultramicroscopy* **92**,181–189.

8.5 Talks and Posters

- R. Straubinger, A. Beyer and K. Volz. A setup for environmental *in situ* observation of III-V semiconductors at atomic resolution conditions. *IAM Nano*, 2015, contributed poster.
- R. Straubinger, A. Beyer, L. Duschek, T. Wegele, W. Stolz and K. Volz. *In situ* observation of annealing effects in Ga(N,As,P) multi quantum well structures. *Microscopy & Microanalysis*, 2015, contributed poster.
- R. Straubinger, M. Widemann, A. Beyer, W. Stolz and K. Volz. *In Situ* TEM Investigations of III/V Semiconductor Materials in the Required Environment. *Microscopy Conference*, 2017, contributed poster.
- R. Straubinger, M. Widemann, A. Beyer and K. Volz. Metal organic vapor phase epitaxy inside a TEM under atomic resolution conditions. *Protochips Users Group Meeting*, 2018, contributed talk.

CHAPTER 9

Zusammenfassung und Ausblick

In diesem Kapitel werden die benötigten Modifikationen aufgeführt, um Gruppe V stabilisierte Experimente in einem Transmissionselektronenmikroskop (TEM) durchführen zu können. Weiter werden die mit diesem System gewonnenen Ergebnisse kurz zusammengefasst.

Um die Möglichkeit zu schaffen, in das von Protochips Inc. entwickelte *in situ* System toxische und luftentzündliche Precursor Gase einzuleiten, und damit Gruppe V stabilisierte Experimente durchführen zu können, ist es nötig, einige weitreichende Modifikationen vorzunehmen. Um die sichere Lagerung und den reibungsfreien Transport der Precursor Gase zum *manifold* zu gewährleisten, wurde das bestehende System um einen Gasschrank erweitert. Um jegliche Kontamination der Leitungen durch Sauerstoff zu vermeiden und um sicherzustellen, dass sich die Precursor Gase nicht in der Raumluft ausbreiten, bilden die beiden Systeme eine geschlossene Einheit, in der hoch reiner N_2 als Träger- und Reinigungsgas benutzt wird. Falls nötig, besteht die Möglichkeit, pures Ar oder ein ArH_2 (4 % H_2) Gemisch als Träger- und Reinigungsgas zu benutzen. Der Gasschrank besitzt jeweils drei Anschlussmöglichkeiten für Gruppe III und Gruppe V Precursor Gase. Diese Anschlüsse können, falls nötig, auch für Gasflaschen genutzt werden um weitere Träger- und Reinigungsgase ins System einzuleiten. Soweit wie möglich wurden alle Verbindungen im Gasschrank geschweißt. An Stellen, an denen dies nicht möglich war, wurde die sichere Verbindung mittels *vacuum coupling radiation* (VCR) Metalldichtungen mit Silberbeschichtung hergestellt. Um sicherzustellen, dass keinerlei giftige Gase über die Abgasanlage in die Umwelt entweichen können, wird das Abgas mithilfe eines mini Absorber gereinigt. Um den Brandschutzverordnungen genüge zu tragen, erfüllt der Gasschrank DIN 12925. Das bedeutet, dass er feuerfest ist und sich alle Öffnungen im Falle eines Brandes automatisch schließen. Des Weiteren werden alle Räume, in denen sich Teile des Aufbaus befinden, durch Gassensoren überwacht.

Die atomar aufgelöste *in situ* Untersuchung von single kristallinen Proben, die mittels *metal organic vapor phase epitaxy* (MOVPE) gewachsen wurden, eröffnet viele neue Möglichkeiten. Da momentan gängige *in situ* Halter nur um eine Achse kippbar sind, muss die Präparation und Positionierung der *focussed ion beam* (FIB) Lamelle jedoch so erfolgen, dass die vorab gewählte Zonenachse perfekt parallel zum Strahlengang des Mikroskops ausgerichtet wird. Dies zu bewerkstelligen war ein Teil dieser Arbeit. Dabei wurde der elektronentransparente Teil der FIB Lamella so präpariert, dass er perfekt senkrecht zur ausgewählten Zonenachse ist und zudem von drei Seiten von dickerem Material stabilisiert ist. Diese Stabilisierung verhindert, dass sich der elektronentransparente Teil der FIB Lamella unter Einfluss von Hitze verbiegt. In einer ersten Studie wurde die Funktionalität der Präparationstechnik bestätigt.

Nachdem sich die entwickelte Präparationstechnik als Erfolg erwiesen hat, wurde in zwei weiteren Heizexperimenten die Funktionalität der Precursor Gas Einbringung in die *in situ* Zelle getestet. Hierfür wurde eine Ga(N,As,P) Probe einmal ohne Gruppe V Stabilisierung und einmal mit Gruppe V Stabilisierung thermisch geheizt, und die beiden Serien anschließend miteinander verglichen. Während die Probe, die in einer Gruppe V stabilisierenden Tertiarybutylphosphine (TBP) atmosphere geheizt wurde, bis zu einer Temperatur von ca. 500 °C keinerlei Beschädigung zeigte, begann sich die ohne Stabilisierung geheizte Vergleichsprobe schon bei ca. 300 °C aufzulösen. Im weiteren Verlauf dieser Untersuchung wurde noch über die Dickenänderung der Probe die Abdampfrate von P in Abhängigkeit der Temperatur und des TBP Drucks bestimmt und abschließend die Diffusion von As aus der Ga(N,As,P) Schicht in das umgebende GaP ermittelt. Die dadurch gewonnenen Messdaten ermöglichten es, eine Aktivierungsenergie (E_A) für P in Abhängigkeit der Stabilisierung zu errechnen.

Mit Hilfe von Untersuchungen an Ga(P,Bi) Strukturen mit unterschiedlichen Bi Anteilen sollte die Initialisierungstemperatur, ab welcher das vorhandene Bi anfängt, sich zu akkumulieren, ermittelt werden. Dank der vorausgegangenen Erkenntnisse bezüglich der Gruppe V Stabilisierung konnte der Einfluss von P desorption im untersuchten Temperaturbereich ausgeschlossen werden. Somit war es möglich, den dynamischen Prozess der Bi Akkumulation *in situ* zu beobachten.

Zusätzlich zu den Gruppe V stabilisierten Heizexperimenten wurde im Rahmen dieser Arbeit auch das Wachstum von GaP auf Si untersucht. Für diese Experimente dienten facettierte Si Nanopartikel als Si Substrat. Durch das thermische Ausheizen der Partikel bei 1000 °C in einem $ArSiH_4$ (4 % SiH_4) Gemisch war es möglich, den amorphen SiO_x Mantel um den kristallinen Kern der Partikel zu entfernen. Diese ersten Ergebnisse bestätigen die Vermutung, dass eine Untersuchung von GaP Wachstum auf Si *in situ* unter hoch aufgelösten Bedingungen möglich sein muss. Gleichwohl benötigt es noch weitere Untersuchungen bezüglich der Wachstumsparameter um dies zu bewerkstelligen.

9.1 Ausblick

Der Fokus dieser Arbeit besteht darin, das Fundament für ein neues *in situ* Forschungsfeld an III/V Halbleitermaterialien zu ebnen. Mit der entwickelten Anlage ist es möglich, MOVPE Prozesse zu untersuchen, ohne dabei die Zerstörung der Probe durch Gruppe V Desorption berücksichtigen zu müssen.

Jedoch stellen die hier gezeigten *in situ* Heizexperimente erst den Anfang dar und kratzen nur an der Oberfläche dessen, was mit dieser Technik möglich ist. In zukünftigen Untersuchungen sollte es möglich sein, Diffusionsprozesse auf atomarer Ebene zu untersuchen. Des Weiteren könnte bei zunehmender Verfeinerung der Präparationstechnik die Möglichkeit bestehen, eine Versetzung im Kristall so im elektronentransparenten Teil der Lamelle zu platzieren, dass anschließend *in situ* Untersuchungen der dynamischen Prozesse dieser Versetzung in Abhängigkeit der Temperatur und der Stabilisierung möglich sind.

Ein anderes Themenfeld ist die hoch/atomar aufgelöste Untersuchung von Kristallwachstum *in situ* im TEM. Erste Untersuchungen, die im Abschnitt 6.4 dieser Arbeit aufgeführt sind, haben gezeigt, dass es möglich ist, GaP *in situ* im TEM auf Si aufwachsen zu lassen. Um jedoch kontrolliert Kristallwachstum im Mikroskop demonstrieren zu können, müssen noch viele offenen Fragen, wie z.B. der Precursor Druck, die exakte Temperatur und die Substrat Präparation, innerhalb der Zelle geklärt werden.

Bibliography

[1] E. A. F. Ruska. Beitrag zur übermikroskopischen Abbildung bei höheren Drucken. *Kolloid-Zeitschrift*, 100(2):212–219, 1942.

[2] H. Hashimoto, T. Naiki, T. Eto, and K. Fujiwara. High temperature gas reaction specimen chamber for an electron microscope. *Japanese Journal of Applied Physics*, 7(8):946, 1968.

[3] E. D. Boyes and P. L. Gai. Environmental high resolution electron microscopy and applications to chemical science. *Ultramicroscopy*, 67(1-4):219–232, 1997.

[4] T. W. Hansen and J. B. Wagner. Environmental transmission electron microscopy in an aberration-corrected environment. *Microscopy and Microanalysis*, 18(4):684–690, 2012.

[5] J. F. Creemer, S. Helveg, G. H. Hoveling, S. Ullmann, A. M. Molenbroek, P. M. Sarro, and H. W. Zandbergen. Atomic-scale electron microscopy at ambient pressure. *Ultramicroscopy*, 108(9):993–998, 2008.

[6] T. Yaguchi, M. Suzuki, A. Watabe, Y. Nagakubo, K. Ueda, and T. Kamino. Development of a high temperature–atmospheric pressure environmental cell for high-resolution TEM. *Journal of electron microscopy*, 60(3):217–225, 2011.

[7] N. De Jonge, W. C. Bigelow, and G. M. Veith. Atmospheric pressure scanning transmission electron microscopy. *Nano letters*, 10(3):1028–1031, 2010.

[8] L. Sun, K. W. Noh, J. G. Wen, and S. J. Dillon. In situ transmission electron microscopy observation of silver oxidation in ionized/atomic gas. *Langmuir*, 27(23): 14201–14206, 2011.

[9] J. B. Wagner, F. Cavalca, C. D. Damsgaard, L. D. L. Duchstein, and T. W. Hansen. Exploring the environmental transmission electron microscope. *Micron*, 43(11):1169–1175, 2012.

[10] J. Wu, H. Shan, W. Chen, X. Gu, P. Tao, C. Song, W. Shang, and T. Deng. In situ environmental TEM in imaging gas and liquid phase chemical reactions for materials research. *Advanced Materials*, 28(44):9686–9712, 2016.

[11] R. T. K. Baker and P. S. Harris. Controlled atmosphere electron microscopy. *Journal of Physics E: Scientific Instruments*, 5(8):793, 1972.

[12] R. T. K. Baker, F. S. Feates, and P. S. Harris. Continuous electron microscopic observation of carbonaceous deposits formed on graphite and silica surfaces. *Carbon*, 10(1):93–96, 1972.

[13] R. T. K. Baker. *In situ* electron microscopy studies of catalyst particle behavior. *Catalysis Reviews—Science and Engineering*, 19(2):161–209, 1979.

[14] B. Schaffer, W. Grogger, and G. Kothleitner. Automated spatial drift correction for EFTEM image series. *Ultramicroscopy*, 102(1):27–36, 2004.

[15] K. Kishita, H. Sakai, H. Tanaka, H. Saka, K. Kuroda, M. Sakamoto, A. Watabe, and T. Kamino. Development of an analytical environmental TEM system and its application. *Journal of electron microscopy*, 58(6):331–339, 2009.

[16] F. Hofer, W. Grogger, G. Kothleitner, and P. Warbichler. Quantitative analysis of EFTEM elemental distribution images. *Ultramicroscopy*, 67(1-4):83–103, 1997.

[17] P. L. Gai. Probing selective oxidation catalysis under reaction conditions by atomic scale environmental high resolution electron microscopy. *Current Opinion in Solid State and Materials Science*, 4(1):63–73, 1999.

[18] P. L. Gai. Developments in in situ environmental cell high-resolution electron microscopy and applications to catalysis. *Topics in catalysis*, 21(4):161–173, 2002.

[19] R. Sharma, P. A. Crozier, Z. C. Kang, and L. Eyring. Observation of dynamic nanostructural and nanochemical changes in ceria-based catalysts during in-situ reduction. *Philosophical Magazine*, 84(25-26):2731–2747, 2004.

[20] J. Jinschek and S. Helveg. Image resolution and sensitivity in an environmental transmission electron microscope. *Micron*, 43(11):1156–1168, 2012.

[21] N. Ta, J. Liu, S. Chenna, Peter A. Crozier, Y. Li, A. Chen, and W. Shen. Stabilized gold nanoparticles on ceria nanorods by strong interfacial anchoring. *Journal of the American Chemical Society*, 134(51):20585–20588, 2012.

[22] P. A. Crozier, R. Wang, and R. Sharma. In situ environmental TEM studies of dynamic changes in cerium-based oxides nanoparticles during redox processes. *Ultramicroscopy*, 108(11):1432–1440, 2008.

[23] R. Sharma and K. Weiss. Development of a TEM to study in situ structural and chemical changes at an atomic level during gas-solid interactions at elevated temperatures. *Microscopy Research and Technique*, 42(4):270–280, 1998.

[24] P. L. Gai. Environmental high resolution electron microscopy of gas-catalyst reactions. *Topics in Catalysis*, 8(1-2):97–113, 1999.

[25] R. Sharma. Design and applications of environmental cell transmission electron microscope for in situ observations of gas–solid reactions. *Microscopy and Microanalysis*, 7(6):494–506, 2001.

[26] D. Jacobsson, F. Panciera, J. Tersoff, M. C. Reuter, S. Lehmann, S. Hofmann, K. A. Dick, and F. M. Ross. Interface dynamics and crystal phase switching in GaAs nanowires. *Nature*, 531(7594):317, 2016.

[27] T. W. Hansen, J. B. Wagner, P. L. Hansen, S. Dahl, H. Topsøe, and C. J. H. Jacobsen. Atomic-resolution in situ transmission electron microscopy of a promoter of a heterogeneous catalyst. *Science*, 294(5546):1508–1510, 2001.

[28] P. L. Hansen, J. B. Wagner, S. Helveg, J. R. Rostrup-Nielsen, B. S. Clausen, and H. Topsøe. Atom-resolved imaging of dynamic shape changes in supported copper nanocrystals. *Science*, 295(5562):2053–2055, 2002.

[29] S. Helveg and P. L. Hansen. Atomic-scale studies of metallic nanocluster catalysts by in situ high-resolution transmission electron microscopy. *Catalysis today*, 111(1-2): 68–73, 2006.

[30] T. W. Hansen, J. B. Wagner, and R. E. Dunin-Borkowski. Aberration corrected and monochromated environmental transmission electron microscopy: challenges and prospects for materials science. *Materials Science and Technology*, 26(11):1338–1344, 2010.

[31] J. B. Wagner, J. R. Jinschek, T. W. Hansen, C. B. Boothroyd, and R. E. Dunin-Borkowski. In situ HRTEM—Image corrected and monochromated Titan equipped with environmental cell. In *EMC 2008 14th European Microscopy Congress 1–5 September 2008, Aachen, Germany*, pages 509–510. Springer, 2008.

[32] H. Yoshida, T. Uchiyama, M. de Moor, M. Stekelenburg, and S. Takeda. *In-situ* ETEM analysis of growth mechanism of carbon nanotubes. *Microscopy and Microanalysis*, 13:712–713, 2007.

[33] L. F. Allard, S. H. Overbury, W. C. Bigelow, M. B. Katz, D. P. Nackashi, and J. Damiano. Novel MEMS-Based Gas-Cell/Heating Specimen Holder Provides Advanced Imaging Capabilities for In Situ Reaction Studies. *Microscopy and Microanalysis*, 18 (04):656–666, 2012.

[34] G. Patriarche, F. Glas, M. Tchernycheva, C. Sartel, L. Largeau, J. C. Harmand, and G. E. Cirlin. Wurtzite to zinc blende phase transition in GaAs nanowires induced by epitaxial burying. *Nano letters*, 8(6):1638–1643, 2008.

[35] D. L. Dheeraj, G. Patriarche, H. Zhou, T. B. Hoang, A. F. Moses, S. Grønsberg, A. T. J. van Helvoort, B. Fimland, and H. Weman. Growth and characterization of wurtzite GaAs nanowires with defect-free zinc blende GaAsSb inserts. *Nano letters*, 8 (12):4459–4463, 2008.

[36] S. Kodambaka, J. Tersoff, M. C. Reuter, and F. M. Ross. Germanium nanowire growth below the eutectic temperature. *Science*, 316(5825):729–732, 2007.

[37] J. Wu, W. Gao, J. Wen, D. J. Miller, P. Lu, J. M. Zuo, and H. Yang. Growth of Au on Pt icosahedral nanoparticles revealed by low-dose in situ TEM. *Nano letters*, 15 (4):2711–2715, 2015.

[38] J. Wu and H. Yang. Platinum-based oxygen reduction electrocatalysts. *Accounts of chemical research*, 46(8):1848–1857, 2013.

[39] S. A. Wohlgemuth, R. J. White, M. G. Willinger, M. M. Titirici, and M. Antonietti. A one-pot hydrothermal synthesis of sulfur and nitrogen doped carbon aerogels with enhanced electrocatalytic activity in the oxygen reduction reaction. *Green Chemistry*, 14(5):1515–1523, 2012.

[40] R. Straubinger, A. Beyer, T. Ochs, W. Stolz, and K. Volz. In Situ Thermal Annealing Transmission Electron Microscopy (TEM) Investigation of III/V Semiconductor Heterostructures Using a Setup for Safe Usage of Toxic and Pyrophoric Gases. *Microscopy and Microanalysis*, 23(04):751–757, 2017.

[41] R. Straubinger, A. Beyer, and K. Volz. Preparation and Loading Process of Single Crystalline Samples into a Gas Environmental Cell Holder for *In Situ* Atomic Resolution Scanning Transmission Electron Microscopic Observation. *Microscopy and Microanalysis*, 22(3):515–519, 2016.

[42] S. Liebich, M. Zimprich, A. Beyer, C. Lange, D. J. Franzbach, S. Chatterjee, N. Hossain, S. J. Sweeney, K. Volz, B. Kunert, and W. Stolz. Laser operation of Ga(NAsP) lattice-matched to (001) silicon substrate. *Applied Physics Letters*, 99(7):071109, 2011.

[43] N. W. Rosemann, B. Metzger, B. Kunert, K. Volz, W. Stolz, and S. Chatterjee. Temperature-dependent quantum efficiency of Ga(N,As,P) quantum wells. *Applied Physics Letters*, 103(25):252105, 2013.

[44] B. Kunert, S. Reinhard, J. Koch, M. Lampalzer, K. Volz, and W. Stolz. First demonstration of electrical injection lasing in the novel dilute nitride Ga(NAsP)/GaP-material system. *Physica Status Solidi (c)*, 3(3):614–618, 2006.

[45] B. Kunert, A. Klehr, S. Reinhard, K. Volz, and W. Stolz. Near room temperature electrical injection lasing for dilute nitride Ga(NAsP)/GaP quantum-well structures grown by metal organic vapour phase epitaxy. *Electronics Letters*, 42(10):601–603, 2006.

[46] S. J. Sweeney, A .F. Phillips, A. R. Adams, E. P. O'reilly, and P. J. A. Thijs. The effect of temperature dependent processes on the performance of 1.5-μm compressively strained InGaAs(P) MQW semiconductor diode lasers. *IEEE Photonics Technology Letters*, 10(8):1076–1078, 1998.

[47] A. F. Phillips, S. J. Sweeney, A. R. Adams, and P. J. A. Thijs. The temperature dependence of 1.3- and 1.5-μm compressively strained InGaAs(P) MQW semiconductor lasers. *IEEE Journal of selected topics in Quantum Electronics*, 5(3):401–412, 1999.

[48] S. J. Sweeney, T. Higashi, A. R. Adams, T. Uchida, and T. Fujii. A comparison of algainas and InGaAsP-based 1.3-μm semiconductor lasers using high pressure. *International Journal of High Pressure Research*, 18(1-6):49–55, 2000.

[49] K. Oe and H. Okamoto. New semiconductor alloy $GaAs_{1-x}Bi_x$ grown by metal organic vapor phase epitaxy. *Japanese Journal of Applied Physics*, 37(11A):L1283, 1998.

[50] K. Oe. Characteristics of semiconductor alloy $GaAs_{1-x}Bi_x$. *Japanese Journal of Applied Physics*, 41(5R):2801, 2002.

[51] P. Ludewig, L. Nattermann, W. Stolz, and K. Volz. MOVPE growth mechanisms of dilute bismide III/V alloys. *Semiconductor Science and Technology*, 30(9):094017, 2015.

[52] K. Forghani, A. Anand, L. J. Mawst, and T. F. Kuech. Low temperature growth of $GaAs_{1-y}Bi_y$ epitaxial layers. *Journal of Crystal Growth*, 380:23–27, 2013.

[53] L. Nattermann, A. Beyer, P. Ludewig, T. Hepp, E. Sterzer, and K. Volz. MOVPE growth of Ga(PBi) on GaP and GaP on Si with Bi fractions up to 8%. *Journal of Crystal Growth*, 463:151–155, 2017.

[54] S. Gies, M. Zimprich, T. Wegele, C. Kruska, A. Beyer, W. Stolz, K. Volz, and W. Heimbrodt. Annealing effects on the composition and disorder of Ga(N,As,P) quantum wells on silicon substrates for laser application. *Journal of Crystal Growth*, 402:169–174, 2014.

[55] I. A. Buyanova, G. Pozina, P. N. Hai, N. Q. Thinh, J. P. Bergman, W. M. Chen, H. P. Xin, and C. W. Tu. Mechanism for rapid thermal annealing improvements in undoped GaN_xAs_{1-x}/GaAs structures grown by molecular beam epitaxy. *Applied Physics Letters*, 77(15):2325, 2000.

[56] P. Ludewig. *Growth and characterization of dilute bismide GaAs based alloys for high efficiency infra red laser diodes.* PhD thesis, Philipps-Universität Marburg, 2014.

[57] T. Wegele. *Microstructural Characterization of Dilute N-Containing Semiconductor Alloys and Heterostructures by Scanning Transmission Electron Microscopy.* PhD thesis, Philipps-Universität Marburg, 2016.

[58] L. Nattermann. *MOVPE Growth Studies on Dilute Bismide Containing III/Vs & Development of an MOVPE In-Situ Gas Phase Analysis Setup.* PhD thesis, Philipps-Universität Marburg, 2017.

[59] N. Knaub. *Structural analysis of dilute bismide alloys by means of high resolution scanning transmission electron microscopy.* PhD thesis, Philipps-Universität Marburg, 2016.

[60] G. B. Stringfellow. *Organometallic vapor-phase epitaxy: theory and practice.* Elsevier, 1999.

[61] F. C. Frank and J. H. van der Merwe. One-dimensional dislocations. I. Static theory. *Proceedings of the Royal Society of London. Series A. Mathematical and Physical Sciences*, 198(1053):205–216, 1949.

[62] F. C. Frank and J. H. van der Merwe. One-dimensional dislocations. II. Misfitting monolayers and oriented overgrowth. *Proceedings of the Royal Society of London. Series A. Mathematical and Physical Sciences*, 198(1053):216–225, 1949.

[63] F. C. Frank and J. H. van der Merwe. One-dimensional dislocations-III. Influence of the second harmonic term in the potential representation, on the properties of the model. *Proceedings of the Royal Society of London. Series A. Mathematical and Physical Sciences*, 200(1060):125–134, 1949.

[64] M. Volmer and A. Weber. Zur Keimbildung in übersättigten Gebilden. *Zeitschrift für Physikalische Chemie*, 119(1):277–301, 1926.

[65] I. N. Stranski and L. Krastanow. Zur Theorie der orientierten Ausscheidung von Ionenkristallen aufeinander. *Monatshefte für Chemie und verwandte Teile anderer Wissenschaften*, 71(1):351–364, 1937.

[66] C. Plass, H. Heinecke, O. Kayser, H. Lüth, and P. Balk. A comparative study of $Ga(CH_3)_3$, $Ga(C_2H_5)_3$ and $Ga(C_4H_9)_3$ in the low pressure MOCVD of GaAs. *Journal of Crystal Growth*, 88(4):455–464, 1988.

[67] H. Kräutle, H. Roehle, A. Escobosa, and H. Beneking. Investigations on low temperature mo-cvd growth of GaAs. *Journal of Electronic Materials*, 12(1):215–222, 1983.

[68] G. Zimmermann. Einfluss neuartiger Ausgangsmaterialien in der metallorganischen Gasphasenepitaxie (MOVPE) auf die physikalischen Eigenschaften von III-V-Halbleiterstrukturen. *Cuvillier*, 1994.

[69] A. C. Jones. Metalorganic precursors for vapour phase epitaxy. *Journal of Crystal Growth*, 129(3-4):728–773, 1993.

[70] L. Pauling. *The Nature of the Chemical Bond...*, volume 260. Cornell university press Ithaca, NY, 1960.

[71] M. Mizuta, T. Iwamoto, F. Moriyama, S. Kawata, and H. Kukimoto. AlGaAs growth using trimethyl and triethyl compound sources. *Journal of Crystal Growth*, 68(1): 142–147, 1984.

[72] C. A. Larsen, C. H. Chen, M. Kitamura, G. B. Stringfellow, D. W. Brown, and A. J. Robertson. Organometallic vapor phase epitaxial growth of indium phosphide using new phosphorus sources. *Applied Physics Letters*, 48(22):1531–1533, 1986.

[73] C. H. Chen, C. A. Larsen, G. B. Stringfellow, D. W. Brown, and A. J. Robertson. MOVPE growth of InP using isobutylphosphine and tert-butylphosphine. *Journal of Crystal Growth*, 77(1-3):11–18, 1986.

[74] R. A. Berrigan, J. B. Metson, and D. K. Russell. Radical and Molecular Processes in the Thermal Decomposition of Trimethyl and Triethyl Stibines. *Chemical Vapor Deposition*, 4(1):23–28, 1998.

[75] N. C. Hinshelwood and B. Topley. XLVII.—The Unimolecular Decomposition of Phosphine. *Journal of the Chemical Society*, 125(393-406), 1924.

[76] B. Kuner, D. Trusheim, V. Voßebuvrger, K. Volz, and W. Stolz. Annealing experiments of the GaP based dilute nitride Ga(NAsP). *Physica Status Solidi (a)*, 205(1):114–119, 2008.

[77] M. Wu, E. Luna, J. Puustinen, M. Guina, and A. Trampert. Formation and phase transformation of Bi-containing QD-like clusters in annealed GaAsBi. *Nanotechnology*, 25(20):205605, 2014.

[78] K. Volz, A. Beyer, W. Witte, J. Ohlmann, I. Nmeth, B. Kunert, and W. Stolz. GaP-nucleation on exact Si (001) substrates for III/V device integration. *Journal of Crystal Growth*, 315(1):37–47, 2011.

[79] T. M. Christian, D. A. Beaton, K. Alberi, B. Fluegel, and A. Mascarenhas. Mysterious absence of pair luminescence in gallium phosphide bismide. *Applied Physics Express*, 8(6):061202, 2015.

[80] T. M. Christian, B. Fluegel, D. A. Beaton, K. Alberi, and A. Mascarenhas. Bismuth-induced Raman modes in $GaP_{1-x}Bi_x$. *Japanese Journal of Applied Physics*, 55(10): 108002, 2016.

[81] E. Rutherford. Scattering of Alpha and Beta Particles of Matter and the Structure of the Atom. *Philosophical Magazine*, 21:669, 1911.

[82] S. Pennycook. Z-contrast STEM for materials science. *Ultramicroscopy*, 30(1-2):58–69, 1989.

[83] S. J. Pennycook. Seeing the atoms more clearly: STEM imaging from the Crewe era to today. *Ultramicroscopy*, 123:28–37, 2012.

[84] L. Reimer. *Transmission Electron Microscopy*. Springer, Springer Series in Optical science, 1993.

[85] D. B. Williams and C. B. Carter. *Transmission Electron Microscopy: A Textbook for Materials Science*. Springer, 1996.

[86] M. Watanabe, D. W. Ackland, C. J. Kiely, D. B. Williams, M. Kanno, R. Hynes, and H. Sawada. The aberration corrected JEOL JEM-2200FS FEG-STEM/TEM fitted with an Ω electron energy-filter: Performance characterization and selected applications. *JEOL news*, 41:2–7, 2006.

[87] E. J. Kirkland and M. G. Thomas. A high efficiency annular dark field detector for STEM. *Ultramicroscopy*, 62(1-2):79–88, 1996.

[88] M. Schaffer, B. Schaffer, and Q. Ramasse. Sample preparation for atomic-resolution STEM at low voltages by FIB. *Ultramicroscopy*, 114:62–71, 2012.

[89] D. S. He and Z. Y. Li. A practical approach to quantify the ADF detector in STEM. *Journal of Physics: Conference Series*, 522(1):012017, 2014.

[90] A. Rosenauer and M. Schowalter. STEMSIM—a new software tool for simulation of STEM HAADF Z-contrast imaging. In *Microscopy of Semiconducting Materials*, pages 170–172. Springer, 2008.

[91] P. Ludewig, S. Reinhard, K. Jandieri, T. Wegele, A. Beyer, L. Tapfer, K. Volz, and W. Stolz. MOVPE growth studies of Ga(NAsP)/(BGa)(AsP) multi quantum well heterostructures (MQWH) for the monolithic integration of laser structures on (001) Si-substrates. *Journal of Crystal Growth*, 438:63–69, 2016.

[92] T. Wegele, A. Beyer, S. Gies, M. Zimprich, W. Heimbrodt, W. Stolz, and K. Volz. Correlation of the nanostructure with optoelectronic properties during rapid thermal annealing of Ga(NAsP) quantum wells grown on Si(001) substrates. *Journal of Applied Physics*, 119(2), 2016.

[93] G. Mannino, A. Alberti, R. Ruggeri, S. Libertino, A. R. Pennisi, and G. Faraci. Octahedral faceted Si nanoparticles as optical traps with enormous yield amplification. *Scientific Reports*, 5:1–7, 2015.

[94] A. Stegmüller, P. Rosenow, and R. Tonner. A quantum chemical study on gas phase decomposition pathways of triethylgallane (TEG, $Ga(C_2H_5)_3$) and tert-butylphosphine (TBP, PH2(t-C_4H_9)) under MOVPE conditions. *Physical Chemistry Chemical Physics*, 16(32):17018–17029, 2014.

[95] A. Beyer, R. Straubinger, J. Belz, and K. Volz. Local sample thickness determination via scanning transmission electron microscopy defocus series. *Journal of Microscopy*, 262(2):171–177, 2016.

List of Figures

Danksagung

Eine wissenschaftliche Arbeit ist nie das Werk einer einzelnen Person. Bei all denjenigen, die mir die Erstellung dieser Arbeit ermöglicht haben, möchte ich mich sehr herzlich bedanken. Ganz besonderer Dank gilt dabei ...

... Prof. Dr. Kerstin Volz für die exzellente Betreuung vor und während meiner Dissertation, für die vielen hilfreichen Diskussionen, Tipps und die Möglichkeit an internationalen Konferenzen teilzunehmen.

... Prof. Dr. Wolfgang Stolz, der das Projekt mit wertvollen Ratschlägen und seiner Erfahrung im Bereich MOVPE unterstützt hat.

... Prof. Dr. Heinz Jänsch für die Übernahme des Zweitgutachtens dieser Arbeit.

... Dr. Marc Willinger für die Teilnahme an meiner Prüfungskommission.

... Prof. Dr. Gert Bange für die Übernahme des Postens des Prüfungskommissionsvorsitzendens.

... der Administration unserer Arbeitsgruppe. Dabei sind ganz besonders zu erwähnen Thomas Ochs, Elke Vaupel und Celina Becker, sowie Stefan Reinhardt, Marina Koch und Isabelle Kimmel, die jederzeit mit Rat und Tat zur Seite standen.

... Andreas Beyer und Maximilian Widemann für die tolle Unterstützung, die unzähligen Diskussionen und die vielen gemeinsamen TEM Sessions. Auch möchte ich mich für die nicht ganz so fachlichen Gespräche und die diversen getrunkenen Biere bedanken.

... Manveer Munde für seine wertvollen Korrekturen.

... allen Vereinskollegen des FSV Blitz für die moralische Unterstützung in Form von vielen tollen Flügen.

... der gesamten Arbeitsgruppe für die großartige Unterstützung und die nette Zeit, die ich nicht missen möchte.

... meiner Familie, insbesondere meinen Eltern und meiner Frau Marilena, die mir immer den Rücken frei gehalten haben.